Contents

0.1 Summary

In this thesis, the author has exploited the multiple rf pulse irradiation techniques to restore the magnetic dipole-dipole interaction of the nuclear spins averaged under the magic-angle sample spinning (MAS) conditions. The techniques were applied to ^{13}C and ^{1}H spin systems, and described in chapter 2 and 3, respectively. Several issues linked to the internuclear transfer of the magnetization for signal assignment, and the precise measurement of the internuclear distance for the molecular conformation analysis were addressed with a combination of analytical/numerical calculations and experiments.

In chapter 1, several aspects of the solid-state NMR spectroscopy are introduced, and the basic theories of averaging process of the spin-spin interactions by MAS and its restoration by multiple rf pulse irradiation are summarized. The properties of the double-quantum (DQ) part of the dipolar interaction and its advantages in the experimental application are also presented.

The new pulse sequence developed in chapter 2 has allowed one to variably change the effective bandwidth of the magnetization transfer through the restored DQ-dipolar interactions. This has been enabled by identifying factors that limit the efficiency of the magnetization transfer at off-resonance conditions of the rf pulse irradiation. The factors were identified by investigating the rotation of the nuclear magnetization vectors under the off-resonant rf fields, and analyzed with the average Hamiltonian theory, exact numerical calculations, and experiments. With the new method, the author has demonstrated that the band-selective magnetization transfer experiments could be made with the rf field amplitude smaller than that needed for known methods. The band-selective magnetization transfer has enabled the

versatile truncation of the ^{13}C spin system, reducing the number of spins incorporated in the magnetization transfer event. The effect of the reduced rf power and the simplified spin system has provided the increase of the S/N ratio of the spectrum. The reduced rf power has also made the present method feasible in fast MAS conditions such as $\nu_{\mathrm{R}} = 20$ kHz.

In chapter 3, the DQ-dipolar recoupling technique was applied to precise ^{1}H–^{1}H distance measurement. The principal achievement in chapter 3 is introduction of a novel rf pulse scheme which allows to measure the ^{1}H–^{1}H distances in high precision and spectral resolution. The new method increased the precision of the ^{1}H–^{1}H distance measurement by utilizing the property of the DQ-dipolar interaction that distinguishes the direct magnetization transfer from the diffusive one. The spectral resolution was increased by detecting the ^{1}H magnetization via ^{13}C free-induction signals. The new method was applied to fully ^{13}C-enriched L-valine hydrochloride (Val·HCl). With the least-square simulations, a $^{1}\mathrm{H}^{\alpha}$–$^{1}\mathrm{H}^{\beta}$ distance and ^{13}C–^{1}H bond length were determined as $d_{\alpha\beta} = 248 \pm 4$ pm and $d_{\mathrm{ch}} = 109 \pm 4$ pm, respectively. The strong correlation between $d_{\alpha\beta}$ and d_{ch}, and the multiple ^{1}H–^{1}H couplings in a molecule have been identified as the source of uncertainty in the measured distances.

In chapter 4, main results of this thesis are summarized, and the advantages and disadvantages of the present methods are compared to that of other known methods. The author proposes an expansion of the method developed in chapter 3, and also mentions the perspectives of new SSNMR methodologies to achieve in foreseeable future.

CHAPTER 1

General Introduction

1.1 Solid-State NMR

1.1.1 Wide applications of solid-state NMR

In this decade, a versatile toolbox of basic pulse technologies for the solid-state NMR (SSNMR) has been developed, and the NMR hardware has been improved to enable the high power performance and fast magic angle spinning etc. With all these accomplishments in software and hardware, SSNMR technique has grown into an indispensable tool for chemical analysis, structure determination, and the study of dynamics in organic, inorganic, and biological systems. It is commonly used for a wide range of applications from the characterization of synthetic products to the study of molecular structures of systems such as catalysis, polymers, and proteins, providing number of ways to tackle to problems interested by chemists, physicists, geologists, biologists, and other scientists.

Variety of inorganic materials has been studied for many years with SSNMR in the context of their interesting structure and importance as catalysts. The structures of zeorites [1, 2, 3, 4] and materials adsorbed in zeorites [5, 6, 7, 8] have been actively studied with signals of variety of nuclear species such as ^{29}S, ^{27}Al, ^{113}Cd and ^{207}Pb. Dodecatungstophosphoric acid was recently studied with ^{2}H NMR and ^{1}H–^{31}P spin-echo double resonance techniques, elucidating the origin of its catalytic activity [9]. The adsorption mechanisms of gaseous acid by modified zirconium phosphate accompanied by the intercalation of acid molecules were investigated with ^{13}C and ^{31}P SSNMR [10].

SSNMR has also been applied in the area of solid ionic conductors. The measurement of the spin diffusion and the analysis of the lineshape as well as the relaxation times of the NMR signals provide information on mobility. With its unique ability to provide

the information of dynamics, SSNMR gives great deal of information on the nature of ion movement in these materials [11, 12]. Semiconducting materials have also been studied by frequently focusing the interest on metal-semiconducting transitions, as monitored by nuclei at particular points in the material [13].

Synthetic polymers have been studied with SSNMR since the very early days of the methods. Reactions and structural changes of polymers, and the dynamics of copolymers have been characterized by SSNMR [14, 15]. In some cases, the combination of SSNMR studies with quantum ab initio calculations allowed one to unravel complex dynamics of polymers [16].

SSNMR has a wide variety of applications also to biologically derived materials such as proteins. The molecular structural analysis of peptides and proteins is the major interest of the author. In such systems also, major advantages of SSNMR to provide molecular structural and dynamics information are outstanding. Analyzing structure of proteins is important because the molecular function of many disease-related proteins is tightly correlated to its three-dimensional structure. Further, it provides a starting point to understand the basic biology of living organisms. In this regard, the structural biology that discuss the molecular functions on the basis of precise molecular structure are consistently providing many hottest topics in the research domain.

More recently, with the torrent of the genomic sequencing data, novel research area called structural proteomics has been developed. This aims to determine protein structure and discusses protein functions in more extensive way with the aids of variety of computational techniques of database searching and molecular structure prediction techniques from the amino acid sequence. One of the primary goals of such post-genome projects is to draw

up a catalog of the structure-function relation of the human genome-derived proteins. An international effort involving at least 11 countries is actually on the track, aiming to determine at least one representative protein structure for every estimated 10,000 super families of human protein.

So far, major contributions for the 3D structure determination of proteins are made by the x-ray crystallography and liquid-state NMR spectroscopy. Though the 3D structure can also be sketched out using the cryo-electron microscopy [17], it does not deliver the high resolution of x-ray or NMR methods for analyzing whole protein structures. Recently, an increasing attention is drawn to the applications of SSNMR. Several aspects of SSNMR technique summarized below confers an unique position to SSNMR in these research areas.

(i) SSNMR does not require crystallinity and solubility and has no limitation in molecular weight that is encountered with the liquid-state NMR technique. X-ray crystallography depends on the availability of single crystals in dimension $\gtrsim 100$ μm. The liquid-state NMR technique generally requires high solubility of the sample, and is limited to proteins of molecular weight $\lesssim 40$ kDa for a detailed structural analysis because of the fast relaxation of the NMR signals.

(ii) SSNMR provides determination of proton positions. The detailed structural information about hydrogen atom is only available from the x-ray crystallography experiments with 1.2 Å or better resolution [18]. However, the analysis with such high resolution is generally difficult with proteins in the molecular weight > 10 kDa.

(iii) The molecular structure parameters obtained by SSNMR can be more precise than that determined by liquid-state NMR methods. The SSNMR utilizes spin interactions that remain anisotropic and intense because of the limited molecular motion. The direct dipo-

lar coupling strength between nuclear spins in organic solids is often two orders of magnitude larger than the indirect J coupling mainly utilized in liquid-state NMR.

(iv) SSNMR provides molecular structural information on non-crystalline solids such as biopolymers in amorphous phases in atomic resolution. The peptide and protein fibrils [19] as well as self-aggregated chlorophylls [20] that are insoluble in water or loses their natural super structure in solvents are the important systems of this type.

(v) SSNMR is applicable to membrane proteins. The integral membrane proteins perform essential biological function, and make up 30 % of most eukaryotic genomes [21]. In spite of their importance, very small knowledge of the molecular structure has been provided because the methodologies investigating membrane systems are not yet well developed. Crystallization of the membrane proteins is generally difficult. SSNMR may fill in the vacancy of the method to tackle such molecular systems.

(vi) SSNMR provides information on dynamic structures. The analysis of the ^{2}H and ^{31}P signal line shapes have provided the molecular dynamics information on DNA in the form of the amorphous powder [22] and hydrated fiber [23]. The broad line width in ^{2}H NMR ($\approx$ 200 kHz) permits the investigation of a wide range of molecular motions. In the solid-state samples, in which the overall molecular motion is largely absent, a detailed analysis of the molecular internal motion can be conducted by changing temperature and hydration level of the sample variably.

1.1.2 High resolution solid-state NMR

In many experiments of SSNMR, non-oriented polycrystalline or powder sample is used. The sample molecule is labeled with NMR isotopes at selected or all nuclei, and the sample container is subjected to the magic-angle sample spinning (MAS). The isotope labeling enhances the signal-to-noise (S/N) ratio of the NMR spectrum and labeling uniformly all the carbon and nitrogen atoms in a molecule with ^{13}C and ^{15}N maximize the structural information obtained per sample. The use of the powder sample, in which the molecules take on all possible orientations with random distribution, minimizes labor required in the sample preparation for the NMR measurements. The powder sample gives NMR spectrum with anisotropically broadened lines that are overlapped each other, and the spectrum is difficult or often impossible to analyze. Spinning fast the sample rotor at "magic angle"$\approx 54.736^\circ$ from the external field direction, a technique called MAS, gets rid of the line broadening, making the spectrum amenable to the analysis. The MAS technique has become one of the fundamental tools in high-resolution SSNMR experiments.

Potentially, the molecular structure parameters such as dihedral angle [24, 25, 26] and internuclear distance [27, 28, 29] can be obtained by analyzing the nuclear spin interactions in solids. However, MAS eliminates the anisotropic spin interactions, and also the valuable molecular structural information. The structural information can be selectively re-introduced or re-coupled by manipulating the spin interactions with radio-frequency (rf) pulses irradiated synchronously to the sample rotation. In the following section, theoretical and technical aspects of the spin interactions in solids, ideas of the recoupling and decoupling of the spin interactions in MAS NMR are summarized. Several unique properties of

so-called double-quantum (DQ) part of the magnetic dipole-dipole interaction of spins are also discussed.

1.2 Theoretical Background

1.2.1 Spin interactions in solids

Solid-state NMR spectra are determined by the nuclear spin Zeeman interaction, chemical shift, homonuclear and heteronuclear magnetic dipole-dipole interactions, and interactions with applied rf fields. NMR experiments are analyzed in the rotating frame, where the Hamiltonian terms representing these interactions have the following form [30]:

$$\mathcal{H} = \boldsymbol{\omega}^{\text{eff}}(t) \cdot \mathbf{I} + \Delta\omega^{\text{aniso}}(t) I_z + \omega_{\text{D}}^{II}(t)(3I_{1z}I_{2z} - \mathbf{I}_1 \cdot \mathbf{I}_2) + \omega_{\text{D}}^{IS}(t) I_z S_z, \tag{1.1}$$

where $\boldsymbol{\omega}^{\text{eff}} = (\omega_{\text{RF}}(t), 0, \Delta\omega_z)$. I and S are spin angular momentum vector operators for two different spin species. The isotropic chemical shift and resonance offset, i.e. the difference between the nuclear Lamor frequency and the rf carrier frequency, are included in $\Delta\omega_z$, and the applied rf field is denoted by $\omega_{\text{RF}}(t)$. The time and orientation dependence of the chemical shift anisotropy (CSA) $\Delta\omega^{\text{aniso}}(t)$, and dipolar coupling $\omega_{\text{D}}^{\Lambda}(t)$ are expressed as

$$\Delta\omega^{\text{aniso}}(t) = \sum_{m=-2}^{2} \sum_{n=-2}^{2} A_{2n} D_{n,m}^{(2)}\left(\boldsymbol{\Omega}_{\text{PR}}\right) d_{m,0}^{(2)}\left(\theta_{\text{MAS}}\right) \exp\left(\mathrm{i}m\omega_{\text{R}}t\right), \tag{1.2}$$

$$\omega_{\text{D}}^{\Lambda}(t) = -\sum_{m=-2}^{2} b_{\Lambda}\, D_{0,m}^{(2)}\left(\boldsymbol{\Omega}_{\text{PR}}'\right) d_{m,0}^{(2)}\left(\theta_{\text{MAS}}\right) \exp\left(\mathrm{i}m\omega_{\text{R}}t\right), \tag{1.3}$$

with $\Lambda = II$ or IS, and the dipolar couplings

$$b_{II} = -\frac{\mu_0}{4\pi}\frac{\gamma_I^2}{r_{II}^3}\hbar, \tag{1.4}$$

$$b_{IS} = -\frac{\mu_0}{4\pi}\frac{\gamma_I\gamma_S}{r_{IS}^3}\hbar \tag{1.5}$$

for the homo- and heteronuclear dipolar interactions, respectively. Above, A_{2n} is the spherical tensor element for the chemical shift, γ_j is the magnetogyric ratio of the spin j and r_{ij} is the internuclear distance between spin i and j. The dipolar couplings in Eqs.(1.4) and (1.5), and the principal values of the anisotropic chemical shift A_{2n} in Eq.(1.2) in the respective principal axis system (PAS) can be expressed in the laboratory frame with successive transformations of the coordinate from PAS to a rotor-fixed frame, and from the rotor frame to the laboratory frame. The rotational transformation of the spherical tensors associated with the dipolar coupling and the shielding anisotropy of the nuclear spins can conveniently be expressed with the second-order Wigner rotation matrix elements $D^{(2)}_{m,m'}(\mathbf{\Omega})$, in which $\mathbf{\Omega}$ is a set of Euler angles (α, β, γ) of the rotation. In Eqs.(1.2) and (1.3), the Wigner matrix elements $D^{(2)}_{n,m}(\mathbf{\Omega}_{\rm PR})$ and $D^{(2)}_{0,m}(\mathbf{\Omega}^{'}_{\rm PR})$ describes, respectively, the transformation of the expression of the CSA and the dipolar coupling from PAS to rotor frame. The transformations of these expressions to that in the laboratory frame are described by the reduced Wigner matrix element $d^{(2)}_{m,0}(\beta_{\rm RL})$ with the magic angle $\beta_{\rm RL} = \theta_{\rm MAS}$. The angles incorporated in the two successive coordinate transformations above, $\mathbf{\Omega}_{\rm PR}$ or $\mathbf{\Omega}^{'}_{\rm PR}$ together with $\theta_{\rm MAS}$ defines the direction of the applied magnetic field in the CSA PAS, or the displacement of the internuclear vector from the applied magnetic field direction along the laboratory z axis. The dipolar couplings $\omega^{II}_{\rm D}$ and $\omega^{IS}_{\rm D}$ in Eq.(1.1) obviously contain structural information through the dependence on internuclear distance and directions. Thus, observation of these geometrically dependent NMR frequencies provides us the molecular structural information. The information in dipolar interaction has the advantage over that in CSA because it is independent of electronic structure and therefore independent of quantum chemical calculations or empirical calibration from model compound studies.

1.2.2 Decoupling by MAS and recoupling techniques

With MAS, one can eliminate the secular parts of second-rank spin interactions. The MAS technique is to spin the sample rotor about an axis tilted by the "magic angle", $\theta_{\mathrm{MAS}} = \arccos(1/\sqrt{3}) \approx 54.736^\circ$ (i.e. $3\cos^2\theta_{\mathrm{MAS}} - 1 = 0$), from the applied magnetic field. How the decoupling and recoupling of the spin interactions occur under MAS is overviewed below by taking, an example of the second-rank interaction, the homonuclear dipolar interaction mainly exploited in this thesis.

The dipolar coupling Hamiltonian term $\mathcal{H}_{\mathrm{D}}$ in Eq.(1.1) is time dependent because of the sample rotation with

$$\omega_{\mathrm{D}}^{\Lambda}(t) \propto \sum_{m} C_m \, e^{im\omega_{\mathrm{R}}t}. \tag{1.6}$$

The time-integrated propagator $U(\tau)$ for such time-dependent Hamiltonian $\mathcal{H}(t)$ can be analyzed with an effective propagator U^{eff} written as

$$\begin{aligned} U(\tau) &= \mathcal{T}\exp\left(-i\int_0^\tau \mathcal{H}(t)dt\right) \\ &\approx U^{\mathrm{eff}}(\tau) \\ &= \exp\left\{-i\overline{\mathcal{H}^{\mathrm{eff}}}\tau\right\}, \end{aligned} \tag{1.7}$$

where the effective Hamiltonian $\overline{\mathcal{H}}^{\mathrm{eff}}$ is given by the Magnus expansion,

$$\overline{\mathcal{H}} = \overline{\mathcal{H}}^{(1)} + \overline{\mathcal{H}}^{(2)} + \cdots, \tag{1.8}$$

and

$$\overline{\mathcal{H}}^{(1)} = \tau^{-1}\int_0^\tau dt\mathcal{H}(t), \tag{1.9}$$

$$\overline{\mathcal{H}}^{(2)} = (2i\tau)^{-1}\int_0^\tau dt' \int_0^{t'} dt[\mathcal{H}(t), \mathcal{H}\left(t'\right)]. \tag{1.10}$$

When the rotor frequency ω_{R} is large relative to that of the spin interaction, the effective Hamiltonian only with the lowest order term $\overline{\mathcal{H}}^{(1)}$ becomes a valid approximation [31]. Since

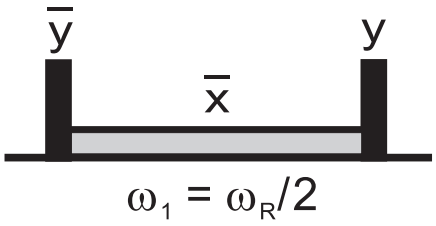

Figure 1.1: Pulse sequence for recovery of homonuclear dipolar couplings in MAS experiments. The solid rectangular represents the $\pi/2$-pulse.

in the dipolar coupling ω_{D} the Fourier component with $m \neq 0$ had time-dependent amplitude oscillations, the simple averaging of $\mathcal{H}_{\mathrm{D}}$ reduces such components to zero. Thus, only the Fourier component with $m = 0$ is left as

$$\begin{aligned} \omega_{\mathrm{D}} &= \tau_{\mathrm{R}}^{-1} \int_0^{\tau_{\mathrm{R}}} \omega_{\mathrm{D}}(t) dt \\ &= -b\, D_{00}^{(2)}(\mathbf{\Omega}_{\mathrm{PR}})\, d_{00}^{(2)}(\theta_{\mathrm{MAS}}). \end{aligned} \tag{1.11}$$

As the reduced Wigner matrix element $d_{00}^{(2)}(\theta) = \frac{1}{2}(3\cos^2\theta - 1)$ is zero at the magic angle, $\theta = \theta_{\mathrm{MAS}}$, thus $\omega_{\mathrm{D}} = 0$ and the dipolar coupling term is zero, $\mathcal{H}_{\mathrm{D}} = 0$. The same average occurs to all second-rank tensoric interactions including CSA and the quadrupolar couplings, that commonly include the factor $d_{00}^{(2)}(\theta_{\mathrm{MAS}})$ in the geometrical part. The NMR signal broadened by the effect of the anisotropic spin interaction in the static case thus becomes a much narrow line under sufficiently fast MAS conditions.

The time dependence of the Hamiltonian term induced by rf pulses can counteract the averaging of the spin interactions induced by MAS. Consequently, the spin interactions can be re-coupled, even under fast MAS conditions. The recoupling techniques allow anisotropic nuclear spin interactions to be turned on and off during desired time periods of the pulse scheme. With such ability, one can obtain the structural information in the anisotropic spin interactions via the high resolution spectra under the effect of MAS.

As a simple illustration of recoupling of homonuclear dipolar interactions, consider

a pulse scheme shown in Fig.1.1, which is the general scheme of the homonuclear rotary resonance (HORROR) sequence [32]. In the pulse scheme, a weak rf field is applied such that the nutation frequency $\omega_1 = -\gamma B_1$ of the rf field matches the condition

$$\omega_{\mathrm{R}} = 2\omega_1, \tag{1.12}$$

with the sample rotation frequency ω_{R}. To simplify the description of the spin dynamics, the rotary resonant irradiation period is considered to be preceded and followed by two strong rf pulses of flip angle $\pi/2$, out of phase with the

rotary resonant field by $\pm\pi/2$. The rotation of the sample has made the geometrical part of the homonuclear dipolar coupling term ω_{D} time dependent. The dipolar term Hamiltonian in Eqs.(1.1) and (1.3) is rewritten as

$$\mathcal{H}_{\mathrm{D}}(t) = \sum_{m=-2}^{2} \omega_{\mathrm{D}}^{(m)} \exp(im\omega_{\mathrm{R}}t)\sqrt{6}\, T_{20}, \tag{1.13}$$

in which the angular terms are collected in $\omega_{\mathrm{D}}^{(m)}$, and the spin part $(3I_{1z}I_{2z} - \mathbf{I}_1 \cdot \mathbf{I}_2)$ is rewritten by the irreducible tensor operator T_{20}. The rf irradiation at the frequency ω_1 introduces an additional time dependence to the dipolar coupling term. It is convenient to express the spin Hamiltonian in the interaction frame of the rf field, in which the Hamiltonian term of the rf field $\mathcal{H}_{\mathrm{RF}} = \omega_1 I_x$ is removed. The dipolar term in the interaction frame denoted by tilde is expressed as

$$\begin{aligned} \tilde{\mathcal{H}}_{\mathrm{D}} &= U_{\mathrm{RF}}^{\dagger}(\tau)\mathcal{H}_{\mathrm{D}}U_{\mathrm{RF}}(\tau) \\ &= \sum_{m\mu} \mathcal{F}_{m\mu} \exp\left\{i(\mu\omega_1 + m\omega_{\mathrm{R}})t\right\} T_{2\mu}, \end{aligned} \tag{1.14}$$

where $U_{\mathrm{RF}} = \exp\left\{-i\omega_1 I_x\right\}$, and both spatial- and spin-rotation indices m and μ run from -2 to 2. The rotational components are given by

$$\mathcal{F}_{m\mu} = \omega_{\mathrm{D}}^{(m)}\, d_{\mu 0}^{(2)}(-\pi/2). \tag{1.15}$$

The reduced rotation function $d^{(2)}_{\mu 0}(-\pi/2)$ takes into account the "bracketing" of the rotary resonance period by the strong $\pi/2$ pulses.

Providing the frequencies ω_1 and $\omega_{\rm R}$ are larger than the other interactions, the effective spin Hamiltonian is approximated with the lowest-order term of the Magnus expansion, i.e. a simple average of $\tilde{\mathcal{H}}_{\rm D}$ over the rotational period. Since the frequencies ω_1 and $\omega_{\rm R}$ satisfy the condition of Eq.(1.12), the exponential factors in Eq.(1.14) is averaged to zero unless the spin rotation index μ and space rotation index m are related by $\mu = -2m$. Since the space component with $m = 0$ vanishes with MAS, the only remaining terms for the dipolar interaction has $(m, \mu) = (1, -2)$ or $(-1, 2)$. The effective spin Hamiltonian denoted by the over-bar is given by

$$\begin{aligned}\overline{\mathcal{H}}_{\rm D} &= \frac{3}{2}\left\{\omega_{\rm D}^{(1)} T_{2-2} + \omega_{\rm D}^{(-1)} T_{22}\right\} \\ &= \frac{3}{8\sqrt{2}} b \sin(2\beta_{\rm PR}) \left(I^+ I^+ e^{i\gamma_{\rm PR}} + I^- I^- e^{-i\gamma_{\rm PR}}\right). \end{aligned} \tag{1.16}$$

It is seen that the effective Hamiltonian recoupled in Eq.(1.16) involves terms with the double-quantum (DQ) transition operators I^+I^+ and I^-I^-. Under such Hamiltonian, the spin state can be evolved into the double-quantum coherence (DQC), in which both two dipolar coupled spins change their spin states simultaneously. Thus, the dipolar component recoupled in Eq.(1.16) is termed as the double-quantum (DQ) part of the homonuclear dipolar interaction. The unique properties of the DQ-dipolar component can lead to useful features in applications such as multidimensional spectroscopy and multiple quantum spectroscopy based on the DQC. Several important methods that determine the local geometry of molecules, such as torsion angle [33, 34], and the relative orientation of CSA tensors [35], depend on excitation of the DQC.

1.3 Technical Background

1.3.1 Double-quantum dipolar interactions

Applying the DQ-dipolar interaction in experiments is useful from several viewpoints. The DQ-dipolar interaction excites the DQC of a ^{13}C-spin pair. The DQC is a correlation between the polarization of neighboring ^{13}C spins. By first exciting the DQC and reconverting only the DQC into observable signal, eliminating other coherences with phase cycling, one can distinguish NMR signals of the site-specifically introduced ^{13}C labels from that of randomly distributed natural ^{13}C spins. The ability of such double-quantum "filter" is particularly important in analyzing large molecule that involves a few ^{13}C-labeled sites [36].

The excitation of the DQC also enables to conduct multi-dimensional DQ/SQ correlation experiments [37, 38], in which the time evolution of the DQC is correlated with the evolution of the single-quantum coherence (SQC) observable. Because during the DQ time dimension the generated DQCs evolve under the sum of the chemical shifts of the two respective nuclei, the DQ/SQ spectrum possesses different frequency labels for a correlation signal in the two axis of the 2D spectrum. This provides an opportunity to resolve the correlation signal which can not be resolved in normal SQ/SQ 2D correlation spectrum.

One of interesting features of the DQ-dipolar terms recoupled in Eq.(1.16) is that the spatial- and spin-rotation indices m and μ have a one-to-one correspondence, i.e. only terms with $(m, \mu) = (1, -2)$ and $(-1, 2)$ are allowed in the effective Hamiltonian. In this favorable case, the amplitude of the coupling depends on the crystallite orientation only through the Euler angle β_{PR}. The angle γ_{PR} just changes the relative phase of two DQ-dipolar terms in Eq.(1.16). In a contrasting case where terms e.g. with $(m, \mu) = (\pm 1, -2)$ are allowed, the

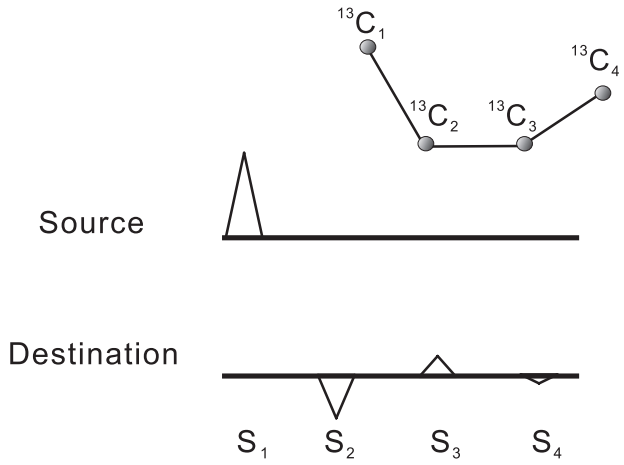

Figure 1.2: Pictorial NMR spectrum explaining the alternating cross peak intensities for the transferred magnetization under the DQ-dipolar interaction. In the assumed ^{13}C-spin system, C_1 spin is assumed to be excited. During the DQ-mixing period, a negative cross peak appears for C_2, indicating the C_1 magnetization transferred *directly* to C_2 is dominant. The magnetization transferred to C_3 spin by intermediating C_2 in turn displays a positive peak.

amplitude depends both on $\beta_{\rm PR}$ and $\gamma_{\rm PR}$ as

$$\begin{aligned}\omega^{'}_{\rm DQ} &= \omega^{(1)}_{\rm DQ} + \omega^{(-1)}_{\rm DQ} \\ &\propto \sin(2\beta_{\rm PR})\left(e^{-i\gamma_{\rm PR}} - e^{i\gamma_{\rm PR}}\right) \\ &= \sin(2\beta_{\rm PR})\cos(\gamma_{\rm PR}).\end{aligned} \tag{1.17}$$

The independence of the coupling amplitude on one of two Euler angles leads to large overall recoupling for powder samples. This feature so called γ-encoding is realized so far only with the DQ-dipolar part of the dipolar interaction.

Another interesting property of the DQ-dipolar term is that the nuclear magnetization transferred under the effect of the DQ-dipolar interactions displays magnetization transfer signals with alternating intensities depending on the number of intermediating spins in the transfer pathway. When odd and even number of spins intermediate the transfer process between the source and destination spins, negative and positive cross peaks appear, respectively. Thus, in the ^{13}C spin system for instance, signals of a carbon across one chemical

bond and that across two chemical bonds can easily be distinguished on the spectrum (see Fig.1.2). This feature aids the signal assignment of the spectrum [39].

1.3.2 Development of recoupling technique

The simplest version of the

DQ-dipolar recoupling pulse sequence HORROR shown in Fig.1.1 functions well only in a small frequency range of about $0.4\,\nu_{\mathrm{R}}$, where ν_{R} is the MAS frequency. Thus under typical experimental settings with $\nu_{\mathrm{R}} \approx 10$ kHz and the external applied field strength of $B_0 \approx 11$ T, the effective frequency range of the recoupling is only about 4 kHz. Considering the large chemical shift dispersion of the ^{13}C spins of about 20 kHz at $B_0 \approx 11$ T, the applicability of HORROR to ^{13}C DQ-dipolar recoupling is limited. In addition, the recoupling by HORROR, established with the CW rf irradiation, is highly dependent on the spatial homogeneity of the rf filed amplitude. Because normal NMR probe usually has ~ 5 % distribution of the rf amplitude across the coil, the intolerance of HORROR to the rf inhomogeneity severely limits its experimental applicability. Another issue to which one should pay attention is the residual spin interactions other than desired homonuclear DQ-dipolar interaction. The co-existence of other spin interactions may introduce unnecessary complication or undesirable signal loss in the final spectrum. The elimination of residual ^{13}C/^{1}H heteronuclear dipolar couplings and intense CSA of ^{13}C spins are particularly important. Of course, the γ-encoding property of HORROR favorable for the powder samples should be retained. The recoupling pulse sequences dealing with these issues have been developed for last several years.

A recently developed DQ-dipolar recoupling sequence, POST-C7 [40], has real-

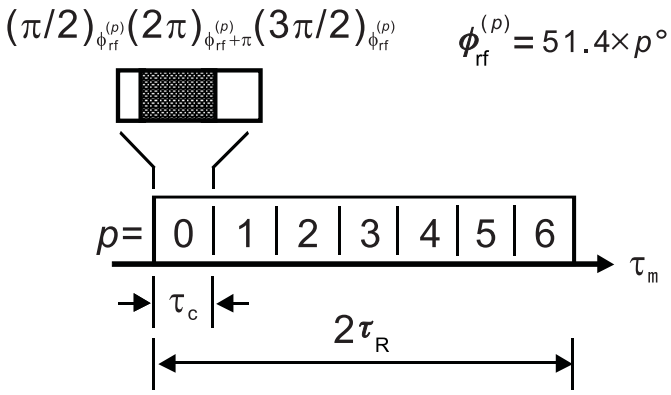

Figure 1.3: Pulse sequence for permutationaly offset-compensated C7 sequence under MAS.

ized the low CSA dependence, the γ-encoding property, and suppression of the offset and rf inhomogeneity effects. As shown in Fig.1.3, POST-C7 involves seven "element pulses" contiguously irradiated to span two rotor revolutions, accompanying a systematic rf phase shifts in contrast to the CW irradiation scheme used in HORROR. The element pulse is an rf cycle for a period $\tau_{\rm c}$, thus the state of the irradiated spins are invariant before and after the element pulse in the absence of other interactions. The overall phase $\phi_{\rm rf}^{(p)}$ of the p-th element pulse is set as $\phi_{\rm rf}^{(p)} = \frac{2\pi}{7}p$ to be rotated once in the xy plane during the two rotor revolutions. This rotor-synchronous phase rotation scheme is often termed as "z-rotation". The "POST" element pulse that is first introduced with POST-C7 has a particular form, $(\pi/2)_{\phi_{\rm rf}^{(p)}}(2\pi)_{\phi_{\rm rf}^{(p)}+\pi}(3\pi/2)_{\phi_{\rm rf}^{(p)}}$, which has made the spin part of the "error" Hamiltonian terms, that describe the non-ideality of the pulse sequence, perpendicular to the z axis of the rf phase rotation. The averaging over the z rotation, POST-C7 sequence eliminated the error Hamiltonian terms of the offset and rf inhomogeneity. This has lead to the stable recoupling of the DQ-dipolar interaction over larger offset range than that by the predecessor, C7 sequence [41].

Major drawback of POST-C7 is that it needs the rf field amplitude 7 times the rotor

frequency. It has been shown that the rf power of the I-spin decoupling for most of these sequence needs 3 times the power input for the S-spin mixing [42, 43]. However, most commercial probes can accommodate only restricted power, which often severely limits the use of several of this kind of recoupling sequence at high MAS rate. For POST-C7, the I-spin decoupling power should be approximately 21 times the MAS rate. This means that intolerably large field amplitude, > 210 kHz,

is needed under moderate sample spinning rate of 10 kHz. Thus, in many cases one is obliged to compromise with the ^{1}H-decoupling filed amplitude insufficient to completely remove the CH dipolar couplings. The residual CH coupling leads the ^{13}C magnetization to relax during the mixing period, and decreases the S/N ratio of the spectrum.

A new DQ-dipolar recoupling sequence SPC5 introduced in 1999 [44] reduced the required mixing field amplitude to 5/7 of that needed for POST-C7 by using only five element pulses during two rotor revolutions. In 2000, the common recoupling principle for C7 and SPC5 sequences has been developed to a general symmetry principle of the rotor-synchronous rf irradiation. Under the light of the general symmetry principle, the rf irradiation is largely classified into two major symmetries denoted as $\mathrm{C}N_n^\nu$ [45] for which the magnetization vector is flipped during each element pulse by 2π, and $\mathrm{R}N_n^\nu$ [46] for which the flip angle of the element pulse is π. The $\mathrm{C}N_n^\nu$ sequence involves N element pulses during n rotor revolutions. The phases of neighboring element pulses differ by $2\pi\nu/N$. The phases of the sample rotor at the end of two neighboring element pulses differ by $2\pi n/N$.

The $\mathrm{C}N_n^\nu$ sequence recouples particular spin interaction terms with a similar concept as HORROR explained with Eqs.(1.12)$\sim$(1.16) except that the presence of an additional rf modulation introduced by the z rotational phase shift. Remembering that the rf phase and

rotor phase at the mixing time $\tau_{\mathrm{m}} = p\tau_{\mathrm{c}}$ were $\phi_{\mathrm{rf}}^{(p)} = \frac{2\pi\nu}{N}p$ and $\phi_{\mathrm{rotor}}^{(p)} = \frac{2\pi n}{N}p$, respectively, The spin interaction Hamiltonian in the interaction frame of rf field is expressed for p-th element pulse as

$$\tilde{\mathcal{H}}_p = \tilde{\mathcal{H}}_0 \exp\left\{ i\frac{2\pi}{N}(mn - \mu\nu)p \right\}. \tag{1.18}$$

On the z-rotational averaging written as

$$\overline{\mathcal{H}}^{(1)} = \frac{1}{N\tau_{\mathrm{c}}} \sum_{p=0}^{N} \tilde{\mathcal{H}}_p \tau_{\mathrm{c}}, \tag{1.19}$$

the spin interaction terms that do not satisfy the recoupling condition $mn - \mu\nu = 0$ are eliminated for the first-order average Hamiltonian, $\overline{\mathcal{H}}^{(1)}$. Here, it is evident that the symmetry numbers $\nu = 1$ and $n = 2$ associated with the C7 sequence satisfy the recoupling condition for the DQ-dipolar interaction with spatial and spin rotation indices $m = \pm 1$ and $\mu = \pm 2$ as $mn - \mu\nu = \pm 1 \cdot 2 - (\pm 2 \cdot 1) = 0$.

1.4 Scope of this Thesis

The structure analysis of proteins by SSNMR often involves the following steps. In the first step, isotope-labeled protein samples high in purity and labeling rate must be prepared. In the second step, the resonances in multidimensional SSNMR spectra must be resolved and assigned. The assignment of the resonance signals to corresponding spins in a molecule enables to get structural and dynamical information of the molecule site-specifically. For example, it is well known that the chemical shift values of C^{α} spins on the backbone, and C^{β} on side chain of an amino acid residue in a protein can be related to the local secondary structure of the protein. Also, analyzing the line shape change and/or the change in the chemical shift value associated with the pH, temperature as well as pres-

sure change provides molecular dynamical information. The assignment is accomplished by a number of multidimensional correlation techniques that encode the chemical shifts of various spins during different time periods. Between these two encoding periods, the magnetization is mixed among spins by often using the dipolar couplings of spins. In the third step, the molecular structure parameters such as dihedral angles and internuclear distances are to be accumulated. In many cases, one can generate a set of most probable molecular structures by the molecular geometrical calculations based on the accumulated structural constraints. As mentioned in section 1.2.1, the internuclear distance is a preferred structural parameter over CSA because of its independence from the electronic structures of atoms.

In this thesis, studies are focused on two current problems associated to above mentioned second and third steps of the structure analysis by SSNMR, namely the signal assignment and internuclear distance measurement.

In many cases, the signal assignment is conducted for ^{13}C resonances because of the generally good spectral resolution. For the magnetization transfer among ^{13}C spins, it is useful to exploit the DQ-dipolar interaction for reasons stated in section 1.3.1. Several effective recoupling sequences for the DQ-dipolar recoupling is provided by the symmetry-based CN sequences introduced in section 1.3.2. The trouble in the ^{13}C-recoupling experiments occurs when the mixing rf field amplitude ω_{mix} on ^{13}C spins approaches to the amplitude ω_{dec} of ^{1}H-decoupling field. In this case, the CH dipolar interaction is partially recoupled by the Hartmann-Hahn condition ($\omega_{\mathrm{mix}} = \omega_{\mathrm{dec}}$), and it significantly reduces the ^{13}C magnetization, thus the S/N ratio of the spectrum. Because the upper bound for ω_{dec} is limited by a probe, a small ω_{mix} is desirable. The CN sequence requires ω_{mix} determined as a function of the spinning frequency ω_{R}, the symmetry numbers N, n and ν as well as the total flip angle

of the element pulse ϕ_{tot} as

$$\frac{\omega_{\mathrm{mix}}}{\omega_{\mathrm{R}}} = \frac{(\phi_{\mathrm{tot}}/2\pi)\,N}{n}. \tag{1.20}$$

Study in chapter 2 aims the reduction of ω_{mix} by reducing ϕ_{tot} to alleviate the ω_{dec}–ω_{mix} matching problem, and to accommodate the CN recoupling sequence under fast MAS rate in the range $\omega_{\mathrm{R}}/2\pi = 10 \sim 20$ kHz. The author analytically derives a careful design of the element pulse that decreases ϕ_{tot} but does not decrease the efficiency of the recoupling.

The evolution of a nuclear spin system under the effect of the dipolar interactions can be analyzed to estimate internuclear distances. In many cases, the time dependence of the magnetization transfer between spins is analyzed. For the collection of a large number of suitable distance constraints from small number of samples, the ^{13}C–^{13}C constraints have been the primal importance because of the good signal resolution. However, the measurement of long ^{13}C–^{13}C distances that are dependent on the molecular conformation is hindered in uniformly ^{13}C-enriched samples by the covalently-bonded ^{13}C spins. This is because the chemically-bonded partner is generally closest in space, and because the evolution of the spin system among many dipolar couplings is dominated by a strongest one of them due to a phenomenon referred to as dipolar truncation [47]. The ^{1}H–^{1}H distance information is preferred over that of ^{13}C–^{13}C because the shortest ^{1}H–^{1}H distance can often be conformation-dependent in organic molecules. Moreover, the feasibility of the distance measurement by NMR experiment critically depends on the size of effective dipolar coupling between nuclei under study. Thus, the experiments involving low-γ ^{13}C–^{13}C pair are plagued by relatively small effective dipolar couplings compared with ^{1}H–^{1}H spin systems. In this course, advantage of the ^{1}H–^{1}H distance information is clear. Actually, success of liquid-state NMR in determining 3D molecular structures can mainly be ascribed to the abundant short

^{1}H–^{1}H distances that can be obtained in high sensitivity and resolution with NOESY-related correlation experiments.

Method to estimate the ^{1}H–^{1}H proximity in solids has been previously suggested by several authors. The troubles therein have been the low precision and the small amount of distance information that can be obtained per experiment. Classically, the ^{1}H spin diffusion through the ^{1}H–^{1}H dipolar couplings has been analyzed by solving the diffusion equation to roughly estimate a very large structural feature in dimension up to 2000 Å [48, 49]. The amount of the ^{1}H–^{1}H constraints that can be drawn per experiment is limited by the low-resolution of the ^{1}H spectroscopy in solids [50]. The spectral resolution was improved recently by the introduction of a three-dimensional ^{1}H–^{1}H–^{13}C correlation experiment [51] and ^{1}H-^{1}H DQ/SQ spectroscopy [37]. Although the precision of distance was improved by a method that evaluates the DQ MAS sideband patterns [27], only two ^{1}H–^{1}H distances were distinguished by their ^{1}H chemical shift difference. In chapter 3, the author develops a method to increase the precision and amount of ^{1}H–^{1}H distance obtained by experiment. The ^{1}H magnetization is mixed under the effect of the ^{1}H DQ-dipolar interaction recoupled with POST-C7 and detected via ^{13}C free-induction signals. With the DQ-mixing process, the magnetization exchanged between two spatially closest ^{1}H spin is characterized with two NMR signals 180° out of phase each other. Thus, they appear as positive and negative intensity signals in the spectrum. This property increases the precision of the ^{1}H–^{1}H distance measurement. Detecting ^{1}H spin dynamics via high-resolution ^{13}C spectrum improves the amount of ^{1}H–^{1}H distance that can be determined per experiment. The author discusses the major differences that occur between ^{13}C recoupling and ^{1}H recoupling experiment with POST-C7, focusing his attention on the residual spin interactions during POST-C7 irradiation

and on the effective offset bandwidth of the magnetization transfer achieved with POST-C7.

REFERENCES

[1] T.-H. Chen, B. H. Wouter, and P. J. Grobet, Structure change of molecular sieve SAPO-37 at high temperature studied by ^{27}Al multiple quantum and multi-nuclear MAS NMR, *Stud. Surf. Sci. Catal.* **135**, 2217–2223 (2001).

[2] C. A. Fyfe, J. L. Bretherton, and L. Y. Lam, Detection of the "invisible aluminum" and characterization of the multiple aluminum environments in zeorite USY by high-field solid-state NMR, *Chem. Commum.* **17**, 1575–1576 (2000).

[3] S. B. Hong, D.-Y. Han, O. H. Han, and I.-S. Nam, Solid-state NMR evidence for the presence of two crystallographically distinct tetrahedral sites in zeorite merlinoite, *Chem. Commum.* **17**, 1719–1720 (2000).

[4] A. Eldewik, J. M. Hook, N. K. Singh, and R. F. Howe, Multinuclear solid-state NMR study of cadmium- and lead-exchanged LTA zeorite, *Magn. Reson. Chem.* **37**, S63–S68 (1999).

[5] M. Sanchez-Sanchez, T. Blasco, and F. Rey, An NMR study on the adsorption and reactivity of chloroform over alkali exchanged zeolites X and Y, *Phys. Chem. Chem. Phys.* **1**, 4529–4535 (1999).

[6] E. Bosch, S. Huber, J. Weitkamp, and H. Knozinger, Adsorption of trichloro- and trifluoromethane in Y-zeolites as studied by IR spectroscopy and multinuclear solid-state

NMR, *Phys. Chem. Chem. Phys.* **1**, 579–584 (1999).

[7] G. W. Wagner and P. W. Bartram,

Reactions of VX, HD, and their simulants with NaY and AgY zeolites. Desulfurization of VX on AgY, *Langmuir* **15**, 8113–8118 (1999).

[8] J. Wu and S. C. Larsen, Solid-state nuclear magnetic resonance study of acetone oxime adsorbed on CuZSM-5 and on HZSM-5, *J. Catal.* **182**, 244–256 (1999).

[9] T. Ueda, T. Tatsumi, T. Eguchi, and N. Nakamura, Structure and properties of acidic protons in anhydrous dodecatungstophosphoric acid, $H_3PW_{12}O_{40}$, as studied by solid-state ^1H, ^2H NMR, and ^1H–^{31}P sedor NMR, *J. Phys. Chem. B* **105**, 5391–5396 (2001).

[10] H. Nakayama, A. Hayashi, T. Eguchi, N. Nakamura, and M. Tsuhako, Unusual adsorption mechanism for carboxylic acid gases by polyamine-intercalated α-zirconium phosphate, *J. Mater. Chem.* **12**, 3093–3099 (2002).

[11] H. A. Every, A. G. Bishop, D. R. MacFarlane, G. Oraedd, and M. Forsyth, Room temperature fast-ion conduction in imidazolium halide salts, *J. Mater. Chem.* **11**, 3031–3036 (2001).

[12] Y. Tsukahara, K. Hashimoto, K. Kaeriyama, A. Niwa, M. A. Mehta, T. Fujitani, and K. Hayamizu, Ionic conductivity and NMR self-diffusion in poly(macromonomer)s of vinylbenzyl poly(ethylene oxide)s, *Chem. Lett.* **6**, 490–491 (2001).

[13] H. Lock, J. Xiong, Y.-C. Wen, B. A. Parkinson, and G. E. Maciel, Solid-state Si-29, Cd-113, Sn-119, and P-31 NMR studies of II-IV-P-2 semiconductors, *Solid State Nucl. Magn. Reson.* **20**, 118–129(2001).

[14] S. C. Martin, J. J. Liggat, and C. E. Snape, In situ NMR investigation into the thermal degradation and stabilisation of PAN, *Polym, Degrad. Stab.* **74**, 407–412 (2001).

[15] P. A. Mirau, S. A. Heffner, and M. Schilling, Fast magic-angle spinning proton NMR studies of polymers at surfaces and interfaces, *Solid State Nucl. Magn. Reson.* **16**, 47–53 (2000).

[16] J. Brus and J. Dybal, Solid-state NMR study of structure, size and dynamics of domains in hybrid siloxane networks, *Polymer* **41**, 5269–5282 (2000).

[17] D. Acehan, X. Jiang, D. G. Morgan, J. E. Heuser, X. Wang, and C. W. Akey, Three-dimensional structure of apoptosome: implications for assembly, procaspase-9 binding, and activation, *Mol. Cell.* **9**, 423–432 (2002).

[18] M. E. Hatcher, I. LeTrong, R. Stenkamp, and G. P. Drobny, Local dynamics of the CpG step in a DNA crystal, *J. Am. Chem. Soc.* **123**, 8874–8875 (2001).

[19] T. S. Burkoth, T. L. S. Benzinger, V. Urban, D. M. Morgan, D. M. Gregory, P. Thiyagarajan, R. E. Botto, S. C. Meredith, and D. G. Lynn, Structure of the β-amyloid$_{(10-35)}$ fibril, *J. Am. Chem. Soc.* **122**, 7883–7889 (2000).

[20] I. de Boer, L. Bosman, J. Raap, H. Oschkinat, and H. J. M. de Groot, 2D ^{13}C–^{13}C MAS NMR correlation spectroscopy with mixing by true ^{1}H spin diffusion reveals long-range intermolecular distance restraints in ultra high magnetic field, *J. Magn. Reson.* **157**, 286–291 (2002).

[21] E. Wallin, and G. von Heijne, Genome-wide analysis of integral membrane proteins from eubacterial archaean and eukaryotic organisms, *Protein Sci.* **7**, 1029–1038 (1998).

[22] M. E. Hatcher, D. L. Mattiello, G. A. Meints, J. Orban, G. P. Drobny, A solid-state deuterium NMR study of the localized dynamics at the C9pG10 step in the DNA dodecamer [d(CGCGAATTCGCG)]$_2$, *J. Am. Chem. Soc.* **120**, 9850–9862 (1998).

[23] T. Fujiwara, and H. Shindo, Phosphorus-31 nuclear magnetic resonance of highly ori-

ented DNA fibers. 2. Molecular motions in hydrated DNA, *Biochemistry* **24**, 896–902 (1985).

[24] X. Feng, P. J. E. Verdegem, M. Edén, D. Sandström, Y. K. Lee, P. H. M. Bovee-Geurts, W. J. de Grip, J. Lugtenburg, H. J. M de Groot, and M. H. Levitt, Determination of a molecular torsional angle in the metarhodopsin-I photointermediate of rhodopsin by double-quantum solid-state NMR, *J. Biomol. NMR* **16**, 1–8 (2000).

[25] B. Reif, M. Hohwy, C. P. Jaroniec, C. M. Rienstra, and R. G. Griffin, NH-NH vector correlation in peptides by solid-state NMR, *J. Magn. Reson.* **145**, 132–141 (2000).

[26] K. Nomura, K. Takegoshi, T. Terao, K. Uchida, and M. Kainosho, Three-dimensional structure determination of a uniformly labeled molecule by frequency-selective dipolar recoupling under magic-angle spinning, *J. Biomol. NMR* **17**, 111–123 (2000).

[27] J. Gottwald, D. E. Demco, R. Graf, H. W. Spiess, High-resolution double-quantum NMR spectroscopy of homonuclear spin pairs and proton connectivities in solids, *Chem. Phys. Lett.* **243**, 314–323 (1995).

[28] S. R. Kiihne, K. B. Geahigan, N. A. Oyler, H. Zebroski, M. A. Mehta, and G. P. Drobny, Distance measurements in multiply labeled crystalline cytidines by dipolar recoupling solid state NMR, *J. Phys. Chem. A* **103**, 3890–3903 (1999).

[29] J. M. Griffith, A. E. Bennet, M. Engelhard, F. Siebert, J. Raap, J. Lugtenburg, J. Herzfeld, R. G. Griffin, Structural investigation of the active site in Bacteriorhodopsin: Geometric constraints on the roles of Asp-85 and Asp-212 in the proton-pumping mechanism from solid state NMR, *Biochemistry* **39**, 362–371 (2000).

[30] M. Mehring, *Principles of High Resolution NMR in Solids* (Springer-Verlag, New York, 1983).

[31] U. Haeberlen, *High Resolution NMR in Solids, Selective Averaging* (Academic Press, New York, 1976).

[32] N. C. Nielsen, H. Bildsøe, H. J. Jakobsen, and M. H. Levitt, Double-quantum homonuclear rotary resonance: Efficient dipolar recovery in magic-angle spinning nuclear magnetic resonance, *J. Chem. Phys.* **101**, 1805–1812 (1994).

[33] M. Hong, J. D. Gross, and R. G. Griffin, Site-resolved determination of peptide torsion angle ψ from the relative orientation of backbone N–H and C–H bonds by solid-state NMR, *J. Phys. Chem. B* **101**, 5869–5874 (1997).

[34] P. R. Costa, J. D. Gross, M. Hong, and R. G. Griffin, Solid-state NMR measurement of Ψ in peptides: a NCCN 2Q-heteronuclear local field experiment, *Chem. Phys. Lett.* **280**, 95–103 (1997).

[35] D. M. Gregory, M. A. Mehta, J. C. Shiels, and G. P. Drobny, Determination of local structure in solid nucleic acids using double quantum nuclear magnetic resonance spectroscopy, *J. Chem. Phys.* **107**, 28–42 (1997).

[36] A. S. D. Heindrichs, H. Geen, and J. J. Titman, MAS double-quantum filtered dipolar shift correlation spectroscopy, *J. Magn. Reson.* **147**, 68–77 (2000).

[37] I. Schnell, S. P. Brown, H. Y. Low, H. Ishida, and H. W. Spiess, An investigation of hydrogen bonding in benzoxazine dimers by fast magic-angle spinning and double-quantum ^{1}H NMR spectroscopy, *J. Am. Chem. Soc.* **120**, 11784–11795 (1998).

[38] I. Schnell, B. Langer, S. H. M. Söntjens, M. H. P. van Genderen, R. P. Sijbesma, and H. W. Spiess, Inverse detection and heteronuclear editing in ^{1}H–^{15}N correlation and ^{1}H–^{1}H double-quantum NMR spectroscopy in the solid state under fast MAS, *J. Magn. Reson.* **150**, 57–70 (2001)

[39] R. G. Griffin, Dipolar recoupling in MAS spectra of biological solids, *Nature Struc. Biol.* NMR supplement, 508–512 (1998). .

[40] M. Hohwy, H. J. Jakobsen, M. Edén, M. H. Levitt, and N. C. Nielsen, Broadband dipolar recoupling in the nuclear magnetic resonance of rotating solids: A compensated C7 pulse sequence, *J. Chem. Phys.* **108**, 2686–2694 (1998).

[41] Y. K. Lee, N. D. Kurur, M. Helmle, O. G. Johannessen, N. C. Nielsen, and M. H. Levitt, Efficient dipolar recoupling in the NMR of rotating solids. A seven-fold symmetric radio-frequency pulse sequence, *Chem. Phys. Lett.* **242**, 304–309 (1995).

[42] W. P. Aue, D. J. Ruben, and R. G. Griffin, Uniform chemical shift scaling: application to 2D resolved NMR spectra of rotating powdered samples, *J. Chem. Phys.* **80**, 1729–1738 (1984).

[43] Y. Ishii, J. Ashida, and T. Terao, ^{13}C–^{1}H dipolar recoupling dynamics in ^{13}C multiple-pulse solid-state NMR, *Chem. Phys. Lett.* **246**, 439–445 (1995).

[44] M. Hohwy, C. M. Reinstra, C. P. Jaroniec, and R. G. Griffin, Fivefold symmetric homonuclear dipolar recoupling in rotating solids: Application to double quantum spectroscopy, *J. Chem. Phys.* **110**, 7983–7991 (1999).

[45] M. Carravetta, M. Edén, X. Zhao, A. Brinkmann, and M. H. Levitt, Symmetry principle for the design of radiofrequency pulse sequences in the nuclear magnetic resonance of rotating solids, *Chem. Phys. Lett.* **321**, 205–215 (2000).

[46] A. Brinkmann, and M. H. Levitt, Symmetry principle in the nuclear magnetic resonance of spinning solids: Heteronuclear recoupling by generalized Hartmann-Hahn sequences, *J. Chem. Phys.* **115**, 357–384 (2001).

[47] M. Hohwy, C. M. Rienstra, and R. G. Griffin, Bandselective homonuclear dipolar re-

coupling in rotating solids, *J. Chem. Phys.* **117**, 4973–4987 (2002).

[48] D. E. Demco, A. Johansson, and J. Tegenfeldt, Proton spin diffusion for spatial heterogeneity and morphology investigations of polymers, *Solid State NMR* **4**, 13–38 (1995).

[49] D. L. VanderHart, and G. B. McFadden, Some perspectives on the interpretation of proton NMR spin diffusion data in terms of polymer morphologies, *Solid State NMR* **7**, 45–66 (1996).

[50] P. Caravetti, P. Neuenschwander, R. R. Ernst, Characterization of heterogeneous polymer blends by two-dimensional proton spin diffusion spectroscopy, *Macromolecules* **18**, 119–122 (1985).

[51] D. Sakellariou, A. Lesage, and L. Emsley, Proton-proton constraints in powdered solids from ^{1}H–^{1}H–^{1}H and ^{1}H–^{1}H–^{13}C three-dimensional NMR chemical shift correlation spectroscopy, *J. Am. Chem. Soc.* **123**, 5604–5605 (2001).

CHAPTER 2

Recoupling of the ^{13}C–^{13}C DQ-Dipolar Interactions

2.1 Introduction

Solid-state NMR can provide information on structure and dynamics of molecules in non-crystalline states [1, 2] and membrane-associated forms [3, 4]. Efficient methods for spectral assignment [5, 6, 7, 8, 9], inter-nuclear distance measurement [10, 11, 12, 13, 14] and dihedral angle determination [15, 16, 17, 18, 19, 20, 21] include the use of dipolar interaction restored by RF multipulse irradiation under magic angle spinning [22]. Several RF pulse sequences have been designed to recouple zero-quantum (ZQ) [23, 24, 25, 26, 27, 28] and double-quantum (DQ) [29, 30, 31, 32, 33, 34, 35, 36, 37] components of the homonuclear dipolar interaction. The DQ dipolar interaction can be recoupled by rotor synchronous RF irradiation that rotates the dipolar spin operators about the B_1 field [9, 29, 37] or the z axis in the rotating frame [30, 31, 32, 33, 34, 35, 36]. General principles of the RF irradiation symmetry denoted as $\mathrm{C}N_n^\nu$ and $\mathrm{R}N_n^\nu$ allow the latter technique to recouple or decouple the dipolar interaction in homo- and hetero-nuclear spin systems [38, 39, 40, 41].

The RF pulse sequence with the $\mathrm{C}N_n^\nu$ symmetry consists of element pulses with RF phase shifts at $2\pi\nu/N$ steps during n rotor revolutions; here N, ν, and n are integers. The symmetries $\mathrm{C}7_2^1$ (POST-C7) [32], $\mathrm{C}5_2^1$ (SPC5) [33] and $\mathrm{C}14_4^5$ (SC14) [35] have been used for the ^{13}C–^{13}C DQ dipolar recoupling. These sequences are different in required RF amplitude relative to the sample spinning frequency, $\gamma B_1/\omega_\mathrm{R}$, but have broad recoupling bandwidths that cover the ^{13}C chemical shifts for organic molecules.

The band-selective recoupling can increase the signal sensitivity. It suppresses the interaction with spins outside the effective recoupling range [42]. The narrow band operation can be performed with an RF field amplitude lower than those for broadband operation

as shown in Ref.[43]. The reduced γB_1 facilitates the CH dipolar decoupling during the recoupling period under a strong RF field for ^{1}H [31].

In this paper, we propose element pulses for efficient band-selective DQ-dipolar recoupling. We have developed element pulses to vary the effective bandwidth of the CN recoupling sequence. A modification of the element pulse in POST-C7 has been shown to improve the tolerance to offset and RF field homogeneity [32]. The pulse we propose is a generalization of that modified pulse. We present an effective Hamiltonian to characterize the offset dependence of the recoupling with the element pulse. Subsequently, the proposed sequences are compared with broadband recoupling sequences. We demonstrate the advantages of the proposed sequences in band-selective magnetization transfer experiments on uniformly ^{13}C labeled amino acids.

2.2 Theory

2.2.1 Off-resonance effects on the recoupling

In the CN_n^ν sequence for recoupling the DQ dipolar interaction, N cyclic-element pulses are timed to span n rotor revolutions as illustrated in Fig.2.1(a). Each C-element pulse represents a 0° pulse with a width τ_c. The k-th element pulse has a phase $\phi_{rf}^{(k)} = 2\pi\nu k/N(k = 0, 1, 2, \ldots N-1)$. This RF phase rotation about the z axis is referred to as the z rotation [32]. It has been verified that the z-rotation symmetries $C7_2^1$, $C5_2^1$ and $C14_4^5$ recouple the homonuclear DQ- dipolar interactions [33, 35].

The Hamiltonian in the rotating frame for a dipolar-coupled homonuclear two-spin

system under the RF field along the x axis is expressed as

$$\mathcal{H} = \mathcal{H}_{\mathrm{A}} + \mathcal{H}_{\mathrm{B}}, \tag{2.1}$$

$$\mathcal{H}_{\mathrm{A}} = \boldsymbol{\omega}_1^{\mathrm{eff}}(t) \cdot \mathbf{I}_1 + \boldsymbol{\omega}_2^{\mathrm{eff}}(t) \cdot \mathbf{I}_2, \tag{2.2}$$

$$\mathcal{H}_{\mathrm{B}} = \Delta\omega_1^{\mathrm{aniso}}(t) I_{1z} + \Delta\omega_2^{\mathrm{aniso}}(t) I_{2z} + \omega_{\mathrm{D}}(t) \left(3 I_{1z} I_{2z} - \mathbf{I}_1 \cdot \mathbf{I}_2\right), \tag{2.3}$$

where $\boldsymbol{\omega}_j^{\mathrm{eff}} = (\omega_{\mathrm{RF}}(t), 0, \Delta\omega_{jz})$. The isotropic chemical shift and offset are included in $\Delta\omega_{jz}$, and the applied RF field is denoted by $\omega_{\mathrm{RF}}(t)$. The time and orientation dependence of the chemical shift anisotropy (CSA) is expressed as

$$\Delta\omega_j^{\mathrm{aniso}}(t) = \sum_{m=-2}^{2} \sum_{n=-2}^{2} A_{2n}^{(j)} D_{n,m}^{(2)} \left(\boldsymbol{\Omega}_{\mathrm{PR}}\right) d_{m,0}^{(2)} \left(\theta_{\mathrm{MAS}}\right) \exp\left(\mathrm{i}m\omega_{\mathrm{R}}t\right), \tag{2.4}$$

where $A_{2n}^{(j)}$ is the spherical tensor element for the chemical shift of spin j, $d_{m,0}^{(2)}(\theta_{\mathrm{MAS}})$ is a reduced Wigner rotation matrix element, θ_{MAS} is the magic angle and $\omega_{\mathrm{R}} = 2\pi/\tau_{\mathrm{R}}$ is the sample-spinning frequency. The Wigner rotation matrices $D_{m,m'}^{(2)}(\boldsymbol{\Omega}_{\mathrm{PR}})$ transform the tensor from the principal axis system to the rotor-fixed frame with Euler angles $\boldsymbol{\Omega}_{\mathrm{PR}}$. The dipolar coupling strength between the spins is expressed as

$$\omega_{\mathrm{D}}(t) = -\sum_{m=-2}^{2} b\, D_{0,m}^{(2)} \left(\boldsymbol{\Omega}_{\mathrm{PR}}\right) d_{m,0}^{(2)} \left(\theta_{\mathrm{MAS}}\right) \exp\left(\mathrm{i}m\omega_{\mathrm{R}}t\right), \tag{2.5}$$

with $b = \gamma^2\hbar\mu_0/4\pi r^3$, where γ and r are the gyromagnetic ratio and the internuclear distance, respectively [44].

The propagator for one RF phase modulation cycle $N\tau_{\mathrm{c}}$ is given by

$$U(N\tau_{\mathrm{c}}) = U_{\mathrm{A}}(N\tau_{\mathrm{c}}) U_{\mathrm{B}}(N\tau_{\mathrm{c}}) = \exp(-\mathrm{i}\overline{\mathcal{H}}_{\mathrm{A}} N\tau_{\mathrm{c}}) \exp(-\mathrm{i}\overline{\mathcal{H}}_{\mathrm{B}} N\tau_{\mathrm{c}}), \tag{2.6}$$

$$\exp(-\mathrm{i}\overline{\mathcal{H}}_{\mathrm{A}} N\tau_{\mathrm{c}}) = \mathcal{T} \exp\left(-\mathrm{i}\int_0^{N\tau_{\mathrm{c}}} \mathcal{H}_{\mathrm{A}}(t) dt\right), \tag{2.7}$$

$$\exp(-\mathrm{i}\overline{\mathcal{H}}_{\mathrm{B}} N\tau_{\mathrm{c}}) = \mathcal{T} \exp\left(-\mathrm{i}\int_0^{N\tau_{\mathrm{c}}} U_A^{\dagger}(t) \mathcal{H}_{\mathrm{B}}(t) U_A(t) dt\right), \tag{2.8}$$

where $\mathcal{T}$ is the Dyson time-ordering operator.

The residual spin rotation due to the offset for the k-th C-element pulse in Eq.(2.7) is expressed as

$$\mathcal{T}\exp\left(-\mathrm{i}\int_{(k-1)\tau_\mathrm{c}}^{k\tau_\mathrm{c}}\mathcal{H}_\mathrm{A}(t)dt\right)=\exp\left(-\mathrm{i}(\omega_1^\mathrm{eff}\mathbf{n}_1^{(k)}\cdot\mathbf{I}_1+\omega_2^\mathrm{eff}\mathbf{n}_2^{(k)}\cdot\mathbf{I}_2)\tau_\mathrm{c}\right), \tag{2.9}$$

with $\mathbf{n}_j^{(k)}\cdot\mathbf{I}_j=\hat{R}_z\left(2\pi kn/N\right)\mathbf{n}_j^{(0)}\cdot\mathbf{I}_j$, where $\hat{R}_z(\phi)\equiv\exp\left(-\mathrm{i}\phi\left(\hat{I}_{1z}+\hat{I}_{2z}\right)\right)$ is a rotation superoperator about the z axis and $\mathbf{n}_j^{(0)}$ is a rotation axis for the $k=0$ element. When k runs from 0 to $N-1$, the transverse components of the spin operators in Eq.(2.9) are rotated about the z axis. Thus the x and y components are averaged out to zero when $\omega_j^\mathrm{eff}\tau_\mathrm{c}\ll 1$. The resultant effective Hamiltonian is

$$\begin{aligned}\overline{\mathcal{H}}_\mathrm{A}&\approx\frac{1}{N\tau_\mathrm{c}}\sum_{k=0}^{N-1}\left(\omega_1^\mathrm{eff}\mathbf{n}_1^{(k)}\cdot\mathbf{I}_1+\omega_2^\mathrm{eff}\mathbf{n}_2^{(k)}\cdot\mathbf{I}_2\right)\\&\approx\omega_1^\mathrm{eff}n_{1z}I_{1z}+\omega_2^\mathrm{eff}n_{2z}I_{2z}.\end{aligned} \tag{2.10}$$

The lowest order term in the coherent averaging theory would provide a good approximate Hamiltonian for $\overline{\mathcal{H}}_\mathrm{B}$ in Eq.(2.8) as

$$\overline{\mathcal{H}}_\mathrm{B}\approx\frac{1}{N\tau_\mathrm{c}}\int_0^{N\tau_\mathrm{c}}U_\mathrm{A}^\dagger(t)\,\mathcal{H}_\mathrm{B}(t)\,U_\mathrm{A}(t)dt. \tag{2.11}$$

Only terms satisfying $mn-\mu\nu=NZ$ in Eq.(2.3) are not zero in $\overline{\mathcal{H}}_\mathrm{B}$ after averaging over $N\tau_\mathrm{c}$, where Z is an integer, m and μ are spatial- and spin-rotation indices in the spherical basis, and ν is the number of the phase revolution about the z axis during the CN sequence. We are interested in the effective Hamiltonian in an offset range where the DQ dipolar terms are larger than the other terms that are not commutable with the DQ spin operators. Thus we leave only the DQ terms for Eq.(2.11). The total effective Hamiltonian given by Eq.(2.6) is

$$\overline{\mathcal{H}}_\mathrm{eff}(N\tau_\mathrm{c})\approx\overline{\mathcal{H}}_\mathrm{A}+\overline{\mathcal{H}}_\mathrm{B}, \tag{2.12}$$

when higher order terms are neglected, i.e. $\left[\,\overline{\mathcal{H}}_{\rm A}, \overline{\mathcal{H}}_{\rm B}\,\right] N\tau_{\rm c} \ll \overline{\mathcal{H}}_{\rm A} + \overline{\mathcal{H}}_{\rm B}$, and

$$\overline{\mathcal{H}}_{\rm A} \approx \frac{\omega_\delta}{2}\left(I_{1z} - I_{2z}\right) + \frac{\omega_\sigma}{2}\left(I_{1z} + I_{2z}\right), \tag{2.13}$$

$$\overline{\mathcal{H}}_{\rm B} \approx \frac{\omega_{\rm DQ}}{2}\left(\mathrm{e}^{-\mathrm{i}(\gamma_{\rm PR}-\chi)} I_1^+ I_2^+ + \mathrm{e}^{\mathrm{i}(\gamma_{\rm PR}-\chi)} I_1^- I_2^-\right), \tag{2.14}$$

with $\omega_{\rm DQ} = \kappa b \sin(2\beta_{\rm PR})$, $\omega_\delta = \omega_1^{\rm eff} n_{1z} - \omega_2^{\rm eff} n_{2z}$ and $\omega_\sigma = \omega_1^{\rm eff} n_{1z} + \omega_2^{\rm eff} n_{2z}$. Here κ and χ denote the absolute value and the phase of the dipolar scaling factor, respectively. Note that this scaling factor depends on offsets, $\Delta\omega_{1z}$ and $\Delta\omega_{2z}$, as shown in Section 2.2.3. The supercycle consisting of two CN sequences, C$N\overline{\rm C}\overline{N}$ shown in Fig.2.1(a), further contributes to suppressing the x and y components of $\mathbf{I}_j$ in $\overline{\mathcal{H}}_{\rm A}$, and does not affect the DQ dipolar terms recoupled. We neglect terms originating from CSA in Eq.(2.14), since CSA is suppressed by CN and its supercycles [33].

The effective Hamiltonian in Eq.(2.12) transfers the magnetization from I_{1z} to I_{2z} as a function of the mixing time $\tau_{\rm m}$ (Appendix 2.7.1).

$$\begin{aligned} I_{1z} \xrightarrow{\overline{\mathcal{H}}_{\rm eff}} & \left(1 - \sin^2\phi_{\rm DQ}\sin^2 q\tau_{\rm m}\right) I_{1z} - \left(\sin^2\phi_{\rm DQ}\sin^2 q\tau_{\rm m}\right) I_{2z} \\ & + \frac{1}{4}\sin 2\phi_{\rm DQ}\left(-\cos 2q\tau_{\rm m} + 1\right)\hat{R}_z\Big(\frac{\gamma_{\rm PR}-\chi}{2}\Big)\left(I_1^+ I_2^+ + I_1^- I_2^-\right) \\ & - \frac{1}{2i}\sin\phi_{\rm DQ}\sin 2q\tau_{\rm m}\,\hat{R}_z\Big(\frac{\gamma_{\rm PR}-\chi}{2}\Big)\left(I_1^+ I_2^+ - I_1^- I_2^-\right), \end{aligned} \tag{2.15}$$

where $\phi_{\rm DQ} = \arctan(\omega_{\rm DQ}/\omega_\sigma)$ and $q = \sqrt{\left(\omega_\sigma^2 + \omega_{\rm DQ}^2\right)}/2$. The amplitude of the transferred magnetization is at its maximum at $\tau_{\rm m} = \pi/2q$. The maximum of the transferred magnetization $M_{\rm m}$ is expressed as a function of $r = \omega_\sigma/\omega_{\rm DQ} = \omega_\sigma/(\kappa b \sin 2\beta_{\rm PR})$ by

$$\begin{aligned} M_{\rm m}(r)/M_0 &= \sin^2\left(\arctan(r^{-1})\right) \\ &\approx 1 - r^2 + \frac{11}{12}r^4 - \frac{5}{12}r^6 + \ldots, \end{aligned} \tag{2.16}$$

where M_0 is the magnetization for I_{1z} at $\tau_{\rm m} = 0$. Equation (2.16) shows that the maximum $M_{\rm m}$ is determined by the pulse sequence through the scaling factor κ and the sum of the z components of the spin rotational frequencies, ω_σ. In an offset range where $r = \omega_\sigma/\omega_{\rm DQ} <$

0.5, M_{m} is larger than about 80 % of M_{m} at $\omega_\sigma = 0$.

2.2.2 Composite 0° pulses for band-selective recoupling

Equation (2.16) shows that the smaller z component of the residual spin rotation yields larger transferred magnetization. The x and y components of $\omega_j^{\mathrm{eff}}\mathbf{n}_j^{(k)}$ can be canceled by the z rotation as shown in Eq.(2.10). Thus, the element pulse should have the spin rotation axis $\mathbf{n}_j^{(k)}$ in the xy plane to maximize the transferred magnetization. To vary the effective bandwidth as a function of the flip angle, we designed a general composite pulses having the rotation axis in the xy plane.

We start with a phase alternating sequence consisting of two pulses with flip angle a, $(a)_0(a)_\pi$. The net spin rotation angle ϕ_{a} and its axis $\mathbf{n}_{\mathrm{a}}$ at offset $\Delta\omega_z$ for $(a)_0(a)_\pi$ can be analytically calculated as

$$\mathbf{n}_{\mathrm{a}} = \frac{1}{\sqrt{(1+L)(1-L)}} \begin{pmatrix} 0 \\ -\sin^2(a/2)\sin 2\theta \\ -\sin a\cos\theta \end{pmatrix} \tag{2.17}$$

$$\phi_{\mathrm{a}} = 2\cos^{-1} L, \tag{2.18}$$

where $L = \cos^2(a/2) - \sin^2(a/2)\cos 2\theta$ and $\tan\theta = \gamma B_1/\Delta\omega_z$ [45]. Equation (2.17) indicates that $(a)_0(a)_\pi$ has the effective rotation axis tilted from the y axis by ρ in the yz plane, here

$$\tan\rho = \frac{n_{\mathrm{a},z}}{n_{\mathrm{a},y}} = \frac{\cot(a/2)}{\sin\theta}. \tag{2.19}$$

This can approximately be solved for ρ under $\Delta\omega_z \ll \gamma B_1$ and $\pi \le a \le 2\pi$ as

$$\rho \approx -\frac{a}{2} - \frac{\pi}{2} + \frac{1}{4}\left(\theta - \frac{\pi}{2}\right)^2 \sin a. \tag{2.20}$$

The cyclic permutation by $-\rho$ (> 0) gave a new C-element pulse, $(\rho + a)_0(a)_\pi(-\rho)_0$. Since $\Delta\omega_z/\gamma B_1 << 1$, we can neglect the offset for the permuted pulse. The rotation of the new

element pulse is, therefore, expressed as [46]

$$\exp\left\{\mathrm{i}\rho\left(I_x+\frac{\Delta\omega_z}{\gamma B_1}I_z\right)\right\}\exp(\mathrm{i}\phi_\mathrm{a}\mathbf{n}_\mathrm{a}\mathbf{I})\exp\left\{-\mathrm{i}\rho\left(I_x+\frac{\Delta\omega_z}{\gamma B_1}I_z\right)\right\} \tag{2.21}$$

$$\approx \exp(\mathrm{i}\rho I_x)\exp(\mathrm{i}\phi_\mathrm{a}\mathbf{n}_\mathrm{a}\mathbf{I})\exp(-\mathrm{i}\rho I_x)$$

$$= \exp\left[\mathrm{i}\phi_\mathrm{a}\exp(\mathrm{i}\rho I_x)\mathbf{n}_\mathrm{a}\mathbf{I}\exp(-\mathrm{i}\rho I_x)\right]. \tag{2.22}$$

Thus the spin rotation axis of this pulse is approximately in the xy plane. Since $-\rho \approx a/2+\pi/2$, a generalized C-element pulse that suppresses the z spin rotation component is written as

$$\left(\frac{a}{2}-\frac{\pi}{2}\right)_0(a)_\pi\left(\frac{a}{2}+\frac{\pi}{2}\right)_0. \tag{2.23}$$

We refer to this element pulse as a C^z-element pulse. The same element pulse at $a=2\pi$, $(\pi/2)_0(2\pi)_\pi(2\pi/3)_0$, has been used in POST-C7 and SPC5 for the broadband DQ dipolar recoupling.

We calculate the rotations of a spin by the C$^z5$ and C$^z7$ sequences which denote $\mathrm{C}5_2^1$ and $\mathrm{C}7_2^1$ consisting of the C^z-element pulses. Figure 2.2 shows the net rotation angle $\phi=2\omega_j^\mathrm{eff}\tau_\mathrm{R}$ and its z component ϕn_z as a function of offset. The offset range where ϕ is suppressed varies with a. The C$^z5$ sequences reduce the rotational frequency $|\phi n_z/2\tau_\mathrm{R}|$ to less than $0.05\ \omega_\mathrm{R}$ in the range from -3.0 to $1.0\ \omega_\mathrm{R}$ at $a=300^\circ$ and that from -0.4 to $0.4\ \omega_\mathrm{R}$ at $a=210^\circ$. The z component dominates the spin rotation in the offset range where $\phi\approx\phi n_z$. In this offset range, the approximation to $\overline{\mathcal{H}}_\mathrm{A}$ in Eq.(2.10) is valid.

The RF field amplitude γB_1 increases with N as $\gamma B_1=2Na/n\tau_\mathrm{R}$ when $a/n\tau_\mathrm{R}$ is constant. The net rotation angle of the CN sequence, ϕ, increases with the number of element pulse in the sequence, N, if the spin rotation can be added linearly as shown in

Eq.(2.10). Therefore, the spin rotation of C7 at $\Delta\omega_z/\omega_\mathrm{R}$ is 7/5 times that of C5 at offset $(5/7)\Delta\omega_z/\omega_\mathrm{R}$ as can be seen from Fig.2.2. This means that ϕ/N as a function of $\Delta\omega_z/\gamma B_1$ is the same for C5 and C7 as revealed with the upper horizontal and right vertical scales in

Fig.2.2. Thus, the dependence of ϕ/N on $\Delta\omega_z/\gamma B_1$ for the $\mathrm{C}^z N$ sequence is determined not by the symmetry $\mathrm{C}N$ but by C^z-element pulse specified by flip angle a.

2.2.3 Dipolar scaling factor

The absolute value of the scaling factor κ can be factorized as

$$\kappa = \kappa_{\mathrm{rf}}\left(a, \mathrm{C}N_n\right)\kappa_z\left(\Delta\omega_{1z}, \Delta\omega_{2z}\right). \tag{2.24}$$

The factor κ_{rf} depends on the $\mathrm{C}N_n$ symmetry and the element pulse on resonance [39]. The offset also affects κ through κ_z that is normalized to unity at $\Delta\omega_{1z} = \Delta\omega_{2z} = 0$.

The on-resonance scaling factor κ_{rf} for a C^z-element pulse can be analytically derived as in Appendix 2.7.2, and its a dependence is shown in Fig.2.3. The minimum of κ_{rf} at $a \approx 270°$, 0.16, is about 30 % smaller than the maximum at $a \approx 450°$, 0.23 for $\mathrm{C}^z 5_2^1$. The dependence of κ_{rf} on the symmetry is also shown for $\mathrm{C}^z 5_3^1$ and $\mathrm{C}^z 7_2^1$.

The offset dependent factor κ_z was numerically calculated for the $\mathrm{SC}^z 5$ sequence at different a. The $\mathrm{SC}^z 5$ sequence has the phase modulation used in SPC5 as illustrated in Fig.2.1(a). Figure 2.4 shows κ_z as a function of resonance offsets for the spin pair. The factor κ_z is large along the line $\Delta\omega_{1z} \approx -\Delta\omega_{2z}$ for the element pulse at $a = 300°$ and $340°$. The terms proportional to $I_{1z} - I_{2z}$ and $I_{1z} + I_{2z}$ in $\mathcal{H}_{\mathrm{A}}$ are larger along the lines $\Delta\omega_{1z} \approx -\Delta\omega_{2z}$ and $\Delta\omega_{1z} \approx \Delta\omega_{2z}$, respectively. Since $I_{1z} + I_{2z}$ is not commutable with the DQ term but $I_{1z} - I_{2z}$ is, $\mathcal{H}_{\mathrm{A}}$ interferes with the DQ dipolar recoupling process in Eq.(2.11) for $\overline{\mathcal{H}}_{\mathrm{B}}$ along the line $\Delta\omega_{1z} \approx \Delta\omega_{2z}$ more than along the line $\Delta\omega_{1z} \approx -\Delta\omega_{2z}$.

2.2.4 Off-resonance effects on the magnetization transfer

The magnetization transfer calculated from the approximate Hamiltonian Eq.(2.12) qualitatively agrees with that obtained by the exact numerical computation. Figure 2.5 shows the offset dependence of the maximum of the magnetization transferred with SC^z5 consisting of the C^z-element pulses at $a = 210°$, $300°$ and $340°$ calculated by the two methods. This agreement confirms the validity of the analysis with κ and ω_σ.

The C^z-element pulse maximizes the magnetization transferred by the recoupled dipolar interaction. Figure 2.6 shows the maximum transferred magnetization numerically calculated for the SC5 sequence having C-element pulses $(a-x)_0(a)_\pi(x)_0$ for $180° \leq a \leq 450°$ and $x \leq a$ at a constant ω_R. The broken line indicating the C^z condition $x = a/2+\pi/2$ lies in a shaded region that yields large maxima in the transferred magnetization. The plot for the magnetization has another ridge along $x = (a/2+\pi/2)-\pi$, which also tilts the rotation axis into the xy plane.

The offset dependence of $|\omega_\sigma/\kappa_\mathrm{rf}b|$ for SC^z5 is shown in Fig.2.7. Since the magnetization transfer is a function of $\omega_\sigma/\omega_\mathrm{DQ}$ as shown by Eq.(2.16), the shaded regions in Figs.2.4 ($\kappa_z \geq 0.5$) and 2.7 ($|\omega_\sigma/\kappa_\mathrm{rf}b| \leq 0.5$) exhibit the offset regions favorable for the magnetization transfer. The effective regions in κ_z include those in $|\omega_\sigma/\kappa_\mathrm{rf}b|$ even for the element pulse at $a = 340°$ which has the largest area $|\omega_\sigma/\kappa_\mathrm{rf}b| \leq 0.5$. This means that the residual spin rotation frequency increases with offset faster than the recoupled DQ-dipolar coupling strength decreases. Therefore, the ratio $\omega_\sigma/\omega_\mathrm{DQ}$ depends more strongly on ω_σ, and the effective region for the magnetization transfer is limited by ω_σ rather than by κ. This is also confirmed by Fig.2.5 showing that the regions where the transferred magnetization is

larger than $0.5\,M_0$ are almost the same as those $|\omega_\sigma/\kappa_{\rm rf}b| \leq 0.5$ rather than those $\kappa_z \geq 0.5$. Figure 2.7 shows $|\omega_\sigma/\kappa_{\rm rf}b|$ for a ^{13}C spin pair at an internuclear distance 0.15 nm. For the pair at a longer distance, the effective offset region is smaller because of larger $|\omega_\sigma/\kappa_{\rm rf}b|$.

As seen in Figs.2.7(b) and (c), ω_σ for the element pulses $a = 300°$ and $340°$ has small absolute value along the anti-diagonal line $\Delta\omega_{1z} \approx -\Delta\omega_{2z}$ as expected from the spin rotation ϕn_z given in Fig.2.2. The scaling factor κ_z is large along the $\Delta\omega_{1z} \approx -\Delta\omega_{2z}$ as mentioned for Fig.2.4. Thus, the recoupling sequences allow the effective magnetization transfer along the anti-diagonal line.

Because the scaling factor κ is determined by the nutation of the DQ terms due to $\mathcal{H}_{\rm A}$ within a cycle of a CN sequence as shown by Eq.(2.11), κ is characterized by the spin dynamics on a time scale shorter than $N\tau_{\rm c}$. The scaling factor κ depends on the element pulse as well as the symmetry CN_n^ν as shown in Fig.2.3. Since ω_σ is obtained from the net spin rotations by an entire recoupling sequence, ω_σ is characterized by the dynamics on a time scale longer than $N\tau_{\rm c}$ [47]. The element pulse and the supercycle primarily determine ω_σ as mentioned for Fig.2.2. For example, the C^z-element pulse at $a = 360°$ used in POST-C7 suppresses ω_σ over an offset range broader than that for $(2\pi)_0(2\pi)_\pi$ in C7 without changing the scaling factor $\kappa_{\rm rf}$. The supercycles are also used to cancel ω_σ in SC14 and SPC5.

2.2.5 Modified SC^{z}5 for doubly selective magnetization transfer

By the use of the C^z-element pulse one can suppress the residual spin rotation frequency ω_σ over various offset range, and on this basis, one can confine the magnetization transfer to occur within a selected bandwidth around the irradiation frequency. The C^z-

element pulse can further be modified to establish the magnetization transfer in and between two separated bandwidths. The modified C^z-element pulse is written as

$$\left(\frac{a}{2} - \Delta\right)(a)\left(\frac{a}{2} + \Delta\right), \tag{2.25}$$

with $\Delta \neq \pi/2$. According to Eq.(2.16), the magnetization transfer should occur around the offset points where $\omega_\sigma = 0$ provided that the amplitude of the DQ-dipolar term ω_{DQ} is non-zero. With $\Delta \neq \pi/2$, ω_σ steeply increases in small offset, and is re-suppressed to zero at larger offset as shown in Fig.2.8. This feature may provide us an opportunity of establishing two (or more) separated effective bandwidths around offset points at which ω_σ crosses zero, and the magnetization should be transferred among spins in and between these separated frequency bandwidths. With such doubly-selective transfer band, one can transfer magnetization only between spins with large chemical shift difference, which is normaly not possible with broadband recoupling sequences.

2.2.6 Effects of chemical shifts on dipolar spectra

We have examined the effects of the isotropic and anisotropic chemical shifts of the aliphatic carbons on the dipolar scaling and the magnetization transfer. The simulated powder spectra in Fig.2.9 show the nutation frequency of the z magnetization by the recoupled dipolar interaction for $^{13}\mathrm{C}^\alpha$–$^{13}\mathrm{C}^\beta$ of alanine. The spectrum in Fig.2.9(a) was calculated for the broadband recoupling sequence SPC5, i.e. SC^z5 at $a = 360°$. The splitting of the doublet due to the DQ dipolar coupling is 830 Hz for the spin pair in alanine and 852 Hz for a pair with the identical shift on resonance. The spectrum shown in Fig.2.9(b) was calculated for the narrow-band recoupling sequence SC^z5 at $a = 210°$. The splitting of the spectrum is 752 Hz

for alanine and 820 Hz for the spin pair with the identical shift on resonance. The spectrum shown by the broken line in Fig.2.9(b) was calculated for SC^z5 at $a = 210°$ without the chemical shift anisotropy. The small difference between the spectra indicates effects of the anisotropy are negligible. Thus the isotropic chemical shifts for alanine reduce the effective coupling by less than 10%.

The isotropic chemical shifts suppress the spectral intensity near zero frequency and give the strong peak at zero frequency as shown in Fig.2.9(b). The frequency of the z field, ω_σ, is about 130 Hz, which can be obtained from the sum of the z- rotation frequencies at offset about 1.5 and -1.5 kHz in Fig.2.2(b). Equation (2.15) indicates that such ω_σ yields a nutation component with frequency $2q$ and amplitude proportional to $\sin^2\phi_{\mathrm{DQ}}$. Since $2q \geq \omega_\sigma$, the spectral intensity less than $\nu \approx 130$ Hz is eliminated.

Figure 2.9(c) shows the influence of the chemical shifts on the magnetization transfer. The effective bandwidth of the SC^z5 sequence at $a = 210°$ is about one sixth of that at $a = 360°$. This reduction in the bandwidth is accompanied by a decrease in the maximum transferred magnetization only by about 10%. The decreased transfer is due to the z field mainly caused by the isotropic chemical shifts.

2.3 Experimental Results

Advantages in using the band-selective recoupling sequences with the C^z-element pulses are demonstrated. The spectra shown in Fig.2.10 were obtained with the sequence in Fig.2.1(b) for monitoring the z magnetization transfer by the recoupled DQ-dipolar interactions. Figure 2.10(b) shows that the dipolar couplings transfer the $^{13}\mathrm{C}^\alpha$ magnetization to

$^{13}C^{\beta}$ and ^{13}CO under the broadband sequence SPC5 irradiated at the center of the chemical shifts of $^{13}C^{\beta}$ and ^{13}CO in uniformly labeled L-alanine at $\nu_{\mathrm{R}} = 10$ kHz. The irradiation frequency of SPC5 and the mixing time were selected so that they maximized the magnetization transferred to C^{β} for Fig.2.10(c). We made band-selective recoupling experiments by using the $\mathrm{SC}^{z}5$ sequence at $a = 210°$, which was irradiated to maximize the transfer to $^{13}C^{\beta}$. The maximum of the magnetization transferred to C^{β} with the band-selective sequence (Fig.2.10(d)) was 25% larger than that with the broadband sequence (Fig.2.10(c)). This enhancement under the selective sequence is due to decoupling of the ^{13}C–^{1}H dipolar interactions as well as unnecessary ^{13}C–^{13}C interactions. The selective operation decouples dipolar interaction between ^{13}C spins one of which is outside the effective range and permits the magnetization transfer only within the effective range. The $\mathrm{SC}^{z}5$ sequence at $a = 210°$ needs a ^{13}C RF field amplitude of 29.2 kHz which is smaller than the amplitude for SPC5, 50.0 kHz. This smaller recoupling field amplitude aids decoupling the CH dipolar interactions.

The C^{z}-element pulse can be used at faster sample spinning rates to increase the transferred magnetization in the aliphatic spectral region. We compared the $\mathrm{SC}^{z}5$ sequence at $a = 210°$ with SC14 whose mixing field amplitude is 1.4 times as smaller than that of SPC5. As shown in Fig.2.11(b), the DQ dipolar interaction recoupled under SC14 transferred the magnetization from C^{α} to all the other ^{13}C spins in uniformly labeled L-valine at ν_{R} =15 kHz. The irradiation frequency and the mixing time were adjusted in order to maximize the magnetization transferred to C^{β}. Figure 2.11(c) shows that the narrow bandwidth for $\mathrm{SC}^{z}5$ at $a = 210°$ increased the magnetization transferred from C^{α} to C^{β} and C^{γ} by excluding the carboxyl ^{13}C from the ^{13}C dipolar coupled spin network. The irradiation

frequency was set so as to maximize the C^{γ} signals. It is also possible to find a pulse width and an irradiation frequency experimentally that allow the magnetization to transfer only between C^{α} and C^{β} as shown in Fig.2.11(d). The maximum of the magnetization transferred from C^{α} to C^{β} with $SC^{z}5$ at $a = 210°$ was 100% larger than that with SC14 (Fig.2.11(b)). This enhancement would partly be due to the improved CH dipolar decoupling, because the RF field amplitude of the $SC^{z}5$ sequence, 43.8 kHz, is smaller than that of SC14, 52.5 kHz.

Figure 2.12 shows the offset dependence of the magnetization transferred from C^{α} to C^{β} in alanine at ν_{R} =10 kHz obtained with experiments and numerical simulations for the ^{13}C three-spin system. The $SC^{z}5$ sequence at $a = 210°$ has the bandwidth of about $0.5\,\omega_{\mathrm{R}}$ at $\gamma B_1 = 2.9\,\omega_{\mathrm{R}}$ as shown in Fig. 2.12(a). In Fig.2.12(c), the $SC^{z}5$ sequence at $a = 340°$ has the broadest bandwidth of about $3.0\,\omega_{\mathrm{R}}$ at $\gamma B_1 = 4.7\,\omega_{\mathrm{R}}$. This bandwidth is slightly larger than that for SPC5 (Fig.2.12(d)) at $\nu_{\mathrm{R}} = 10$ kHz. The

experimental magnetization was lower than calculated one at $a \geq 300°$, probably because of experimental imperfections such as residual CH dipolar interactions and RF inhomogeneity. We have also calculated the effect of ± 5 % rf field inhomogeneity on the transfer efficiency. The homogeneity does not have significant effects as shown by Fig.2.12

The modified C^{z}-element pulse shown in Eq.(2.25) can be used to transfer magnetization between two groups of spins with large chemical shift differences, such as groups of C^{α} and C=O spins. Figure 2.13(b) shows that the broadband dipolar recoupling sequence (SC14) transfers the $^{13}C^{\alpha}$ magnetization to both $^{13}C^{\beta}$ and ^{13}CO spins of L-alanine. The irradiation frequency of SC14 was set so as to maximize the magnetization transfer to ^{13}CO spin. Figure 2.13(c) shows the modified $SC^{z}5$ sequence with $a = 280°$ and $\Delta = 70°$ can transfer the magnetization on C^{α} only to C=O. The irradiation frequency was experi-

mentally optimized for the selectivity of the transfer. The magnetization transferred to C=O observed in Fig.2.13(c) was 30% larger than that observed in Fig.2.13(b). The transfer efficiency profile as a function of the offset observed with the same pulse sequence is shown in Fig.2.14(a). This indicates that the magnetization on C^{α} can be transferred either to C^{β} or C=O by adjusting the irradiation frequency. The numerical simulations shown in Figure 2.14(b) shows the dependence of the transferred magnetization on the chemical shift difference of two spins involved. Good transfer can be expected for spins with the chemical shift difference $\delta_{12} = 130 \pm 20$ ppm. The bandwidth of about 40 ppm is favorable to transfer magnetization between two spin groups with distributed chemical shifts.

2.4 Discussion

Faster sample spinning rates are necessary for reducing spinning sidebands at higher static magnetic fields and suppress ^{13}C–^{13}C dipolar couplings during the detection period. The faster spinning rates increase γB_1 that is applied synchronously with the sample spinning. However, a lower RF field amplitude is preferable for the CH decoupling and the reduction of the load on probe circuits. The recouping field amplitude required for the CN sequence is determined as $\gamma B_1 = \omega_{\mathrm{R}}(\theta_{\mathrm{tot}}/2\pi)N/n$. This equation shows that γB_1 can be reduced by decreasing the ratio N/n of the CN symmetry and/or the total flip angle θ_{tot} of the element pulse. The symmetries $\mathrm{C}5_2^1$ employed in SPC5 and $\mathrm{C}5_3^1$ reduce γB_1 for C7 by factors of 1.4 and 2.1, respectively. The C- element pulse $(2\pi)_0$ used in SC14 is twice shorter in θ_{tot} than that used in POST-C7, $(\pi/2)_0(2\pi)_\pi(3\pi/2)_0$, thereby reduces γB_1. The C^{z}-element pulses also reduce γB_1 with smaller θ_{tot}, when the required recoupling

bandwidth is smaller than the effective recoupling bandwidth of SC^z5 and C^z7 at $a = 360°$. The proposed C^z-element pulses can be combined with any CN symmetries.

We compare recoupling sequences in Fig.2.15 which exhibits effective bandwidths for DQ dipolar recoupling as a function of $\gamma B_1/\omega_\mathrm{R}$. The radii of the circles give the scaling factors for reference. The efficiency of the recoupling sequence can be measured by the effective bandwidth relative to γB_1 under complete CH dipolar decoupling. Recoupling sequences with the effective bandwidths $\Delta\omega_{z,\mathrm{rec}}/\gamma B_1 > 0.6$ are relatively efficient. The sequences SC^z14 at $a = 360°$, POST-C7, SC^z5 at $a =$ 340–400°, SC^z5_3, SC14 and HORROR are located in the efficient region. The pulse sequences SC^z14 at $a = 360°$ and POST-C7 need a high $\gamma B_1/\omega_\mathrm{R}$ and have the broadest effective bandsidth, $5.0\,\omega_\mathrm{R}$. The sequences SC^z5 at $a = 340°$ and SC14 have effective bandwidths of 4.0 and $2.5\,\omega_\mathrm{R}$, respectively, at lower $\gamma B_1/\omega_\mathrm{R}$. The C^z element specified by a makes the SC^z14 and SC^z5 sequence band-selective in a range from 5.0 to $0.5\,\omega_\mathrm{R}$ as shown by the lines in Fig.2.15. The efficiency of the C^zN sequence becomes small as the effective bandwidth decreases. Finally, HORROR is an efficient selective method with a bandwidth $0.5\,\omega_\mathrm{R}$ [29]. Numerical simulations at 0, ±5 and ±10 % rf field inhomogeneity indicated HORROR was more sensitive to the homogeneity than C^zN at $a = 210°$ in magnetization transfer (data not shown). HORROR has practically been used with the adiabatic sweep of the field strength to compensate for the resonance offset and RF field inhomogeneity [37]. Thus this adiabatic recoupling method needs a longer mixing time though HORROR has the highest scaling factor.

2.5 Conclusion

We have shown that the sum of the z-rotation frequencies ω_σ and the scaling factor κ characterize the DQ dipolar recoupling with the CN sequence. The theory and simulations revealed that the offset dependence of the DQ dipolar recoupling is primarily determined by ω_σ. For example, the recoupling pulse sequence SC^z5 consisting of the proposed C^z-element pulses can vary the bandwidth of the offset range where ω_σ is suppressed, yielding the effective recoupling bandwidth between $0.5\ \omega_\mathrm{R}$ and $4\ \omega_\mathrm{R}$ as a function of flip angle a.

These band-selective sequences can be applied to the correlation experiments on ^{13}C labeled aliphatic carbons in peptides and proteins for the signal assignment. The band-selective recoupling sequences are capable of limiting the propagation of the magnetization in the dipolar-coupled spin network and necessitate smaller γB_1. Consequently, the magnetization transferred with the selective sequence SC^z5 was larger than that with the broadband sequences SPC5 and SC14 as shown by the experimental spectra in Figs.2.10 and 2.11. The selective mixing could also be advantageous in obtaining higher resolution along the indirect detection axes in the multi-dimensional spectra, because it can suppress aliasing of signals outside the effective region. The selective recoupling of the DQ dipolar interaction is useful for spins with chemical shift differences much smaller than

ω_R. This selective recoupling is, therefore, complementary to RFDR [25, 26, 28] and narrowband RFDR [27] which favor the magnetization transfer for spin pairs with resonance frequency differences comparable to ω_R. The proposed sequences can also be applied to the INADEQUATE [33, 49] and DQ filter experiments [50].

2.6 Experimental

2.6.1 NMR experiments

Experiments were performed on a Varian Infinity-400 spectrometer at a ^{13}C resonance frequency of 100.1 MHz with a broadband double-resonance MAS probe for a 4 mm spinner. Only the spectra in Fig.2.11 were obtained with an Infinity plus-500 spectrometer at a ^{13}C frequency of 125.7 MHz. The carbon magnetization was prepared by cross polarization with the ^{13}C ramped RF amplitude from 55 to 65 kHz at $\nu_{\mathrm{R}} = 10$ kHz and from 50 to 60 kHz at $\nu_{\mathrm{R}} = 15$ kHz under the ^{1}H field amplitude of 70 kHz [51]. The amplitudes of 90° pulses were 70 kHz for ^{1}H and ^{13}C. The Gaussian selective pulse consisted of 17 rectangular pulses of 4 μs width separated by 40 μs intervals. The pulse sequences for Figs.2.11 b-d had a delay of $1/\nu_{\mathrm{R}}$ without the CH decoupling field immediately after the recoupling sequence. The spinning frequency was kept within a deviation of 0.1 %. Proton CW decoupling during the recoupling period was 100 kHz in $\gamma B_1/2\pi$. The TPPM decoupling [52] during the selective excitation and detection priods consisted of 170° pulses at a field strength of 85 kHz with a phase excursion of $\pm 7°$. The samples were uniformly 95 % ^{13}C, ^{15}N labeled L-alanine and L-valine (Shoko Co. Ltd, Japan) diluted to 10 % and 50 %, respectively, with natural abundance alanine and valine. The amounts of carbon-13 nuclei in the natural abundance and enriched samples were taken into account to evaluate the transferred magnetization.

2.6.2 Numerical simulation

The time evolution of the spin system was calculated by the numerical integration of a time-dependent Hamiltonian including terms for the ^{13}C-dipolar interactions, the isotropic and anisotropic chemical shifts, and the RF field. A total propagator for a 2π sample rotation was expressed as a product of about 100 element propagators that were calculated on the assumption of the time independence during the short piece-wise sections. The time-domain signals for about 1300 orientations were summed up to reproduce the powder distribution. The transferred magnetization as a function of the mixing time was computed as

$$M(\tau_{\rm m}) = \frac{M_0}{8\pi^2}\int_0^{2\pi}\int_0^{\pi}\int_0^{2\pi} {\rm Tr}\left\{I_{2z}U(\tau_{\rm m})I_{1z}U^{\dagger}(\tau_{\rm m})\right\} d\alpha_{\rm PR}\sin\beta_{\rm PR}d\beta_{\rm PR}d\gamma_{\rm PR}. \quad (2.26)$$

The dipolar spectra in Fig.2.9 were obtained by the Fourier transformation of the time-dependent sum magnetization, $I_{1z}+I_{2z}$, under the recoupling sequence for about 35×10^5 orientations. All numerical simulation programs coded in FORTRAN were rum on an SGI Origin200 workstation having four R10000 processors.

2.7 Appendices

2.7.1 Magnetization transfer under the effective Hamiltonian

The magnetization transfer under the effective Hamiltonian of Eq.(2.12) is analytically derived. The effective Hamiltonian is expressed as

$$\overline{\mathcal{H}}_{\text{eff}} = \omega_\delta I_z^{(23)} + \omega_\sigma I_z^{(14)} + \omega_{\text{DQ}} \hat{R}_z^{(14)}(\gamma_{\text{PR}} - \chi) I_x^{(14)}, \tag{2.27}$$

with the superoperator $\hat{R}_z^{(14)}(\epsilon) \equiv \exp\left(-\mathrm{i}\epsilon \hat{I}_z^{(14)}\right)$ and single transtion operators,

$$\begin{aligned} I_z^{(23)} &= \frac{1}{2}(I_{1z} - I_{2z}), & I_z^{(14)} &= \frac{1}{2}(I_{1z} + I_{2z}), \\ I_x^{(14)} &= \frac{1}{2}(I_1^+ I_2^+ + I_1^- I_2^-), & I_y^{(14)} &= \frac{1}{2\mathrm{i}}(I_1^+ I_2^+ - I_1^- I_2^-). \end{aligned} \tag{2.28}$$

This Hamiltonian can be diagonalized by the unitary transformation

$$U = \exp\left(-\mathrm{i}\phi_{\text{DQ}} I_y^{(14)}\right), \tag{2.29}$$

with $\phi_{\text{DQ}} = \arctan(\omega_{\text{DQ}}/\omega_\sigma)$, and has four eigenvalues,

$$\begin{aligned} E_1 &= \frac{1}{2}\sqrt{\omega_\sigma^2 + \omega_{\text{DQ}}^2} = q, & E_2 &= \frac{1}{2}\omega_\delta, \\ E_3 &= -\frac{1}{2}\omega_\delta, & E_4 &= -q. \end{aligned} \tag{2.30}$$

Here, the energy difference $E_1 - E_4 = 2q$ determines the evolution frequency under the recoupled DQ-dipolar interaction.

The time-dependence of the magnetization during the mixing period can be expressed as a rotation of the density operator in DQ subspace at the frequency $2q$ about an axis inclined from $I_z^{(14)}$ by ϕ_{DQ} in the plane formed by $I_x^{(14)}$ and $I_z^{(14)}$ at $\gamma_{\text{PR}} - \chi = 0$. When the initial state is I_{1z}, the propagator for $\mathcal{H}_{\text{eff}}$, U_{eff}, provides the density operator at the mixing time τ_{m} as

$$\sigma(\tau_{\text{m}}) = U_{\text{eff}}(\tau_{\text{m}})\, I_{1z} U_{\text{eff}}^{-1}(\tau_{\text{m}}). \tag{2.31}$$

The time dependence of the magnetization transferred from I_{1z} to I_{2z} is written as

$$\mathrm{Tr}\left\{I_{2z}\sigma(\tau_{\mathrm{m}})\right\} = -\sin^2\phi_{\mathrm{DQ}}\sin^2 q\tau_{\mathrm{m}}. \tag{2.32}$$

Thus the transferred magnetization reaches the maximum in amplitude, $\sin^2\phi_{\mathrm{DQ}}$, at $\tau_{\mathrm{m}} = \pi/2q$. Similar relations are found for the magnetization transfer in the ZQ subspace [53].

2.7.2 Scaling factors

We derive the scaling factor on resonance for the CN sequence consisting of C-element pulses expressed by $(a-x)_0(a)_\pi(x)_0$. The scaling factor for the DQ dipolar term with $\mu = 2$ and m is defined as

$$\kappa_{\mathrm{rf}}\mathrm{e}^{\mathrm{i}\chi} = \frac{1}{\tau_{\mathrm{c}}}\int_0^{\tau_{\mathrm{c}}} d_{20}^{(2)}\left(\beta_{\mathrm{RF}}(t)\right)\mathrm{e}^{\mathrm{i}m\omega_{\mathrm{R}}t}dt, \tag{2.33}$$

where κ_{rf} and χ represent the absolute value and the phase of the scaling factor [39]. When the time-dependent spin rotation angle $\beta_{\mathrm{PR}}(t)$ is written as

$$\begin{aligned}
\beta_{\mathrm{PR}}(t) &= 2a\frac{t}{\tau_{\mathrm{c}}}, && \text{if} \quad 0 \le t < f/\tau_{\mathrm{c}} \\
&= 2a\left(2f - \frac{t}{\tau_{\mathrm{c}}}\right), && \text{if} \quad f\tau_{\mathrm{c}} \le t < (f+0.5)\tau_{\mathrm{c}} \\
&= 2a\left(\frac{t}{\tau_{\mathrm{c}}} - 1\right), && \text{if} \quad (f+0.5)\tau_{\mathrm{c}} \le t < \tau_{\mathrm{c}}
\end{aligned} \tag{2.34}$$

with $f = (a-x)/2a$, the scaling factor κ_{rf} is given by

$$\kappa_{\mathrm{rf}} = \frac{3}{4\sqrt{2}} \times \frac{aN^2}{(2aN)^2 - (mn\pi)^2} \times \sqrt{A^2 + B^2}, \tag{2.35}$$

where

$$\begin{aligned}
A = \frac{aN}{n\pi}\sin\left(\frac{2\pi mn}{N}\right) - \sin(4af)\cos\left(f\frac{2\pi mn}{N}\right) \\
+ \sin(4af - 2a)\cos\left((f+0.5)\frac{2\pi mn}{N}\right),
\end{aligned} \tag{2.36}$$

$$B = \frac{aN}{n\pi}\left(1-\cos\left(\frac{2\pi mn}{N}\right)\right) - \sin(4af)\sin\left(f\frac{2\pi mn}{N}\right) + \sin(4af-2a)\sin\left((f+0.5)\frac{2\pi mn}{N}\right). \quad (2.37)$$

These equations for A and B are reduced to

$$\kappa_{\mathrm{rf}} = \frac{3}{8\sqrt{2}} \times \frac{N^3}{\pi(4N^2-1)} \times \sqrt{\sin^2\left(\frac{4\pi}{N}\right) + \left\{1-\cos\left(\frac{4\pi}{N}\right)\right\}^2} \quad (2.38)$$

at $(a, x) = (360°, 270°)$, $m = 1$ and $n = 2$. This result Eq.(2.38) agrees with the scaling factor obtained previously [32].

REFERENCES

[1] F. J. Blanco, S. Hess, L. K. Pannell, N. W. Rizzo, and R. Tycko, Solid-state NMR data support a helix-loop-helix structural model for the N-terminal half of HIV-1 Rev in fibrillar form, *J. Mol. Biol.* **313**, 845–859 (2001).

[2] T. S. Burkoth, T. L. S. Benzinger, V. Urban, D. M. Morgan, D. M. Gregory, P. Thiyagarajan, R. E. Botto, S. C. Meredith, and D. G. Lynn, Structure of the β-amyloid$_{(10-35)}$ fibril, *J. Am. Chem. Soc.* **122**, 7883–7889 (2000).

[3] H. J. M. de Groot, Solid-state NMR spectroscopy applied to membrane proteins, *Curr. Opin. Struct. Biol.* **10**, 593–600 (2000).

[4] J. Kikuchi, M. P. Williamson, K. Shimada, and T. Asakura, Structure and dynamics of photosynthetic membrane-bound proteins in *Rhodobacter Sphaeroides*, studied with solid-state NMR spectroscopy, *Photosynth. Res.* **63**, 259–267 (2000).

[5] T. Fujiwara, K. Sugase, M. Kainosho, A. Ono, A. (M.) Ono, and H. Akutsu, ^{13}C–^{13}C and ^{13}C–^{15}N dipolar correlation NMR of uniformly labeled organic solids for the complete assignment of their ^{13}C and ^{15}N signals: An application to adenosine, *J. Am. Chem. Soc.* **117**, 11351–11352 (1995).

[6] C. M. Rienstra, M. Hohwy, M. Hong, and R. G. Griffin, 2D and 3D ^{15}N–^{13}C–^{13}C NMR chemical shift correlation spectroscopy of solids: Assignment of MAS spectra of

peptides, *J. Am. Chem. Soc.* **122**, 10979–10990 (2000).

[7] A. McDermott, T. Polenova, A. Bockmann, K. W. Zilm, E. K. Paulsen, R. W. Martin, and G. T. Montelione, Partial NMR assignments for uniformly (^{13}C, ^{15}N)-enriched BPTI in the solid state, *J. Biomol. NMR* **16**, 209–219 (2000).

[8] B.-J. van Rossum, F. Castellani, K. Rehbein, J. Pauli, and H. Oschkinat, Assignment of the nonexchanging protons of the α-spectrin SH3 domain by two- and three-dimensional ^{1}H–^{13}C solid-state magic-angle spinning NMR and comparison of solution and solid-state proton chemical shifts, *Chembiochem* **2**, 906–914 (2001).

[9] A. Detken, E. H. Hardy, M. Ernst, M. Kainosho, T. Kawakami, S. Aimoto, and B .H. Meier, Methods for sequential resonance assignment in solid, uniformly ^{13}C, ^{15}N labeled peptides: Quantification and application to antamanide, *J. Biomol. NMR* **20**, 203–221 (2001).

[10] O. B. Peersen, M. Groesbeek, S. Aimoto, and S. O. Smith, Analysis of rotational resonance magnetization exchange curves from crystalline peptides, *J. Am. Chem. Soc.* **117**, 7228–7237 (1995).

[11] D. R. Studelska, C. A. Klug, D. D. Beusen, L. M. McDowell, and J. Schaefer, Long-range distance measurements of protein binding sites by rotational-echo double-resonance NMR, *J. Am. Chem. Soc.* **118**, 5476–5477 (1996).

[12] S. Kiihne, M. A. Mehta, J. A. Stringer, D. M. Gregory, J. C. Shiels, and G. P. Drobny, Distance measurements by dipolar recoupling two-dimensional solid-state NMR, *J. Phys. Chem. A* **102**, 2274–2282 (1998).

[13] C. A. Fyfe and A. R. Lewis, Investigation of the viability of solid-state NMR distance determinations in multiple spin systems of unknown structure, *J. Phys. Chem. B* **104**,

48–55 (2000).

[14] O. J. Murphy III, F. A. Kovacs, E. L. Sicard, and L. K. Thompson, Site-directed solid-state NMR measurement of a ligand-induced conformational change in the serine bacterial chemoreceptor, *Biochemistry* **40**, 1358–1366 (2001).

[15] Y. Ishii, T. Terao, and M. Kainosho, Relayed anisotropy correlation NMR: Determination of dihedral angles in solids, *Chem. Phys. Lett.* **256**, 133–140 (1996).

[16] T. Fujiwara, T. Shimomura, and H. Akutsu, Multidimensional solid-state nuclear magnetic resonance for correlating anisotropic interactions under magic-angle spinning conditions, *J. Magn. Reson.* **124**, 147–153 (1997).

[17] M. Hong, J. D. Gross, and R. G. Griffin, Site-resolved determination of peptide torsion angle ϕ from the relative orientation of backbone N-H and C-H bonds by solid-state NMR, *J. Phys. Chem. B* **101**, 5869–5874 (1997).

[18] T. Fujiwara, T. Shimomura, Y. Ohigashi, and H. Akutsu, Multidimensional solid-state nuclear magnetic resonance for determining the dihedral angle from the correlation of ^{13}C–^{1}H and ^{13}C–^{13}C dipolar interactions under magic-angle spinning conditions, *J. Chem. Phys.* **109**, 2380–2393 (1998).

[19] X. Feng, P. J. E. Verdegem, M. Edén, D. Sandström, Y. K. Lee, P. H. M. Bovee-Geurts, W. J. de Grip, J. Lugtenburg, H. J. M de Groot, and M. H. Levitt, Determination of a molecular torsional angle in the metarhodopsin-I photointermediate of rhodopsin by double-quantum solid-state NMR, *J. Biomol. NMR* **16**, 1–8 (2000).

[20] B. Reif, M. Hohwy, C. P. Jaroniec, C. M. Rienstra, and R. G. Griffin, NH-NH vector correlation in peptides by solid-state NMR, *J. Magn. Reson.* **145**, 132–141 (2000).

[21] K. Nomura, K. Takegoshi, T. Terao, K. Uchida, and M. Kainosho, Three-dimensional

structure determination of a uniformly labeled molecule by frequency-selective dipolar recoupling under magic-angle spinning, *J. Biomol. NMR* **17**, 111–123 (2000).

[22] R. G. Griffin, Dipolar recoupling in MAS spectra of biological solids, *Nature Struc. Biol.* NMR supplement, 508–512 (1998).

[23] M. H. Levitt, D. P. Raleigh, F. Creuzet, and R. G. Griffin, Theory and simulations of homonuclear spin pair systems in rotating solids, *J. Chem. Phys.* **92**, 6347–6364 (1990).

[24] T. Fujiwara, A. Ramamoorthy, K. Nagayama, K. Hioka, and T. Fujito, Dipolar HOHAHA under MAS conditions for solid-state NMR, *Chem. Phys. Lett.* **212**, 81–84 (1993).

[25] A. E. Bennett, C. M. Rienstra, J. M. Griffiths, W. Zhen, P. T. Lansbury Jr., and R. G. Griffin, Homonuclear radio frequency-driven recoupling in rotating solids, *J. Chem. Phys.* **108**, 9463–9479 (1998).

[26] T. Fujiwara, P. Khandelwal, and H. Akutsu, Compound radio frequency-driven recoupling pulse sequence for efficient magnetization transfer by homonuclear dipolar interaction under MAS conditions, *J. Magn. Reson.* **145**, 73–83 (2000).

[27] G. Goobes, G. J. Boender, and S. Vega, Spinning-frequency-dependent narrowband RF-driven dipolar recoupling, *J. Magn. Reson.* **146**, 204–219 (2000).

[28] Y. Ishii, ^{13}C–^{13}C dipolar recoupling under very fast magic angle spinning in solid-state nuclear magnetic resonance: Applications to distance measurements, spectral assignments, and high-throughput secondary-structure determination, *J. Chem. Phys.* **114** 8473–8483 (2001).

[29] N. C. Nielsen, H. Bildsøe, H. J. Jakobsen, and M. H. Levitt, Double-quantum homonuclear rotary resonance: Efficient dipolar recovery in magic-angle spinning nuclear mag-

netic resonance, *J. Chem. Phys.* **101**, 1805–1812 (1994).

[30] Y. K. Lee, N. D. Kurur, M. Helmle, O. G. Johannessen, N. C. Nielsen, and M. H. Levitt, Efficient dipolar recoupling in the NMR of rotating solids. A seven-fold symmetric radio-frequency pulse sequence, *Chem. Phys. Lett.* **242**, 304–309 (1995).

[31] C. M. Rienstra, M. E. Hatcher, L. J. Mueller, B. Sun, S. W. Fesik, and R. G. Griffin, Efficient multispin homonuclear double-quantum recoupling for magic-angle spinning NMR: ^{13}C–^{13}C correlation spectroscopy of U-^{13}C-erythromycin A, *J. Am. Chem. Soc.* **120**, 10602–10612 (1998).

[32] M. Hohwy, H. J. Jakobsen, M. Edén, M. H. Levitt, and N. C. Nielsen, Broadband dipolar recoupling in the nuclear magnetic resonance of rotating solids: A compensated C7 pulse sequence, *J. Chem. Phys.* **108**, 2686–2694 (1998).

[33] M. Hohwy, C. M. Reinstra, C. P. Jaroniec, and R. G. Griffin, Fivefold symmetric homonuclear dipolar recoupling in rotating solids: Application to double quantum spectroscopy, *J. Chem. Phys.* **110**, 7983–7991 (1999).

[34] M. Carravetta, M. Edén, X. Zhao, A. Brinkmann, and M. H. Levitt, Symmetry principles for the design of radiofrequency pulse sequence in the nuclear magnetic resonance of rotating solids, *Chem. Phys. Lett.* **321**, 205–215 (2000).

[35] A. Brinkmann, M. Edén, and M. H. Levitt, Synchronous helical pulse sequences in magic-angle spinning nuclear magnetic resonance: Double quantum recoupling of multiple-spin systems, *J. Chem. Phys.* **112**, 8539–8554 (2000).

[36] I. Schnell and A. Watts, Towards selective recoupling and mutual decoupling of dipolar-coupled spin pairs in double-quantum magic-angle spinning NMR experiments on multiply labeled solid-state samples, *Chem. Phys. Lett.* **335**, 111–122 (2001).

[37] R. Verel, M. Ernst, and B. H. Meier, Adiabatic dipolar recoupling in solid-state NMR: The DREAM scheme, *J. Magn. Reson.* **150**, 81–99 (2001).

[38] M. Edén and M. H. Levitt, Pulse sequence symmetries in the nuclear magnetic resonance of spinning solids: Application to heteronuclear decoupling, *J. Chem. Phys.* **111**, 1511–1519 (1999).

[39] A. Brinkmann and M. H. Levitt, Symmetry principles in the nuclear magnetic resonance of spinning solids: Heteronuclear recoupling by generalized Hartmann-Hahn sequences, *J. Chem. Phys.* **115**, 357–384 (2001).

[40] P. K. Madhu, X. Zhao, and M. H. Levitt, High-resolution ^{1}H NMR in the solid state using symmetry-based pulse sequences, *Chem. Phys. Lett.* **346**, 142–148 (2001).

[41] P. E. Kristiansen, D. J. Mitchell, and J. N. S. Evans, Double-quantum dipolar recoupling at high magic-angle sipnning rates, *J. Magn. Reson.* **157**, 253–266 (2002).

[42] M. Baldus, A. T. Petkova, J. Herzfeld, and R. G. Griffin, Cross polarization in the tilted frame: Assignment and spectral simplification in heteronuclear spin systems, *Mol. Phys.* **95**, 1197–1207 (1998).

[43] M. Hohwy, C. M. Rienstra, and R. G. Griffin, Bandselective homonuclear dipolar recoupling in rotating solids, *J. Chem. Phys.* **117**, 4973–4987 (2002).

[44] M. Mehring, *Principles of High Resolution NMR in Solids* (Springer-Verlag, New York, 1983).

[45] C. Counsell, M. H. Levitt, and R. R. Ernst, Analytical theory of composite pulses, *J. Magn. Reson.* **63**, 133–141 (1985).

[46] M. H. Levitt, Composite pulses, *Prog. Nuc. Magn. Reson. Spectrosc.* **18**, 61–122 (1986).

[47] T. Fujiwara and K. Nagayama, Efficiency of heteronuclear broadband decoupling and

homonuclear J cross polarization analyzed on two time scales, *J. Magn. Reson.* **81**, 245–254 (1989).

[48] A. Naito, S. Ganapathy, K. Akasaka, and C. A. McDowell, Chemical shielding tensor and ^{13}C–^{14}N dipolar splitting in single crystals of L-alanine, *J. Chem. Phys.* **74**, 3190–3197 (1981).

[49] M. Hong, Solid-state dipolar INADEQUATE NMR spectroscopy with a large double-quantum spectral width, *J. Magn. Reson.* **136**, 86–91 (1999).

[50] A. S. D. Heindrichs, H. Geen, and J. J. Titman, MAS double-quantum filtered dipolar shift correlation spectroscopy, *J. Magn. Reson.* **147**, 68–77 (2000).

[51] G. Metz, X. Wu, and S. O. Smith, Ramped-amplitude cross polarization in magic-angle-spinning NMR, *J. Magn. Reson. A* **110**, 219–277 (1994).

[52] A. E. Bennett, C. M. Rienstra, M. Auger, K. V. Lakshmi, and R. G. Griffin, Heteronuclear decoupling in rotating solids, *J. Chem. Phys.* **103**, 6951–6958 (1995).

[53] L. Müller and R. R. Ernst, Coherence transfer in the rotating frame: Application to heteronuclear cross-correlation spectroscopy, *Mol. Phys.* **38**, 963–992 (1979).

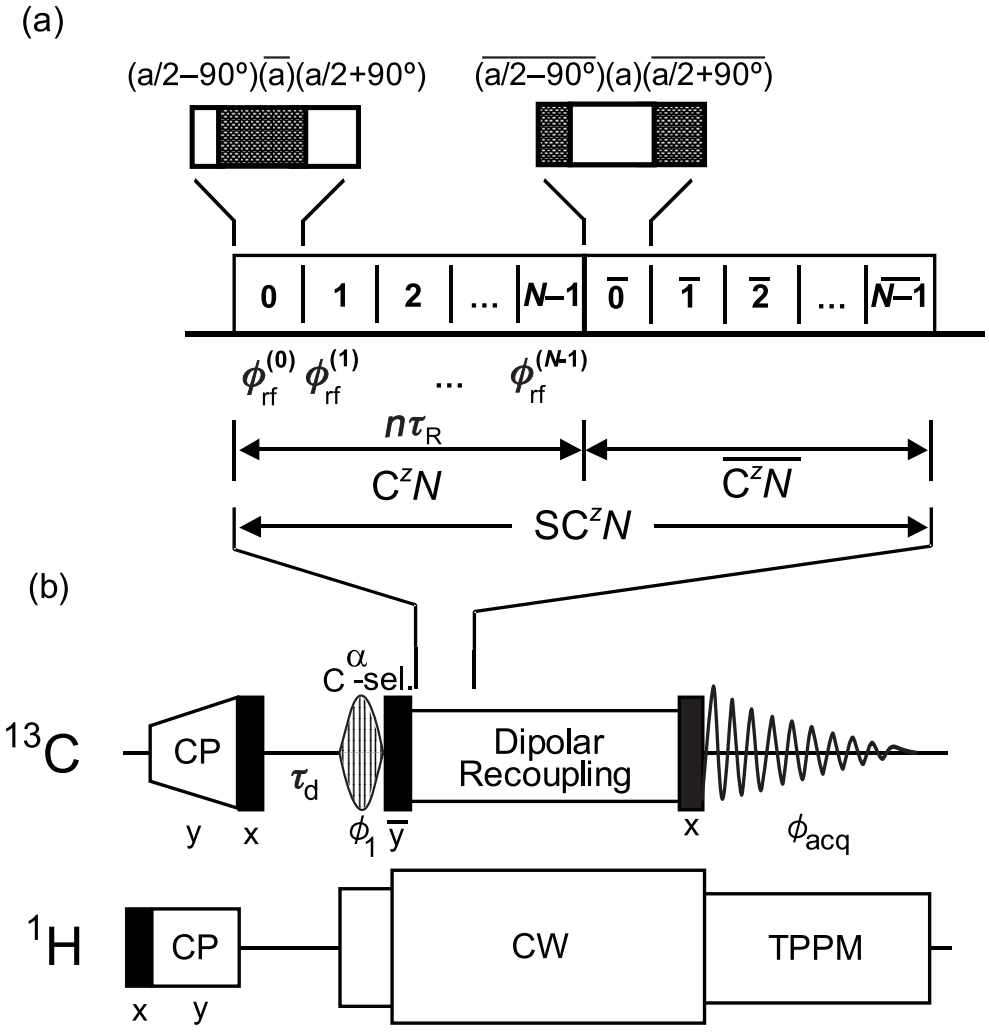

Figure 2.1: Pulse sequence SC^zN consisting of the C^z-element pulses for DQ dipolar recoupling (a), and sequence for selective magnetization transfer (b). (a) The element pulses are phase shifted N times in $\mathrm{C}N_n^\nu$. The sequence SC^zN denotes $\mathrm{C}^zN\overline{\mathrm{C}^zN}$. The upper bars represent 180° shifts of the RF phase. In the sequence (b), the ^{13}C magnetization cross-polarized from the ^{1}H magnetization is flipped to the z direction, and the residual transverse components decays during $\tau_\mathrm{d} = 10$ ms by the CH dipolar interaction. The dark pulses represent 90° pulses. The Gaussian 90° and the subsequent 90° pulses with a phase cycle prepare the z magnetization only at C^α. The z magnetiztion after the mixing period is read out by the final 90° pulse. The CH dipolar interactions are decoupled by a proton CW field during the recoupling period and by the TPPM sequence during the selective excitation and detection periods. The phase cycles are $\phi_1 = y, \overline{y}$ and $\phi_\mathrm{acq} = x, \overline{x}$.

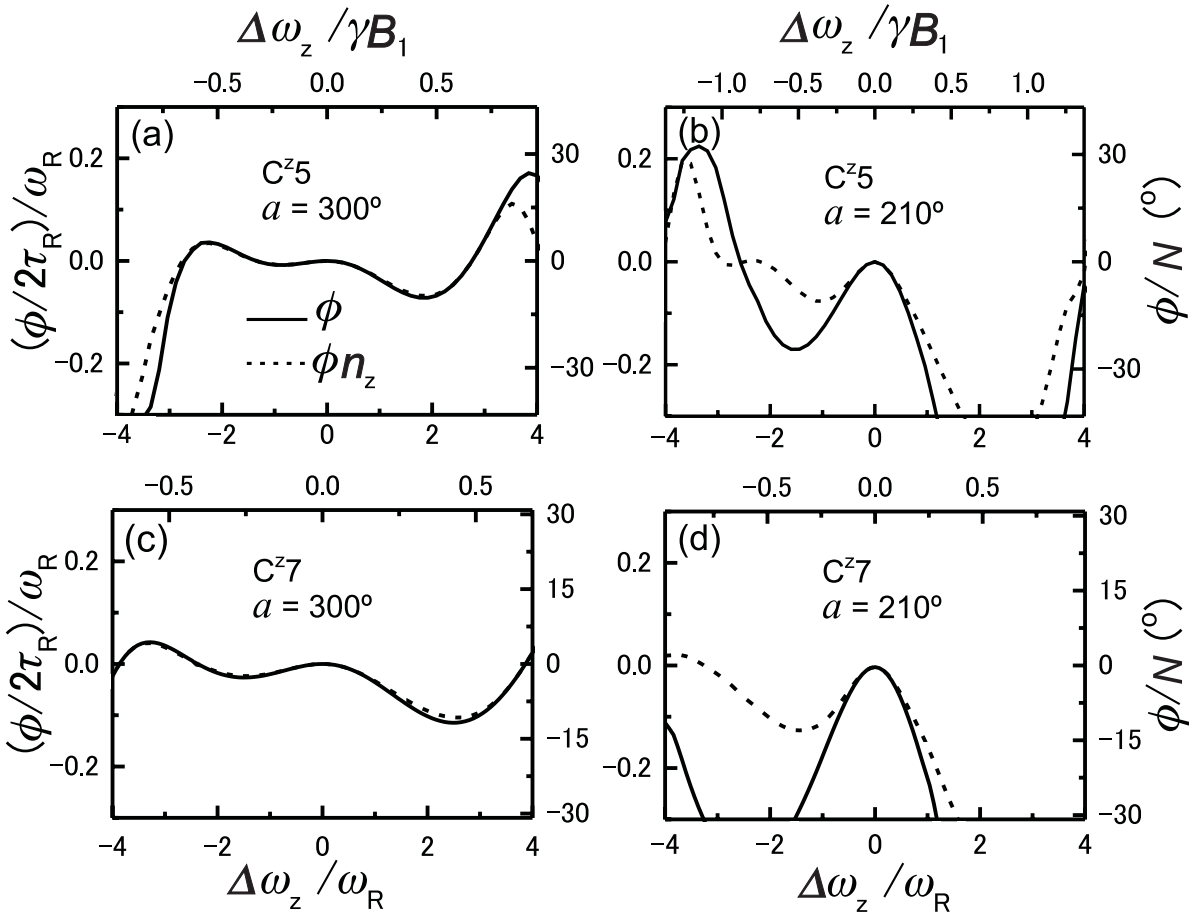

Figure 2.2: The residual spin rotational frequency (solid lines) and its z component (broken lines) as a function of offset. The rotations are given for the C^z5 sequence at $a = 300°$ (a) and 210° (b), and the C^z7 sequence $a = 300°$ (c) and 210° (d). When ν_{R} =10 kHz, $\gamma B_1/2\pi$ is 41.7, 29.2, 58.3 and 40.8 kHz for (a), (b), (c), and (d), respectively. The lower horizontal and left vertical axes show scales normalized by ω_{R}, and the upper horizontal axis shows a scale normalized by γB_1. The vertical axis on the right gives the net spin rotation angle ϕ divided by N.

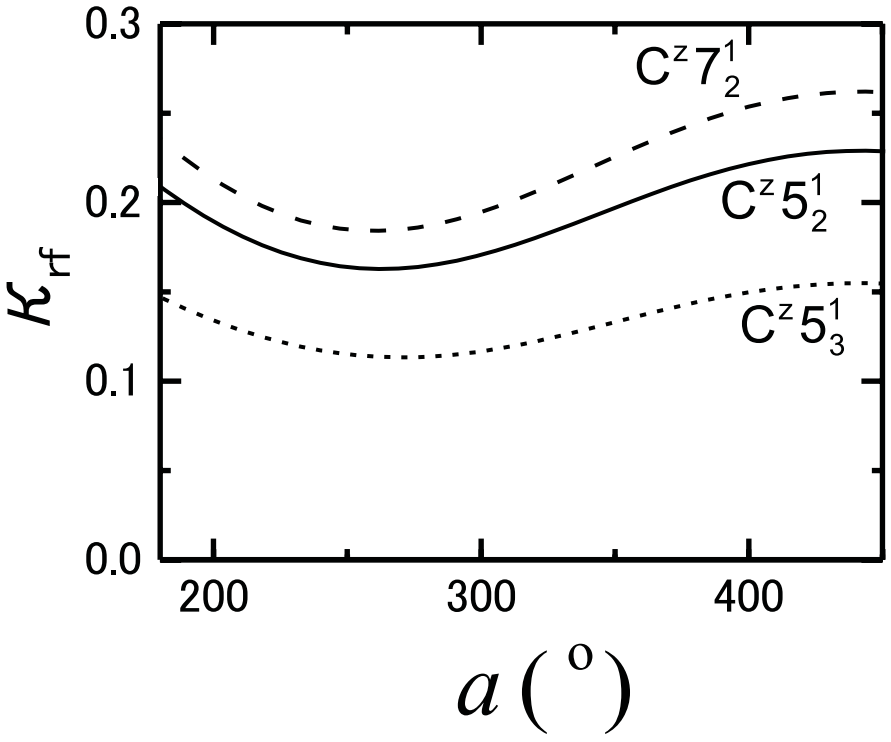

Figure 2.3: Scaling factor $\kappa_{\rm rf}(a, {\rm C}N_{\rm n})$ for a ${\rm C}^z$-element pulse under the on-resonance condition as a function of flip angle a. Scaling factors for ${\rm C}7_2^1$, ${\rm C}5_2^1$ and ${\rm C}5_3^1$ are shown with broken, solid and dotted lines, respectively.

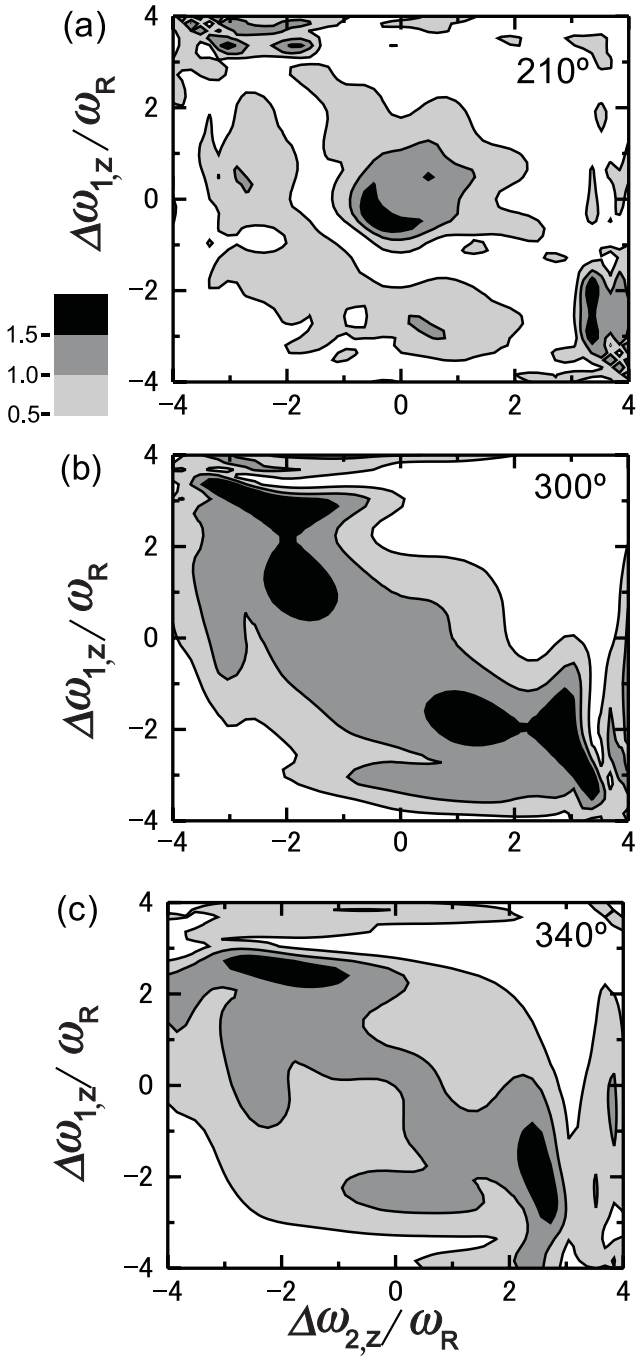

Figure 2.4: Contour plots of the scaling factor κ_z as a function of offsets of a pair of carbon spins with an internuclear distance of 0.15 nm. Scaling factor were numerically calculated for the SC^z5 sequence with $a = 210°$ (a), 300° (b), and 340° (c). The regions $\kappa_z \geq 0.5$ are shaded as the indicator.

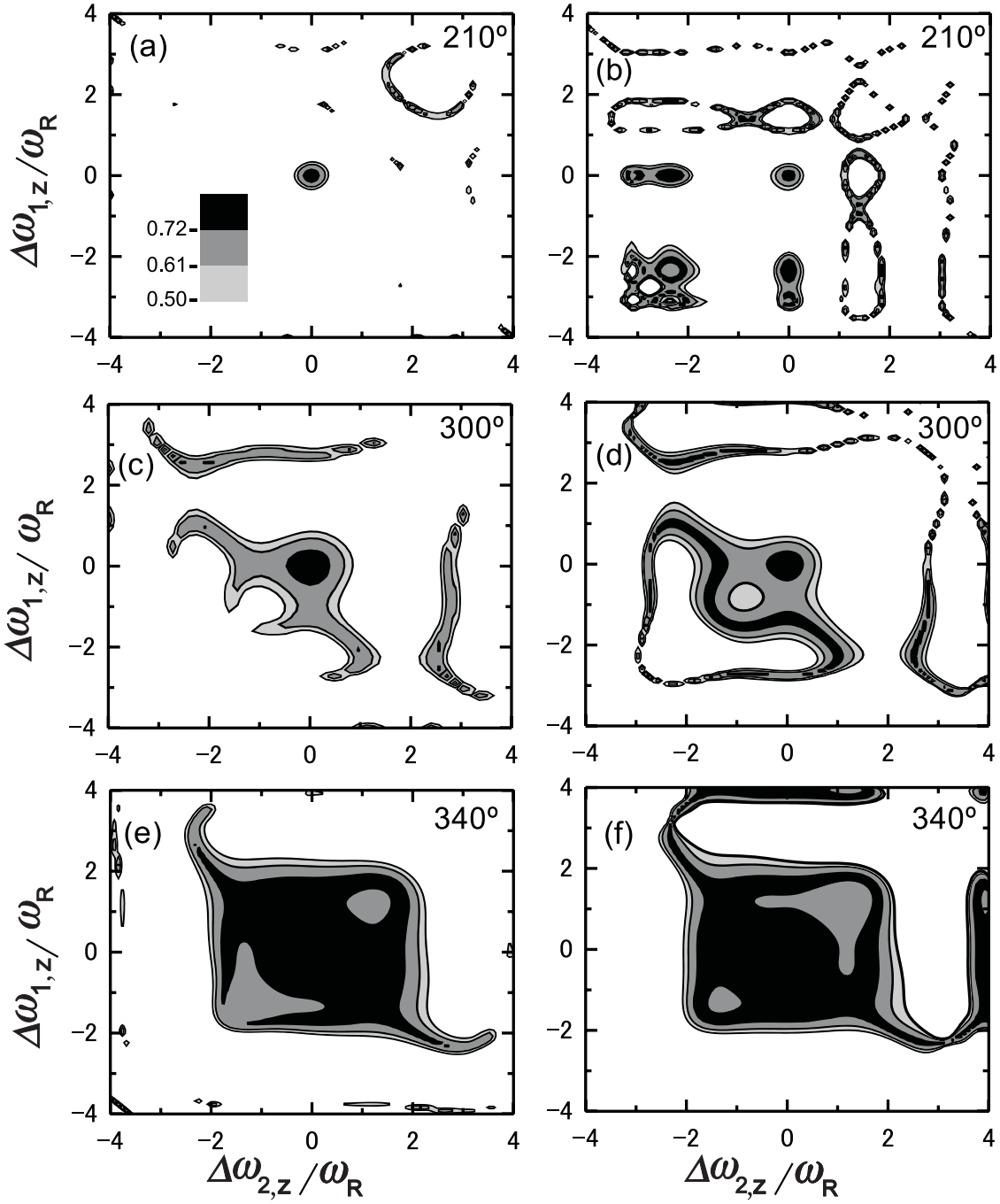

Figure 2.5: Contour plots of the maximum transferred magnetization $M_{\rm m}$ as a function of offsets obtained with the exact numerical computation (a, c, e) and the effective Hamiltonian in Eq.(2.12) (b,d,f) for the powder distribution. The maximum is shown for the SC^z5 sequence with $a = 210°$ (a,b), 300° (c,d), and 340° (e,f). Equation (2.16) was used for Figs. (b), (d), and (f). Contour lines indicate $M_{\rm m}/M_0$.

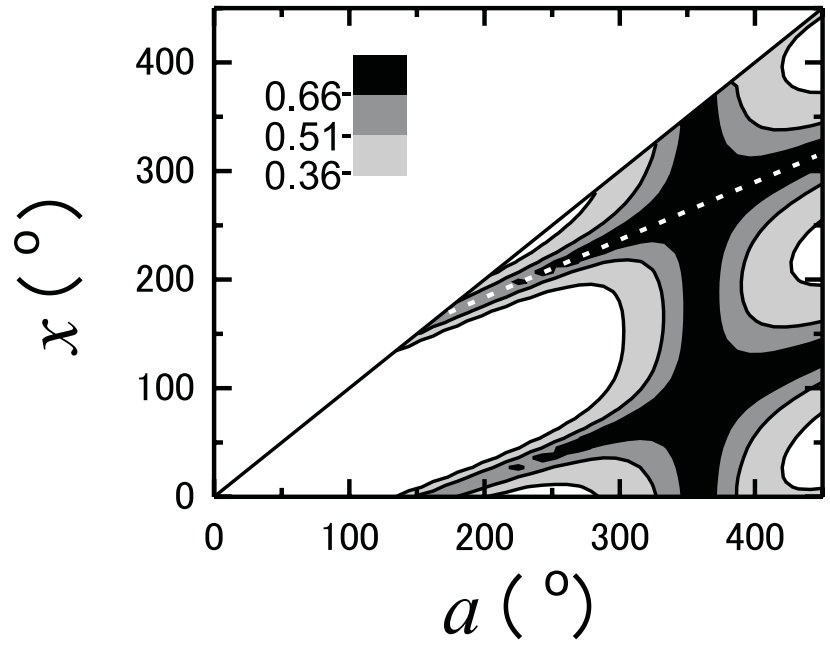

Figure 2.6: Maximum transferred magnetization with the SC5 sequence as a function of a and x for the C-element pulse, $(a-x)_0(a)_\pi(x)_0$. The magnetization was numerically calculated for a covalently bonded carbon spin pair at $\nu_{\rm R}$ =10 kHz in the powdered state. The contour plot gives the maximum transferred magnetization averaged over the offsets $(\Delta\omega_{1z}, \Delta\omega_{2z}) = (0.3, 0.3)\nu_{\rm R}$, $(0.15, 0.15)\nu_{\rm R}$ and $(0.15, -0.15)\nu_{\rm R}$. The white broken line corresponds to the C^z-condition, $x = a/2 + \pi/2$. Contour levels indicate the average magnetization normalized by M_0.

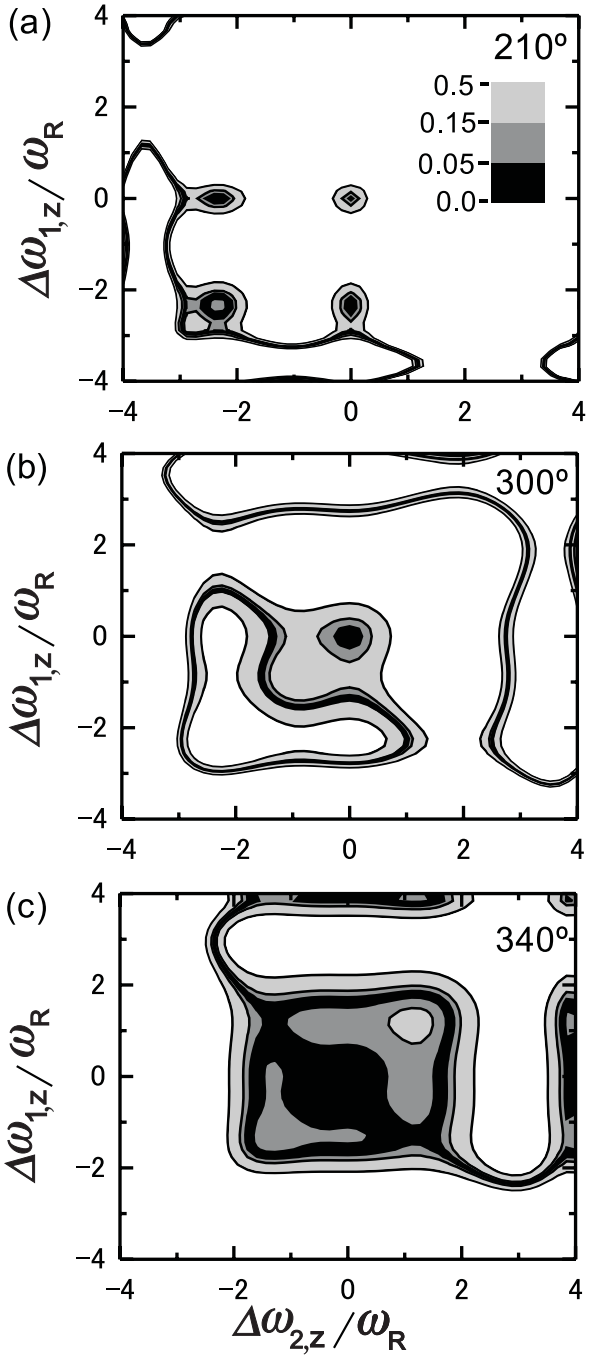

Figure 2.7: Contour plots of the spin rotation frequency relative to the dipolar coupling strength $|\omega_\sigma/\kappa_{\rm rf}b|$ as a function of offsets. The relative frequency $|\omega_\sigma/\kappa_{\rm rf}b|$ was calculated for the SC^z5 sequence at $a = 210^\circ$ (a), 300° (b), and 340° (c). The offset regions where $|\omega_\sigma/\kappa_{\rm rf}b| \leq 0.5$ are shaded as the indicator.

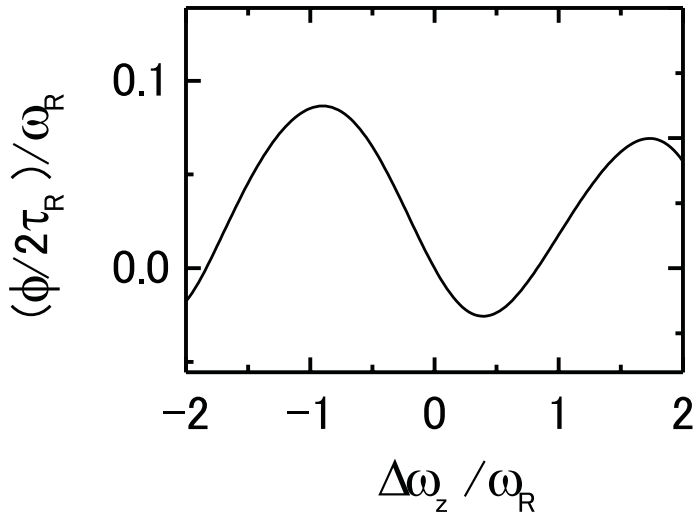

Figure 2.8: The z component of the residual spin rotational frequency as a function of the offset. The spin rotation was calculated for the modified C^z5 sequence with $a = 280°$ and $\Delta = 70°$ When ν_{R} =15 kHz, $\gamma B_1/2\pi$ is 58.3 kHz.

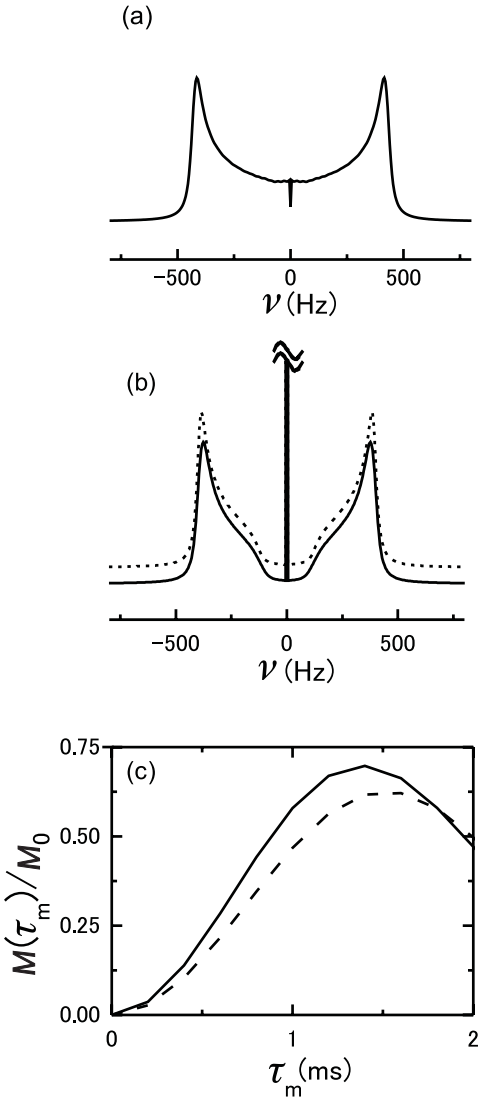

Figure 2.9: Dipolar powder spectra for the recoupled DQ dipolar interaction (a,b), and the transferred magnetization as a function of the mixing time calculated for $^{13}C^{\alpha}$–$^{13}C^{\beta}$ of alanine, (c). The spectra are shown for the SC^z5 sequence with $a = 360°$ (a) and 210° (b) at ν_R =10.0 kHz. The dipolar coupling constant is 2250 Hz. The orientations of the shielding tensors and the principal values for the C^{α} and C^{β} spins were taken from Ref. [48]. The spectrum shown with the broken line in (b) was calculated without the shielding anisotropies. The irradiation frequency for the recoupling sequence was set at the center of the two isotropic chemical shifts at $B_0 = 9.4$ T. An exponential line-broadening factor was 32 Hz. Spectra (a) and (b) have the same integral intensity. In (c), the transferred magnetization calculated with parameters used for (a) and (b) is shown with solid and broken lines, respectvely. The maxima for the solid and broken lines, are 95 % and 85 % of the theoretical maximum 0.73, respectively.

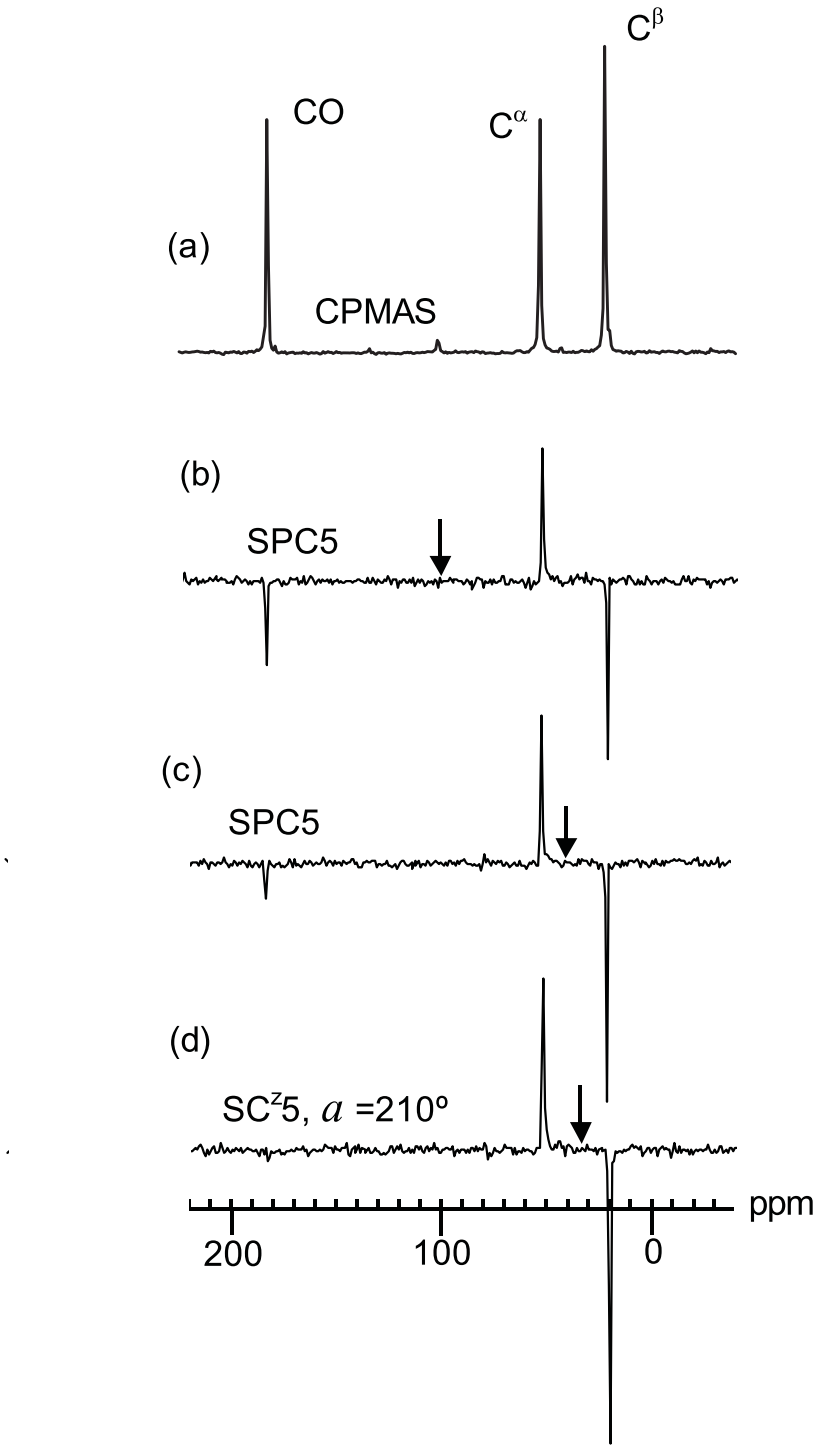

Figure 2.10: Spectra of uniformly ^{13}C, ^{15}N labeled L-alanine obtained with cross polarization (a) and the pulse sequence shown in Fig.2.1(b) (b–d) at ν_{R} =10 kHz and B_0 =9.4 T. The SC^z5 recoupling sequences having $a = 360°$ (b, c) and 210° (d) were employed with $\gamma B_1/2\pi$ =50.0 and 29.2 kHz, respectively, and a mixing time of 1.2 ms. The spectra in (b–d) are shown with the same gain for signal intensity. The mixing pulse was irradiated at the frequencies indicated with arrows, corresponding to 100, 40, and 35 ppm in (b), (c) and (d), respectively.

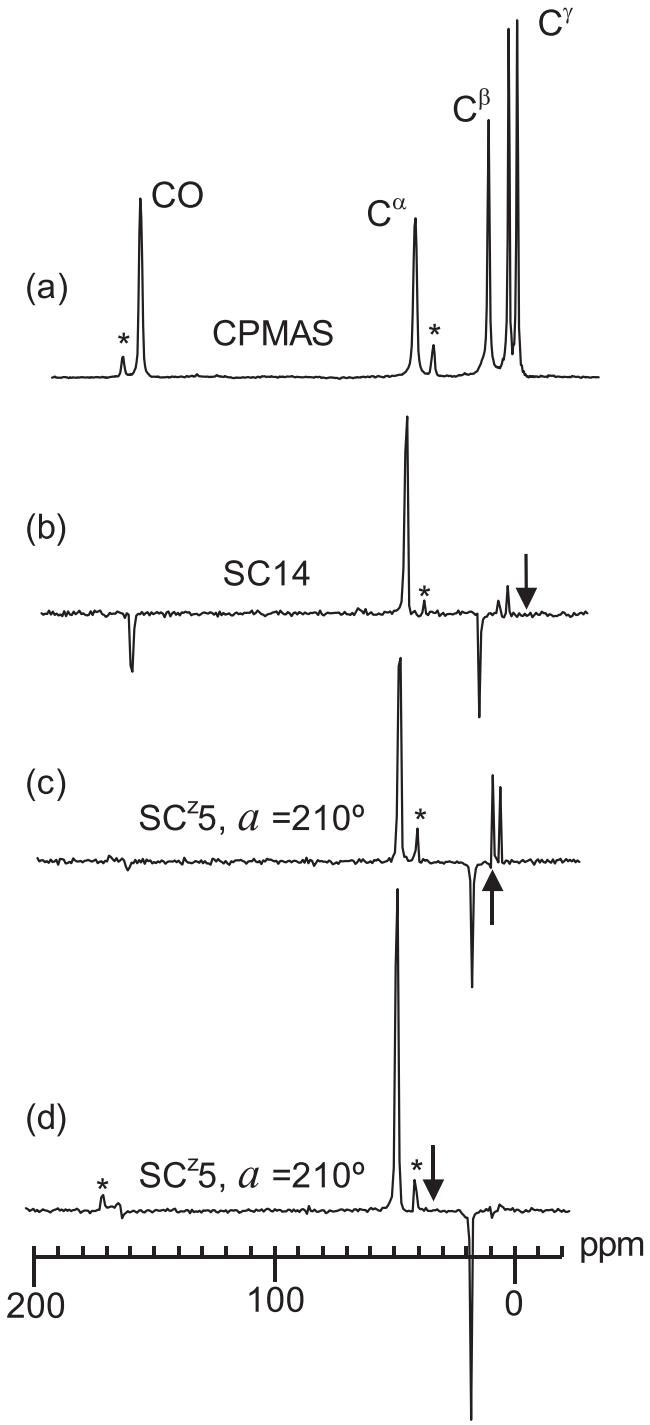

Figure 2.11: Spectra of uniformly ^{13}C, ^{15}N labeled L-valine obtained with cross polarization (a) and the pulse sequence shown in Fig.2.1(b) (b–d) at ν_{R} =15 kHz and B_0 =11.8 T. The SC14 sequence (b) and the SC^z5 sequence with $a = 210°$ (c,d) were used in the recoupling period. The mixing time was 0.80, 1.60 and 1.06 ms for (b), (c) and (d), respectively. The recoupling field amplitude was 52.5 kHz (b) and 43.8 kHz (c,d). The spectra (b–d) are shown with the same gain for signal intensity. Asterisks indicate spinning sidebands. The mixing pulse was irradiated at the frequencies indicated with arrows, corresponding to 0, 12, and 38 ppm in (b), (c) and (d), respectively.

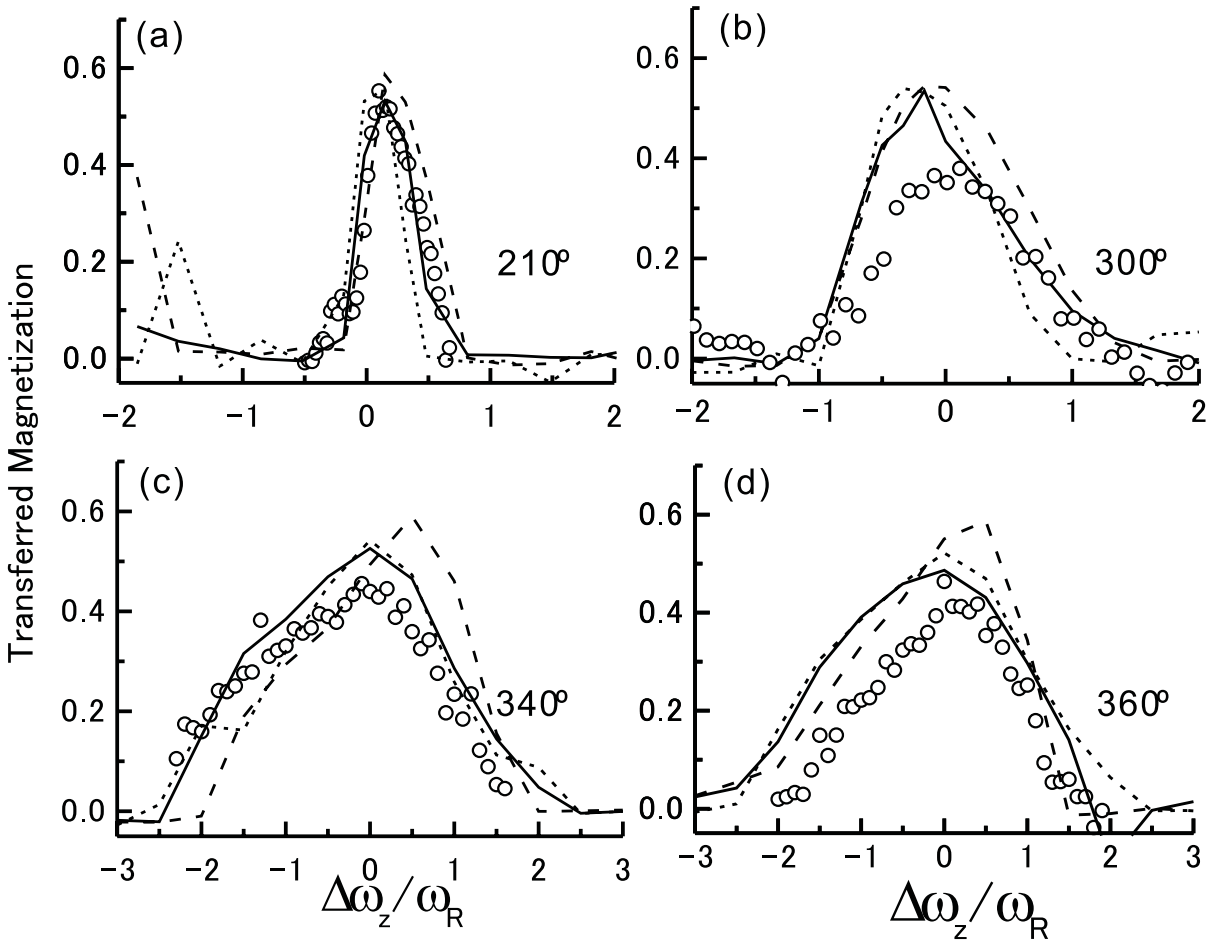

Figure 2.12: The experimental (circles) and calculated (lines) magnetization transferred with SC^z5 at $a = 210°$ (a), 300° (b), 340° (c), and 360° (d) as a function of offset for fully ^{13}C labeled alanine at ν_R =10 kHz. The RF amplitude was 29.2 (a), 41.7 (b) , 47.2 (c), and 50.0 kHz (d). The numerical simulations were performed for the three-spin system $^{13}C^{\alpha}$–$^{13}C^{\beta}$–^{13}CO in alanine. The calculated magnetization at +5% and -5% rf inhomogeneity are also shown in each figure by broken and dotted lines, respectively. The transferred magnetization was measured from the integral intensity of the C^{β} signal. The mixing time was 1.2 ms.

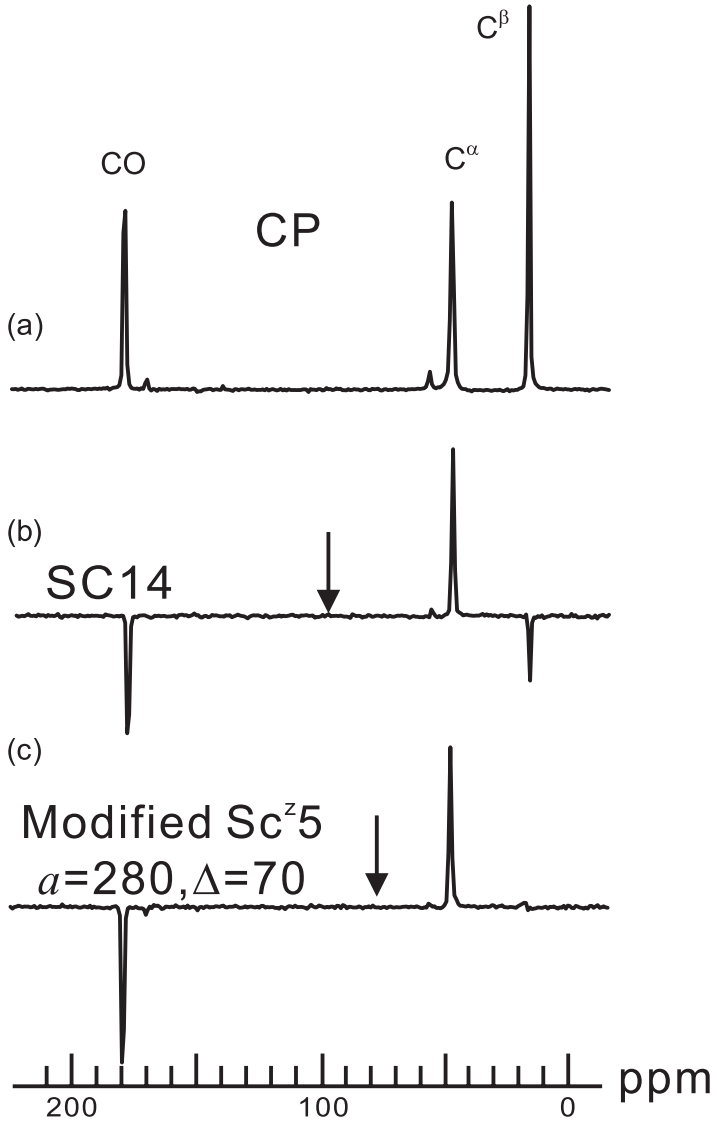

Figure 2.13: Spectra of uniformly ^{13}C, ^{15}N labeled L-alanine obtained with cross polarization (a) and the pulse sequence shown in Fig.2.1(b) (b)(c) at ν_{R} =15 kHz and B_0 =9.4 T. The SC14 sequence (b) and the modified SC^z5 sequence with $a = 280°, \Delta = 70°$ (c) were used in the recoupling period. The mixing time was 1.06 and 1.60 ms for (b) and (c), respectively. The rf field amplitude was 52.5 kHz (b) and 58.3 kHz (c). The spectra in (b) and (c) are shown with the same gain for signal intensity.

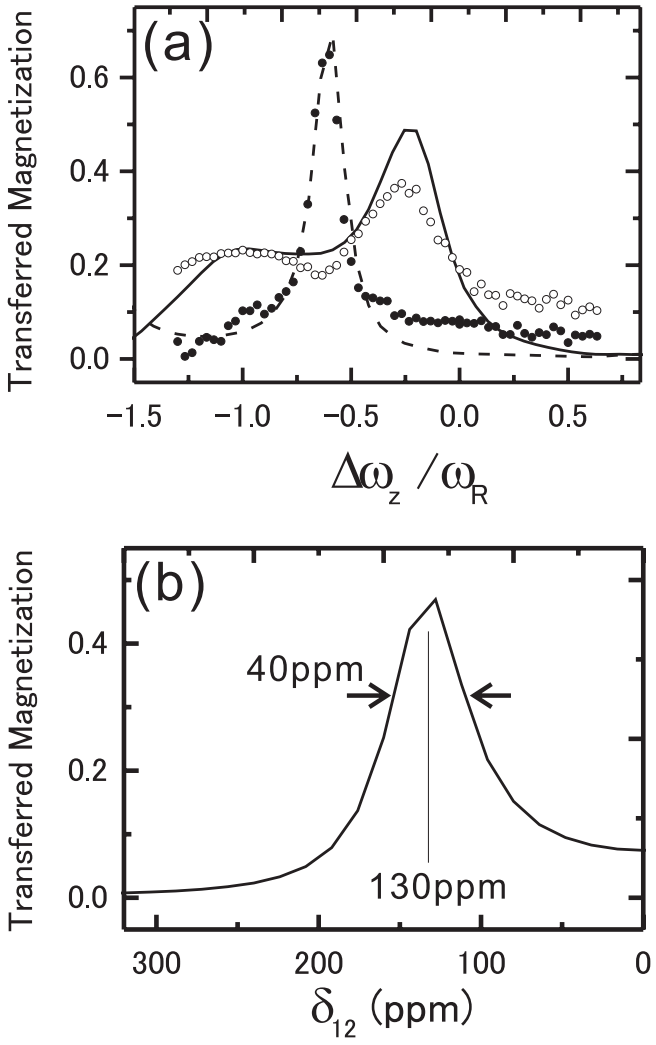

Figure 2.14: (a) The experimental (circles) and calculated (lines) magnetization transferred with the modified SC^z5 at $a = 280°, \Delta = 70°$ as a function of offset (a), and the chemical shift difference (b). The transferred magnetization indicated by filled and open circles were measured from the integral intensity of the C^β and ^{13}CO signals of fully ^{13}C labeled alanine at ν_{R} =15 kHz. The mixing time was 1.6 ms. The RF amplitude was 58.3 kHz. The numerical simulations indicated by dashed and solid lines were performed with a two-spin system with $^{13}\mathrm{C}^\alpha$–$^{13}\mathrm{C}^\beta$ and $^{13}\mathrm{C}^\alpha$–^{13}CO, respectively.

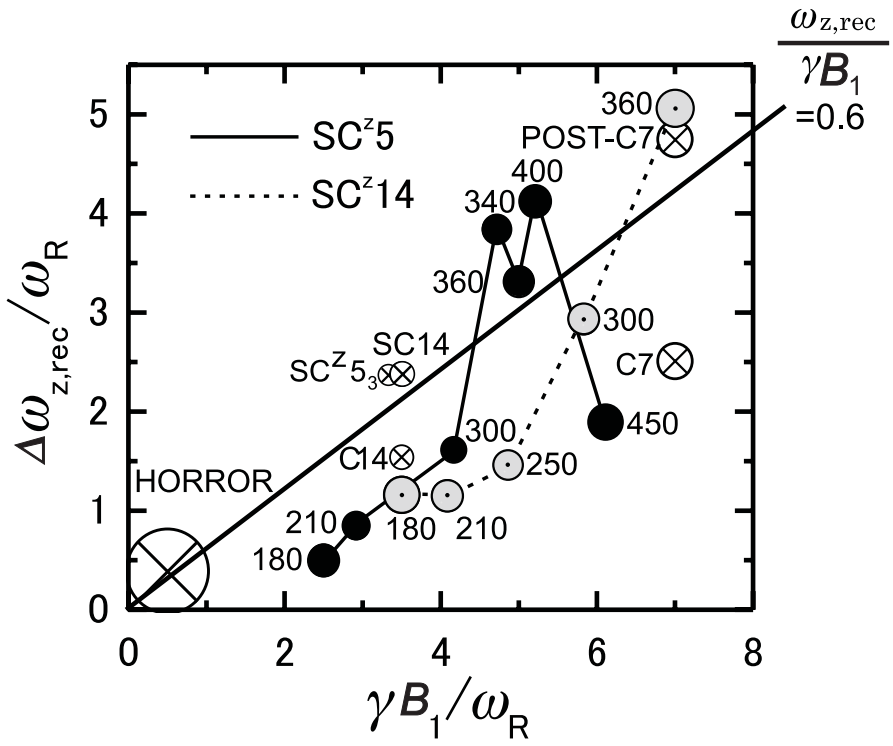

Figure 2.15: Effective bandwidth, $\Delta\omega_{z,\mathrm{rec}}/\omega_{\mathrm{R}}$, as a function of the recoupling field amplitude , $\gamma B_1/\omega_{\mathrm{R}}$, calculated for DQ dipolar recoupling sequences. The solid and broken lines connect the points obtained for SC^z5 and SC^z14, respectively. The C-element pulse in SC14 and $\mathrm{C}14^4_5$ is $(2\pi)_0$ and that in $\mathrm{SC}^z5_3 = \mathrm{C}5^1_3\overline{\mathrm{C}5^1_3}$ is $(\pi/2)_0(2\pi)_\pi(3\pi/2)_0$. The effective bandwidths were computed for a covalently bonded ^{13}C pair with the same resonance frequency. The effective recoupling bandwidth $\Delta\omega_{z,\mathrm{rec}}$ is defined by the offset range where the maximum transferred magnetization M_{m} is larger than a half of M_{m} on resonance. Effective bandwidths were calculated at $\nu_{\mathrm{R}} = 10$ kHz, but they were almost the same at 20 kHz in the scale normalized by ω_{R}. The radii of the circles are proportional to the scaling factors.

CHAPTER 3

Recoupling of the ^{1}H–^{1}H DQ-Dipolar Interactions

3.1 Introduction

The molecular conformation can be probed with the anisotropic spin-spin interactions in solids. The through-space dipolar interaction between nuclear spins can be used to estimate the inter-nuclear distance. In the fully ^{13}C-labeled organic solids, one ^{13}C spin generally receives a dominant dipolar effect from a covalently bonded neighbor ^{13}C spin in the coupled ^{13}C-spin network. This large dipolar coupling to the covalently bonded partner often covers the effect from distant ^{13}C spins which is useful to the molecular structure determination. Also, ^{13}C spins in two distant molecular segment or domain do not become spatially very close each other even with a molecular folding, while it occurs for ^{1}H spins. Thus, the molecular conformation can be probed by determining shorter inter-nuclear distances if one focus on the ^{1}H dipolar couplings rather than that of ^{13}C. In this sense, inter-proton (^{1}H–^{1}H) distance information is more powerful to determine the molecular conformation. Nevertheless, the poor resolution for the ^{1}H NMR spectrum in solids hampers the direct observation of the ^{1}H signals to estimate the ^{1}H–^{1}H distances.

The diffusive property of ^{1}H magnetization in the dense ^{1}H dipolar coupling network (spin diffusion) has been used to probe the structural and dynamical heterogeneity of polymers and polymer blends, providing relatively large molecular feature such as a distance across phases or domains of polymers [1, 2]. The methods for the measurement of long ^{1}H–^{1}H distance relying on the ^{1}H spin diffusion often suffers from the accuracy because the observed propagation of the magnetization contains both contributions from direct and relayed magnetization transfer. Spiess *et al.* used the two-pulse excitation and re-conversion technique that favorably recouples a strong ^{1}H DQ dipolar interaction to determine short

^{1}H–^{1}H distances [3]. Other techniques used the SQ and DQ-spinning side bands of the ^{1}H dipolar coupling [4, 5] or ^{1}H–^{1}H DQ/SQ spectra [6, 7] to estimate ^{1}H–^{1}H distances with an assumption of an isolated ^{1}H–^{1}H pair under very fast MAS conditions ($\nu_{\rm R} = 30$ kHz).

Recently, Levitt *et al.* has developed a general symmetry principle for the RF pulse irradiation to assist the recoupling or decoupling of the spin interaction(s) under MAS conditions [8, 9, 10, 11]. Two types of general sequences $CN^{\nu}_{\rm n}$ and $RN^{\nu}_{\rm n}$ are known. The homonuclear DQ-dipolar interaction can selectively be recoupled with the CN sequence of the symmetry such as $C7^1_2$ (POST-C7) [12], $C5^1_2$ (SPC5) [13], $C14^5_4$ (SC14) [14] etc, and has been applied to the signal assignments [15] and internucelar distance measurement for ^{13}C spin systems [16]. In the magnetization transfer experiment with the DQ mixing, the cross peak signals display positive and negative intensities when, respectively, odd and even number of spins intermediate the transfer process between the source and destination spins, i.e. in the ^{13}C spin system, a negative cross peak appears for a neighbor carbon and a positive one for the next neighbor carbon and so on [17]. This feature aided the signal assignment for the ^{13}C-chemical shift spectrum [18, 15].

We show that ^{1}H–^{1}H distances can be accurately determined on the basis of the time dependence of the ^{1}H–^{1}H magnetization transfer under the ^{1}H DQ-dipolar interaction recoupled with POST-C7. Because the DQ-process conveys the magnetization to a directly dipolar coupled ^{1}H spin in negative intensity, our method distinguishes the direct transfer (with zero intermediating proton) with the relayed one. Our method extracts the ^{1}H–^{1}H distance information via the high-resolution ^{13}C-chemical shift spectrum.

3.2 Theory

We employ POST-C7 to recouple the ^{1}H DQ-dipolar interactions in the ^{1}H spin system. POST-C7 is consisted of seven element pulses ($N = 7$) with an rf phase rotation about the laboratory frame z axis that span two rotor revolutions ($n = 2$) as shown in Fig.3.1. We first show the main effective Hamiltonian under POST-C7 with average Hamiltonian theory (AHT) and discuss about different factors that determine the effective bandwidth of the magnetization transfer in ^{1}H and ^{13}C spin systems. We analyse the effect of the residual spin interactions other than the ^{1}H DQ-dipolar term during the recoupling time, and compare the situation in ^{1}H and ^{13}C spin systems.

3.2.1 Interactions under POST-C7

Double-quantum dipolar term

The high-filed truncated Hamiltonian in the presence of the homonuclear (II) as well as the heteronuclear (IS) dipolar interactions and rf-field irradiation of the CN sequence is written under magic-angle sample spinning (MAS) as

$$\mathcal{H} = \mathcal{H}^{II}_{lm\lambda 0}(t) + \mathcal{H}^{IS}_{lm\lambda 0}(t) + \mathcal{H}^{\mathrm{RF}}(t) \tag{3.1}$$

$$\mathcal{H}^{II}_{lm\lambda 0}(t) = \sum_{m=\pm 1,\pm 2} \omega^{II}_{lm} \exp\left(im\omega_{\mathrm{R}}t\right)\sqrt{6}\, T_{20}, \tag{3.2}$$

$$\mathcal{H}^{IS}_{lm\lambda 0}(t) = \sum_{m=\pm 1,\pm 2} \omega^{IS}_{lm} \exp\left(im\omega_{\mathrm{R}}t\right) T_{10} S_z, \tag{3.3}$$

with

$$\omega^{\Lambda}_{2\pm 1}(t) = b_{\Lambda}\sqrt{\frac{3}{8}}\sin(2\beta_{\mathrm{PR}})\exp\left(\pm i\gamma_{\mathrm{PR}}\right) d^{(2)}_{\pm 10}(\theta_{\mathrm{m}})\exp\left(\pm i\alpha_{\mathrm{RL}}\right), \tag{3.4}$$

$$\omega^{\Lambda}_{2\pm 2}(t) = b_{\Lambda}\sqrt{\frac{3}{8}}\sin^2(\beta_{\mathrm{PR}})\exp\left(\pm 2i\gamma_{\mathrm{PR}}\right) d^{(2)}_{\pm 20}(\theta_{\mathrm{m}})\exp\left(\pm 2i\alpha_{\mathrm{RL}}\right) \tag{3.5}$$

$$b_{II} = -\frac{\mu_0}{4\pi}\frac{\gamma_I^2}{r_{II}^3}\hbar, \tag{3.6}$$

$$b_{IS} = -\frac{\mu_0}{4\pi}\frac{\gamma_I\gamma_S}{r_{IS}^3}\hbar. \tag{3.7}$$

in which $\Lambda = II$ or IS [19]. In Eq.(3.4) and (3.5), the dipolar couplings in the principal axis system (PAS), $\rho_{20,\Lambda}^{\mathrm{PAS}} = \sqrt{3/8}b_\Lambda$, are expressed in the laboratory frame by using the rotational property of the spherical tensor operators

$$\mathbf{R}(\alpha\beta\gamma) \equiv R_z(-\alpha)R_z(-\beta)R_z(-\gamma)\rho_{\lambda 0}R_z(\alpha)R_z(\beta)R_z(\gamma) \tag{3.8}$$

$$= \sum_\mu d_{\mu 0}(-\beta)e^{i\mu\gamma}\rho_{\lambda\mu}. \tag{3.9}$$

The euler angles β_{PR} and γ_{PR} define the relative orientation of the dipolar PAS to the rotor-fixed frame, θ_{m} is the magic angle, γ_i is the magnetogyric ratio of spin i and r_{ij} is the internuclear distance between spins i and j. Each term in the Hamiltonian has its own rotation property in real and spin space, characterized by the ranks l, λ and indices m, μ in the respective spaces. The irreducible tensor operators, $T_{10} = \sqrt{2}I_z$ and $T_{20} = \frac{1}{\sqrt{6}}(3I_{1z}I_{2z}) - \mathbf{I}_1\mathbf{I}_2$ conveniently describe the rotational properties of the spin Hamiltonians. For the pulse sequence shown in Fig.3.1, the sample spinner rotates n times with N element pulses, thus for a p-th element pulse, the rotor phase at time point $\tau_p = \tau_0 + p\tau_{\mathrm{c}}$, ($p = 0$ to $N-1$) is $\phi_{\mathrm{rot}}^{(p)} = \frac{2\pi n}{N}p$. The periodic symmetry of the laboratory frame spin interaction terms may be expressed with the rotor phase $\phi_{\mathrm{rot}} = 2\pi$ as

$$\mathcal{H}_{lm\lambda 0}^{\Lambda}(\tau_p) = \mathcal{H}_{lm\lambda 0}^{\Lambda}(\tau_0)\exp\left\{i\phi_{\mathrm{rot}}^{(p)}\right\}. \tag{3.10}$$

Note that in the high-field approximation, the internal Hamiltonian contains only elements with $\mu = 0$ (secular terms). On the other hand, the terms with $\mu \neq 0$ are generated by the effect of the applied rf field as below.

Average Hamiltonian theory requires a tranformation of the spin interaction terms into the interaction frame of the rf field, where the evolution caused by the rf field is removed.

In this frame denoted by tilde, the Hamiltonian under the rf field irradiated at the I-spin is written with the rf phase for the p-th element pulse $\phi_{\rm rf}^{(p)} = \frac{2\pi\nu}{N}p$ as

$$\tilde{\mathcal{H}}^{II}_{lm\lambda\mu}(\tau_p) = \sum_{m,\mu} \mathcal{F}^{II}_{lm\lambda\mu}(\tau_p)\ \sqrt{6}\, T_{2\mu} \exp\left\{i\left(m\omega_{\rm R}\tau_p - \mu\gamma_{\rm RF}\right)\right\}, \tag{3.11}$$

$$\tilde{\mathcal{H}}^{IS}_{lm\lambda\mu}(\tau_p) = \sum_{m,\mu} \mathcal{F}^{IS}_{lm\lambda\mu}(\tau_p)\ T_{1\mu}S_z \exp\left\{i\left(m\omega_{\rm R}\tau_p - \mu\gamma_{\rm RF}\right)\right\}, \tag{3.12}$$

with

$$\mathcal{F}^{II}_{lm\lambda\mu}(\tau_p) = \omega^{II}_{lm}\ d^{(2)}_{\mu 0}\left(\beta_{\rm RF}\right) \tag{3.13}$$

$$\mathcal{F}^{IS}_{lm\lambda\mu}(\tau_p) = \omega^{IS}_{lm}\ d^{(1)}_{\mu 0}\left(\beta_{\rm RF}\right). \tag{3.14}$$

Each term $\mathcal{H}^{\Lambda}(t)$ depends on the mechanical rotation of the rotor and spin rotation by the CN sequence. The rotation of the spin Hamiltonian is described with the flip angle $\beta_{\rm RF}$ and the Wigner rotation functions of first $d^{(1)}_{\mu 0}$ and second rank $d^{(2)}_{\mu 0}$. Now, the periodic symmetry of the Hamiltonian terms depends also on the pulse sequence as

$$\tilde{\mathcal{H}}^{\Lambda}_{lm\lambda\mu}(\tau_p) = \tilde{\mathcal{H}}^{\Lambda}_{lm\lambda\mu}(\tau_0) \exp\left\{i\frac{2\pi p}{N}\left(mn - \mu\nu\right)\right\}. \tag{3.15}$$

One may analyse the CN sequence using the Magnus expansion of the effective Hamiltonian. The effective Hamiltonian for p-th element pulse that spans the time period $\tau_{p-1} < t < \tau_p$ is written as

$$\overline{\mathcal{H}}^{\Lambda}_{(p)lm\lambda\mu} = \overline{\mathcal{H}}^{\Lambda(1)}_{(p)lm\lambda\mu} + \overline{\mathcal{H}}^{\Lambda(2)}_{(p)lm\lambda\mu} + \overline{\mathcal{H}}^{\Lambda(3)}_{(p)lm\lambda\mu} + \cdots, (p: 0\ \text{ to }\ N-1) \tag{3.16}$$

where the first-order term is given by

$$\overline{\mathcal{H}}^{\Lambda(1)}_{(p)lm\lambda\mu} = \tau_{\rm c}^{-1} \int_{\tau_{\rm p}}^{\tau_{\rm p+1}} \tilde{\mathcal{H}}^{\Lambda}_{lm\lambda\mu}(t)dt. \tag{3.17}$$

The effective Hamiltonian for the entire sequence is obtained by coupling N elemental Hamiltonians $\overline{\mathcal{H}}^{\Lambda}_{(p)lm\lambda\mu}$ as is written as

$$\overline{\mathcal{H}}^{\Lambda(1)}_{lm\lambda\mu}(N\tau_{\rm c}) = \frac{1}{N\tau_{\rm c}} \sum_{p=0}^{N-1} \overline{\mathcal{H}}^{\Lambda}_{(p)lm\lambda\mu}\, \tau_{\rm c} \tag{3.18}$$

for the first order term. For $\overline{\mathcal{H}}^{\Lambda(1)}_{lm\lambda\mu}$, the selection rule,

$$\overline{\mathcal{H}}^{\Lambda(1)}_{lm\lambda\mu} = 0 \quad \text{if } mn - \mu\nu \neq NZ, \tag{3.19}$$

is derived where Z is any integer. For POST-C7 with $N = 7, n = 2$, and $\nu = 1$, the effective Hamiltonian in Eq.(3.17) of the lowest order is written as

$$\begin{aligned} \mathcal{H} &\approx \overline{\mathcal{H}}^{II(1)}_{2122}(N\tau_{\rm c}) + \overline{\mathcal{H}}^{II(1)}_{2-12-2}(N\tau_{\rm c}) \\ &= \omega^{+1}_{\rm DQ}\, T_{22} + \omega^{-1}_{\rm DQ}\, T_{2-2}. \end{aligned} \tag{3.20}$$

Above, the scaled dipolar couplings can be written in a product of the dipolar coupling b defined in Eq.(3.6) and the scaling factor $|\kappa^{+1}| = |\kappa^{-1}| \approx 0.232$ as $\omega^{+m}_{\rm DQ} = \omega^{-m*}_{\rm DQ} = \kappa^{+m} b$ [12]. The scaling factor is defined by

$$\kappa^{\pm m} = \tau_{\rm c}^{-1} \int_{\tau_p}^{\tau_{p+1}} \mathcal{F}_{2\pm m2\pm 2}(t) e^{im\omega_{\rm R} t} dt. \tag{3.21}$$

In Eq.(3.21), each term with $\mu = 2$ and $= -2$ is associated with only one spatial rotatoinal component with $m = 1$ and $= -1$, respectively. Thus only one of two Euler angles $\beta_{\rm PR}$ and $\gamma_{\rm PR}$ that differ by the crystallite orientation affects the amplitude of the effective nutation field of the recoupled DQ-dipolar interaction. On the other hand, the phase of the DQ-nutation field depends on both angles $\beta_{\rm PR}$ and $\gamma_{\rm PR}$. This means that the DQ-dipolar interaction can be recoupled with same amplitude for crystallite components with the same value of $\beta_{\rm PR}$ but different $\gamma_{\rm PR}$ values, and leads to large overall recoupling.

This feature so called γ-encoding is realized so far only with the DQ-dipolar part, and provides larger recoupling efficiency for powder samples than that for the zero-quantum (ZQ) part of the dipolar interaction.

The crystallite orientation dependence of the recoupled DQ-dipolar interaction can be seen from the dipolar powder spectrum shown in Fig.3.2. The time evolution under POST-C7 of the total Zeeman magnetization, $I_{1z} + I_{2z}$, were numerically calculated for powder crystallite orientations. The Fourier transform of the time domain data revealed the powder pattern of the recoupled DQ-dipolar interaction. The pattern shows two strong peaks at $\nu_{\mathrm{D}} = \pm 1.83$ kHz. This value is consistent with the dipolar coupling of about 8 kHz for a ^{1}H–^{1}H pair separated by ≈ 220 pm assumed in the numerical calculation that is scaled by $|\kappa^{-1}| \approx 0.232$ for POST-C7. The strongest peaks seen at the edges of the pattern indicate that the largest DQ-dipolar interaction is recoupled for largest population of the powder components.

Because the separation of the doublet can easily be identified at two strong peak even in noisy spectrum, the measurement of the powder pattern provides a convenient way of elucidating ^{1}H–^{1}H distance in powder samples. The favorable pattern in the powder spectrum is due to the γ-encoding property of POST-C7. With the methods that recouple the dipolar interaction γ dependently, including DRAMA, larger intensities are observed around the center of the powder pattern [23].

Tolerance to the resonance offset

Under the effect of the recoupled DQ-dipolar interaction, the nuclear magnetization can be transferred between spins. This is one of the fundamental techniques for the spin correlation and molecular structure analysis. We inspected how the amount of the transferred magnetization depends on the resonance offsets and the DQ-dipolar coupling strength. The dipolar coupling strength depends on the nuclear spin spieces and the internuclear dis-

tances concerned. The series of recoupling sequences involving POST-C7 employed in the ^{1}H DQ-dipolar recoupling experiment here could generally be applied to different nuclear spin systems, and factors that determine the offset dependence of the effective bandwidth of the magnetization transfer may depend on each system considered.

Large external applied field B_0 favorable for the resolution and sensitivity of the spectra should be available also for the solid-state facilities in the near furture. Under the static field of the strength $B_0 \sim 20$ T, the chemical shift of the ^{1}H spin ranges over 13 kHz, in which the recoupling pulse sequences are desired to be effective and stable. In the previous chapter, we have derived the offset dependence of the magnetization transfer under the effect of the DQ-dipolar interactions recoupled with CN sequences including POST-C7 in an isolated two spin system. The element pulses used in the CN sequences are cyclic on resonance, and does not left any overall spin rotation provided that the rf field is ideally homogeneous. We have ascribed the reduced magnetization transfer at offsets to the residual rotation of spins termed by $\mathcal{H}_{\rm A}$ in the total Hamiltonian that describes the system. The residual spin rotation is almost only about the z axis after the z rotational averaging procedure in Eq.(3.18) of the CN sequece, thus for a coupled spin 1 and 2:

$$\begin{aligned}\mathcal{H}_{\rm A}(N\tau_{\rm c}) &\approx \omega_1^{\rm eff} n_{1z} I_{1z} + \omega_2^{\rm eff} n_{2z} I_{2z} \\ &= \frac{\omega_\delta}{2}\left(I_{1z} - I_{2z}\right) + \frac{\omega_\sigma}{2}\left(I_{1z} + I_{2z}\right), \end{aligned} \tag{3.22}$$

with $\omega_\sigma = \omega_1^{\rm eff} n_{1z} I_{1z} + \omega_2^{\rm eff} n_{2z} I_{2z}$ and $\omega_\delta = \omega_1^{\rm eff} n_{1z} I_{1z} - \omega_2^{\rm eff} n_{2z} I_{2z}$, in which $\omega_j^{\rm eff}$ is an effective spin rotation frequency of spin j. The second term in Eq.(3.22) does not commute with the DQ-dipolar terms and intervenes the magnetization transfer under the effect of the DQ term. The magnetization that transfers between the spin 1 and 2 at offset $\Delta\omega_z$ has been

derived as

$$M_{\mathrm{m}}(\Delta\omega_z) = \sin^2(\arctan(r^{-1})) \approx 1 - r^2 + \frac{11}{12}r^4 - \frac{5}{12}r^6 + \cdots , \tag{3.23}$$

in which r is a function of the offset in the form of a ratio of the residual spin rotation to the DQ-dipolar coupling strength: $r(\Delta\omega_z) = \omega_\sigma/\omega_{DQ}$.

Equation (3.23) above shows $M_{\mathrm{m}}(\Delta\omega_z)$ is larger than $0.8M_{\mathrm{m}}(0)$ while $r < 0.5$. In another words, the effective magnetization transfer occurs in the frequency range in which the recoupled dipolar coupling strength is 2 times larger or more than the residual spin rotation frequency, i.e. $\omega_{\mathrm{DQ}} > 2\omega_\sigma$. Figure 3.3(a) explains schematically the relation of the quantities $\omega_{\mathrm{DQ}}(\Delta\omega_z)$ and $\omega_\sigma(\Delta\omega_z)$. In 3.3(a), both $\omega_{\mathrm{DQ}}(\Delta\omega_z)$ and $\omega_\sigma(\Delta\omega_z)$ are normalized to a value $\omega_{\mathrm{DQ}}(0)$, thus different dipolar coupling strengths because of the difference in the spin spieces and/or the internuclear distance involved in the system concerned are displayed as the different slopes of lines plotting $2\omega_\sigma(\Delta\omega_z)$. Strong dipolar coupling with a ^{1}H–^{1}H pair for instance thus is represented by a small slope of the $2\omega_\sigma(\Delta\omega_z)$ line. Note that the different slopes has emanated from the normalization procedure that is just for the convenience for the drawing. The rotational response of the spin to the applied B_1 field depends neither on the nuclear spieces nor the internuclear distances. The offset dependence of the magnetization transfer is here characterized by the relative arrangement of two lines plotting the dipolar coupling strength (solid line) that depends on the spin system, and that plotting the residual spin rotation (dotted and dashed lines) that depend on the pulse sequences. The offset frequency $\Delta\omega_z$ at which the solid and broken lines cross defines the bound of the effective magnetization transfer bandwidth that gives $M_m(\Delta\omega_z) > 0.8M_m(0)$.

The relative importance of the factors $\omega_\sigma\Delta\omega_z$ and $\omega_{\mathrm{DQ}}\Delta\omega_z$ on the determination

of the effective bandwidth may be able to discuss as follows. When on one hand, $\omega_\sigma/\omega_{\mathrm{DQ}}(0)$ exceed 0.5, with an increasing $\Delta\omega_z$, before $\omega_{\mathrm{DQ}}/\omega_{\mathrm{DQ}}(0)$ falls below 0.5, the bound of the effective bandwidth (the intersection of the solid and broken lines) occurs at the offset where ω_{DQ} still has an amplitude > 0.5. In this case, it could be said that the effective bandwidth is mainly determined by the increase of the residual spin rotation. Because the spin rotation is characterized by the pulse sequence, the supercycling techniques of the mixing sequence that is designed to suppress the spin rotation at offset may improve the effective bandwidth. On the other hand, in the case where $\omega_{\mathrm{DQ}}/\omega_{\mathrm{DQ}}(0)$ falls below 0.5 before $\omega_\sigma/\omega_{\mathrm{DQ}}(0)$ exceeds 0.5, the effective bandwidth can be said mainly determined by the decay of the recoupled DQ-dipolar coupling strength at offset. In this case, the modification of the pulse sequence does not change the bandwidth.

Contour plots shown in Fig.3.4 show how the quantities $\omega_{\mathrm{DQ}}/\omega_{\mathrm{DQ}}(0)$ and $\omega_\sigma/\omega_{\mathrm{DQ}}(0)$ depend on the offsets of two spins $\Delta\omega_{1z}$ and $\Delta\omega_{2z}$. Figures 3.3(b)(e), and (c)(f) show ω_σ for ^{13}C- and ^{1}H spin pair systems, respectively. Quantities shown in Figs.3.3(a)(b)(c) and (d)(e)(f) were calculated assuming POST-C7 sequence applied at the sample spinning frequency $\nu_{\mathrm{R}} = 13$ kHz, and SPC5 sequence applied at $\nu_{\mathrm{R}} = 10$ kHz, respectively. Comparing Figs.3.3(a-c) with (d-f), one can see that the offset dependence of $\omega_{\mathrm{DQ}}/\omega_{\mathrm{DQ}}(0)$ and $\omega_\sigma/\omega_{\mathrm{DQ}}(0)$ in the unit of γB_1 are similar under the two recoupling sequences in spite of the different irradiation symmetry and the sample spinning conditions. Comparison of Figs.3.3(a) with (b), and (d) with (e) shows that the offset $\Delta\omega_z^\sigma$ at which the normalized residual spin rotation exceeds 0.5 is much smaller than that at which the normalized DQ-dipolar coupling strength falls below 0.5, $\Delta\omega_z^{\mathrm{DQ}}$ for a for a spin pair coupled by a relatively small dipolar interaction. On the other hand, for a spin pair coupled with

strong dipolar interaction, $\Delta\omega_z^{\sigma}$ is similar or larger than $\Delta\omega_z^{\mathrm{DQ}}$. These observations suggest that the effective bandwidth of the magnetization transfer under the effect of the recoupled DQ-dipolar interaction is mainly determined by the residual spin rotation in the weak coupling regime, while it is mainly limited by the decay of the DQ-dipolar coupling strength in the strong coupling regime.

The effective bandwidth calculated with Eq.(3.23) on the basis of the average Hamiltonian theory agrees well with that calculated with an exact numerical simulations as shown in Figs.3.5(c) and (d). The calculated area of the highest effeciency (black region) covers the offset range $\Delta\omega_z = \pm 20$ kHz, and is obviously broad enough for the uniform recoupling over the chemical shift range of the ^{1}H spins.

Higher MAS rate is also favorable to the resolution and sensitivity of the spectra as a consequence of narrow lines. The rotor synchronization of the pulses required for the CN recoupling sequence accordingly increases the mixing field amplitude needed. The amplitude needed for the POST-C7 under $\nu_{\mathrm{R}} = 20$ kHz is $\nu_{\mathrm{m}} = 140$ kHz, which is often an intolerable load on a normal probe. The required amplitude can be decreased by using the C^z-element pulse

developed in the previous chapter. For the C^z-element pulse with e.g. $a = 300°$, the shortest pulse width required in the element pulse is 1.43 μsec. Further decrease in a needs even shorter minimum pulse width. The use of the C^z-element pulse that needs the pulse width shorter than 1 μsec may be limited by the ability of the hardware that implements the pulse sequence.

3.2.2 Hamiltonian during a cycle

CH hetero nuclear dipolar term

The heteronuclear dipolar interaction between ^{13}C and ^{1}H spins during ^{1}H–^{1}H mixing is zero in the first averaging step of Eq (3.17). Thus, the residual CH dipolar couplings affect the experimental result only through the cross terms to the recoupled ^{1}H DQ-dipolar terms in the second or higher order correcting terms of the average Hamiltonian. The second-order cross term is written as

$$\overline{\mathcal{H}}^{(2)}(N\tau_{\mathrm{c}}) = \sum_{\Lambda_1,\Lambda_2} \overline{\mathcal{H}}^{\Lambda_1\times\Lambda_2}_{lm\lambda\mu;l'm'\lambda'\mu'} \tag{3.24}$$

$$\overline{\mathcal{H}}^{\Lambda_1\times\Lambda_2}_{lm\lambda\mu;l'm'\lambda'\mu'} = \frac{-i}{2N\tau_{\mathrm{c}}} \int_{\tau_0}^{N\tau_{\mathrm{c}}} d\tau_2 \int_{\tau_0}^{\tau_2} d\tau_1 \left[\tilde{\mathcal{H}}^{\Lambda_1}_{lm\lambda\mu}(\tau_1), \tilde{\mathcal{H}}^{\Lambda_2}_{l'm'\lambda'\mu'}(\tau_2)\right]. \tag{3.25}$$

For example, the cross term between the homo- (II) and heteronuclear (IS) dipolar interection has the general form

$$\overline{\mathcal{H}}^{II\times IS}_{2122;2m1\mu} = \frac{1}{\omega_{\mathrm{rf}}} \sum_{i\neq j} \overline{\omega_{Sij}} S_z (I_{ix}I_{jy} + I_{iy}I_{jx} - I_{ix}I_{jx} + I_{iy}I_{jy}), \tag{3.26}$$

where $\overline{\omega_{Sij}}$ is calculated from the commutator in Eq (3.25).

The large mixing field amplitude for POST-C7 is beneficial becase the cross terms that depend on $(1/\omega_{\mathrm{rf}})$ and higher powers can be truncated in the effective Hamiltonian. Under our experimental settings for POST-C7 with $\gamma B_1 = 91$ kHz, the effect of the residual CH dipolar coupling can be safely neglected. This is in contrast to the ^{13}C recoupling case where the residual CH dipolar couplings broaden the ^{13}C line with the strong ^{1}H–^{1}H dipolar couplings. Thus, in the ^{13}C recoupling case, second averaging by MAS and ^{1}H decoupling field is needed to supress the residual CH dipolar couplings. When the ^{13}C-mixing, and ^{1}H decoupling field amplitudes approaches to the Hartman-Hahn matching condition,

$\omega_{\mathrm{mix},^{13}\mathrm{C}} = \omega_{\mathrm{dec},^1\mathrm{H}}$, the partially recoupled CH dipolar interaction reduces the ^{13}C magnetization. Thus, the ^{13}C line is a complex function of the absolute field strength as well as the mismatch ratio of the ^{1}H decoupling and ^{13}C mixing fileds in addition to MAS frequency as described in Ref [13]. For the ^{1}H recoupling case, one is free from all these issues. The mixing field amplitude is limited in the ^{1}H recoupling case by the power capability of a probe, rather than the mixing- and decoupling-fileds matching effect in the ^{13}C case.

Zero-quantum dipolar term

While the ^{1}H zero-quantum (ZQ) dipolar interaction during POST-C7 is not yet zero in the first averaging step of Eq.(3.17), it *is* after the z rotational averaging in Eq.(3.18). Figure 3.6 shows the magnitude of the real and imaginary part of the phase factor seen in Eq.(3.15) associated with the ZQ term $\tilde{\mathcal{H}}^{II}_{2120}$ as a function of the recoupling time. It is shown that the ZQ term that has non-zero intensity after one element pulse irradiation is suppressed during the z rotational averaging. The same decoupling event of the ZQ term was also seen in the numerically exact calculation of the norm of the ZQ term during the recoupling time shown in Fig.3.7. Figure 3.7 also shows that the CH dipolar term is already eleminated after one element pulse irradiation. Note also that the DQ term is established already at only one element pulse irradiation, and is dominant at $\tau_{\mathrm{m}} = 3\tau_{\mathrm{c}}$, while the AHT assures the dominance only at $\tau_{\mathrm{m}} = 7\tau_{\mathrm{c}} = 2\tau_{\mathrm{R}}$. The dominance of the focal DQ-dipolar term at mixing time shorter than $7\tau_{\mathrm{c}}$ is beneficial for the application of POST-C7 to the ^{1}H recoupling experiment because it enables the observation of the ^{1}H spin dynamics at higher time resolution. This feature is important because the ^{1}H DQ-evolution frequency $|\omega^{+}_{\mathrm{DQ}}|$ of the system under the recoupled interaction should be very large because of the large magnetogyric ratio of ^{1}H spin. Also,

it is because the ^{1}H magnetization transferred by the DQ process with positive and negative signs, rapidly cancelling each other.

3.3 Experimental Results

3.3.1 Analysis of distances

The evolution of a nuclear spin system under the effect of the dipolar interaction can be analyzed to estimate internuclear distance. We employed POST-C7 to recouple the ^{1}H DQ-dipolar interactions. The pulse scheme shown in Fig.3.1 was applied to polycrystalline sample of uniformly ^{13}C- and ^{15}N-labeled valine hydrochloride (Val·HCl). With the pulse scheme shown in Fig.3.1(c), the magnetization was selectively excited on C$^\alpha$, transferred to H$^\alpha$, mixed with POST-C7, and returned to ^{13}C spins for detection. Figure 3.8 shows one-dimensional spectra of Val·HCl obtained (a) with CPMAS, and (b) the pulse scheme of Fig.3.1(c) at indicated ^{1}H DQ-dipolar mixing times. The negative C$^\beta$ signal in Fig.3.8(b) shows the magnetization transferred along the pathway C$^\alpha$ $\rightarrow$H$^\alpha$ $\rightarrow$H$^\beta$ $\rightarrow$C$^\beta$. We call here the NMR signal of C$^\alpha$ as a diagonal peak, and that of C$^\beta$ as a cross peak in analogy to the two-dimensional correlation spectrum. The diagonal and cross peak intensities $M^{\rm exp}$ measured at a series of mixing times $\tau_{\rm m} = \frac{2\tau_{\rm R}}{N} i$ are plotted in Figs.3.9(b) and (c) by open and filled circles, respectively. Means of five experimental observations are shown for each intensity $M^{\rm exp}(\tau_{\rm m})$. All intensities were normalized to that of the diagonal signal at $\tau_{\rm m} = 0$. The distribution of the measurement in $M^{\rm exp}(\tau_{\rm m})$ are shown in the Fig.3.9(c) by error bars. The distribution of the measurement in $M^{\rm exp}(\tau_{\rm m})$ averaged over $\tau_{\rm m} = 0$ to 150 μs was $\sigma^2 \approx 1.5 \times 10^{-5}$, indicating very small uncertainty in the measurement. In Figs.3.9(b) and

(c), lines show the signal intensities obtained by exact numerical simulations, for which we assumed a 7-spin model of the valine molecule as shown in Fig.3.9(a). The 7-spin model includes H^{α}–C^{α}–C^{β}–H^{β} segment and ^{1}H spins of two γ methyl groups, H^{γ_1} and H^{γ_2}, as well as that of the amino group H^N. The simulated intensities $M^{\rm cal}(\tau_{\rm m}, \mathbf{\Gamma})$ are determined by a set of structural parameters $\mathbf{\Gamma} = (d_{\alpha\beta}, d_{\rm ch}, \phi_{\rm hcch}, \theta_{\rm c^{\alpha}hh})$, in which $d_{\alpha\beta}$ is a H^{α}–H^{β} distance, $d_{\rm ch}$ is a ^{13}C–^{1}H bond length, $\phi_{\rm hcch}$ is a dihedral angle, and $\theta_{\rm c^{\alpha}hh}$) is C^{α}–H^{α}–H^{β} angle. The dashed, solid, and dotted lines were calculated with the structural parameters $\mathbf{\Gamma}^{\rm C}$, $\mathbf{\Gamma}^{\rm G}$, and $\mathbf{\Gamma}^{\rm T}$, corresponding respectively to that of the rotational isomers of Val·HCl in *cis*, *gauche*, and *trans* conformations. The parameter sets $\mathbf{\Gamma}^{\rm C} = (217{\rm pm}, 109{\rm pm}, 0°, 73°)$, $\mathbf{\Gamma})^{\rm G} = (247{\rm pm}, 109{\rm pm}, 67.6°, 59°)$, $\mathbf{\Gamma})^{\rm T} = (302{\rm pm}, 109{\rm pm}, 180°, 28°)$ were generated from the structure data of Val·HCl by neutron diffraction study [22]. Filled circles and solid line in Fig.3.9(c) show that experimental and simulated buildup curve of the cross peak intensity agrees well at $\tau_{\rm m} \lesssim 200$ μs. The 7-spin model has taken into account the effect of virtually all intramolecular ^{1}H spins, thus the agreement seen for the cross peak buildup curves suggests that only the intramolecular protons are important to analyze the cross peak intensity at short mixing times. The deviation of the cross peak intensities between the experiment and simulation seen at longer mixing time $\tau_{\rm m} > 200$ μs may be due either to the effect of the intermolecular ^{1}H couplings or the static structural heterogeneity of the crystalline sample. The deviation between experiment and simulations seen for the diagonal peak intensities may be due to the effect of the large number of intra- and intermolecular ^{1}H dipolar couplings that affect the decay of the diagonal peak intensity even at the short mixing time.

In Fig.3.10, values of the chi-squares calculated with experimental data and simulations at $\mathbf{\Gamma} = \mathbf{\Gamma}^{\rm C}, \mathbf{\Gamma}^{\rm G}$, and $\mathbf{\Gamma}^{\rm T}$ are plotted to locate a minimum of χ^2 for the three stable

rotation isomers of Val·HCl. In the above, χ^2 is defined as the sum of the squares of the deviations between the experimental $M^{\rm exp}(\tau_{\rm m})$ and simulated data $M^{\rm cal}(\tau_{\rm m})$ as

$$\chi^2/\delta = \delta^{-1}\sum_i \frac{\left\{M^{\rm exp}\left(\frac{2\tau_{\rm R}}{7}i\right) - M^{\rm cal}\left(\frac{2\tau_{\rm R}}{7}i\right)\right\}^2}{\sigma_i^2}, \tag{3.27}$$

where δ is the number of degrees of freedom in the data sets, $\tau_{\rm R}$ is a sample rotation period, and σ_i is the standard deviation of the experimental measurements at the i-th time point. Figure 3.10 indicates that the most probable structure may be found with the *gauche* conformer.

Before we refine the least-sqares fitting of the data with simulations, we examined the impact of the structure parameters on the measurement $M^{\rm exp}(\tau_{\rm m})$. For this purpose, we assumed a virtual 4-spin system illustrated in Fig.3.11(a), involving two ^{13}C and two ^{1}H spins. With this model, the relative orientation of the ^{13}C–^{1}H and ^{1}H–^{1}H dipolar coupling tensors can be changed without changing ^{1}H–^{1}H distance. The conformation of the virtual 4-spin system is determined with a parameter set $\mathbf{\Gamma} = (d_{\rm hh}, d_{\rm ch}, \phi_{\rm chhc}, \phi_{\rm chh}) = (247{\rm pm}, 109{\rm pm}, a, 108^\circ)$, in which $d_{\rm hh}$ is a interproton distance, $d_{\rm ch}$ is a CH bond length, $\phi_{\rm chhc}$ is a dihedral angle, and $\phi_{\rm chh}$ is a CHH bond angle. For the 4-spin model with several dihedral angles a, we compared the impact of a parameter change by calculating rmsd:

$$R(\mathbf{\Gamma}, \mathbf{\Gamma}') = \sqrt{\sum_{i=0}^{N} \frac{\left\{M^{\rm cal}(\frac{2\tau_{\rm R}}{7}i, \mathbf{\Gamma}) - M^{\rm cal}(\frac{2\tau_{\rm R}}{7}i, \mathbf{\Gamma}^+)\right\}^2}{N+1}}. \tag{3.28}$$

Above, rmsd is defined as a mean squared difference of two simulations $M^{\rm cal}(\frac{2\tau_{\rm R}}{7}i, \mathbf{\Gamma})$ and $M^{\rm cal}(\frac{2\tau_{\rm R}}{7}i, \mathbf{\Gamma}^+)$, in which the two different parameter sets $\mathbf{\Gamma}$ and $\mathbf{\Gamma}'$ involves a change in only one of four parameters by small amount. The small amount change in each parameter is assumed here as $\Delta d_{\rm hh} = 7$pm, $\Delta d_{\rm ch} = 7$pm, $\Delta\phi_{\rm chhc} = 10^\circ$, and $\Delta\phi_{\rm chh} = 10^\circ$. The change in ^{1}H–^{1}H distance by 7pm corresponded to that in the dihedral angle by 10° in the HCCH moiety of Val·HCl. In Fig.3.11(b), the rmsd defined above are shown as a function of the

dihedral angles. It is shown in a broad range of the dihedral angle ϕ_{chhc} that the measurement $M^{\mathrm{cal}}(\tau_{\mathrm{m}}, \mathbf{\Gamma})$ are sensitive to ^{1}H–^{1}H and ^{13}C–^{1}H distances rather than the dihedral angle and CHH bond angle. Exception is the large rmsd associated with the dihedral angle change aroung $\phi_{\mathrm{chhc}} \approx 160°$. This suggests that the heteronuclear CH dipolar interaction remains anisotropic during very short LGCP periods used in our pulse scheme of Fig.3.1. Overall, the measurement in the present method is largely insensitive to the dihedral and bond angles.

With this conclusion, only the H$^\alpha$–H$^\beta$ distance $d_{\alpha\beta}$ and the CH bond length d_{CH} were treated as adjustable parameters in the refinement of the least-square simulation, holding the HCCH diheadral angle ϕ_{hcch} and CHH bond angle ϕ_{chh} fixed at their values known by the neutron diffraction study [22]. The least-squares fitting of the experimental intensity data $M^{\mathrm{exp}}(\tau_{\mathrm{m}})$ with simulations $M^{\mathrm{cal}}(\tau_{\mathrm{m}}, d_{\alpha\beta}, d_{\mathrm{ch}})$ yielded most probable values $d_{\alpha\beta}^{\mathrm{NMR}} = 248$ pm and $d_{\mathrm{CH}}^{\mathrm{NMR}} = 109$ pm.

Figure 3.12 is a contour plot of χ^2 for the least-squares fitting as a function of two parameters $d_{\alpha\beta}$ and d_{CH}. The χ^2 contours follow elliptical paths tilted relative to the coordinate axis, indicating a strong correlation between $d_{\alpha\beta}$ and d_{CH}. From the $\Delta\chi^2 = 1$ contour, we estimated the uncertainties in $d_{\alpha\beta}^{\mathrm{NMR}}$ and $d_{\mathrm{CH}}^{\mathrm{NMR}}$ were about ± 4 pm for both. The determined distances here by NMR $d_{\alpha\beta}^{\mathrm{NMR}} = 248 \pm 4$ pm and $d_{\mathrm{CH}}^{\mathrm{NMR}} = 109 \pm 4$ pm are in close agreement with that determined by neutron diffraction study, $d_{\alpha\beta}^{\mathrm{NEU}} = 246.5 \pm 0.5$ pm and $d_{\mathrm{CH}}^{\mathrm{NMR}} = 109.9 \pm 0.5$ pm. Small discrepancies between values obtained by two methods is probably because of the different averaging effects of the molecular libration in the two methods [25, 26].

3.3.2 Effects of multispin

Simulations shown in Fig.3.9(c) show that the buildup curves of the cross peak intensity diplay large-amplitude oscillations for short distances $d_{\alpha\beta} \leq 250$ pm. On the other hand, the simulation for the *trans* conformer with $d_{\alpha\beta} \approx 300$ pm shows a very small ocillation indicated by a dotted line in Fig.3.9(c). From this observation, the precision of the ^{1}H–^{1}H distance measurement for $d_{\alpha\beta} \approx 300$ pm is expected to be reduced. This is conceivably because the intramolecular H^γ spins for the *trans* conformer locate close to H^α spin, and have larger dipolar effect on H^α spin than that of H^β spin. To inspect the effect of the intramolecuar H^γ spins on the precision of the distance measurement, we simulated the cross peak intensities with a 4-spin model shown in Fig.3.13(a) that involves no ^{1}H spin other than H^α and H^β. We compared the simulations with that obtained with the 7-spin model defined in Fig.3.9(a), in which the effects of all intramolecular ^{1}H spins were taken into account. In Fig.3.13 the rmsd defined in Eq.(3.28) associated with $\Delta d_{\alpha\beta} = 7$ pm are shown for three rotation isomers of the 4-spin and 7-spin models. The values were normalized to that obtained with *cis* conformers of the respective spin system. The rmsd calculated for *gauche* and *trans* conformers were smaller than that calculated for *cis* conformer in both 4- and 7-spin models. This may be due to the slow change of $d_{\alpha\beta}$ around the dihedral angle $\phi_{\mathrm{hcch}} \approx 170°$. With the 7-spin model, the rmsd at *trans* conformer was about 2/3 of that at *gauche* conformer. The decrease in rmsd was larger for the 7-spin model than that for the 4-spin model, indicating that the presence of the intramolecular H^γ spins introduces an additional decrease of the precision of the distance measurement.

3.3.3 Application to two-dimensional spectra

In the previous sections, we fully analyzed the buildup curve of the cross peak intensities with the lease-squares simulations to precisely measure the internuclear distances $d_{\alpha\beta}$ and d_{CH}. Alternatively, the data can be analyzed more roughly with the cross peak intensities in the two-dimensional correlation spectrum measured at a selected mixing time as is done in the liquid-state 2D-NOESY experiments.

Figure 3.14 shows a two-dimensional spectrum obtained with the pulse scheme shown in Fig.3.1(b). We indexed two signals assigned to C^{γ} spins as $C^{\gamma 1}$ and $C^{\gamma 2}$ from lower field side. Cross peaks correlating the chemical shifts of C^{α} with that of C^{β} and C^{γ_1} both have negative intensities as indicated by dashed contour lines. This indicates that H^{α} has a direct dipolar coupling to both H^{β} and H^{γ^1} spins. The cross-peak intensities at short mixing time $\tau_{\mathrm{m}} \lesssim 200\ \mu$sec can be related to the ^{1}H–^{1}H distances of a directly coupled pair. The 2D spectrum resolves four ^{1}H–^{1}H correlation peaks, suggesting that the present method is potential to provide many ^{1}H–^{1}H distance constraints in a single measurement.

The cross peak that correlates C^{α} only to $C^{\gamma 1}$ was seen in Fig.3.14 at the mixing time chosen. This is an evidence that indicates that the $C^{\gamma 1}$ signal corresponds to a ^{13}C spin at near-*gauche* position relative to H^{α} spin. The cross peak intensities observed for $C^{\gamma 2}$ signal generally smaller than that for $C^{\gamma 1}$ signal is consistent with this assignment (Fig.3.15). The assignment of the two stereochemically distinct C^{γ} spins in a valine side chain was straightforward based on the ^{1}H–^{1}H proximity indicated with our method. Same assignment may also be obtained with other methods by determining the relative orientation of two CH dipolar tensors [27], or by stereo-specifically deutrating the γ methyl protons.

3.4 Discussion

Figure 3.12 has shown that the precision of the measured distances $d_{\alpha\beta}^{\mathrm{NMR}}$ and $d_{\mathrm{CH}}^{\mathrm{NMR}}$ was limited by a strong correlation between the two. The error width of about 8 pm for $d_{\alpha\beta}^{\mathrm{NMR}} = 248$ pm and $d_{\mathrm{CH}}^{\mathrm{NMR}} = 109$ pm correspond to the relative uncertainty of $u = 3.3$ % and8 %, respectively.

The precision in $d_{\alpha\beta}^{\mathrm{NMR}}$ also depends on the extent to which the indirect coherence transfer pathways dominate the cross peak intensity at short mixing time. In another words, the precision depends on the number of surrounding ^{1}H spins that indirectly participate to the magnetization exchange between a ^{1}H–^{1}H pair of interest. Simulations shown in Fig.3.13 have shown that the intramolecular H$^{\gamma}$ spins decrease the precision of the ^{1}H–^{1}H distance measurement. This is bacause the intramolecular H$^{\gamma}$ spins locate closest to H$^{\alpha}$ spin in the *trans* conformer. The magnetization transfer among many dipolar couplings is dominated by that through the strongest coupling due to the effect known as the dipolar truncation. As a consequence, the sensitivity of the cross peak intensities to H$^{\alpha}$–H$^{\beta}$ distance was significantly reduced. The decrease of R for the *trans* conformer by a factor of 1.5 compared to that for the *gauche* conformer suggests 1.5 times larger uncertainty in $d_{\alpha\beta}^{\mathrm{T}} \approx 300$ pm for the *trans* conformer compared with that in $d_{\alpha\beta}^{\mathrm{G}} \approx 250$ pm for with the *gauche* conformer. Remembering the error width of about 8 pm for $d_{\alpha\beta}^{\mathrm{NMR}} = 248$ pm in Val·HCl sample, that for $d_{\mathrm{hh}} \approx 300$ pm should be about $1.5 \times 8 = 12$ pm, which corresponds to the relative uncertainty of $u = 4$ %.

Our method estimates longer distance in lower precision. Nevertheless, the relative uncertainty $u \approx 3.2$ % achieved for $d_{\alpha\beta}^{\mathrm{NMR}} = 248$ pm is satisfactory in comparison to ^{1}H–^{1}H distance previously determined by the DQ sideband method [4], 260 ± 15 pm ($u =$

5.8 %), and ^{13}C–^{13}C distance determined by DRAWS DQ-dipolar correlation experiment [28], 303 ± 20 pm ($u = 6.6$ %) and 246 ± 15 pm ($u = 6.1$ %). Thus, the detailed analysis of the cross peak buildup curve can yield precise measurement of distances $d_{\alpha\beta}$ and d_{CH}. With such distance constraints, one can determine the conformation of the valine side chain assuming the HCC bond angle and CC bond length. Our experiment is insensitive to these structural parameters, thus they should be determined with independent experiment(s). In the least-square simulations performed in the present study, data known from the neutron diffraction study were used.

The pulse schemes used in the present study shown in Fig.3.1(b)(c) resulted in a spectrum with relatively small S/N ratio. We here compare our method with 2D DRAWS DQ-dipolar recoupling experiment that was previously used for ^{13}C–^{13}C distance measurement [28]. With the DRAWS experiment in general, the magnetization flows as ^{13}C$\rightarrow$[mix]$\rightarrow^{13}$C$'\rightarrow$[^{13}C-detection], in which the spins at different site in a molecule is distinguished with a prime, and the coherence transfer steps are indicated by arrows. With the same notation, the pulse scheme shown in Fig.3.1 is written as ^{13}C$\Rightarrow^{1}$H$\rightarrow$[mix] $\rightarrow^{1}$H$'\Rightarrow^{13}$C$'\rightarrow$[^{13}C-det.]. Our scheme thus includes two extra cross polarization periods at the steps indicated by broad arrows. Since miximum polarization transfer efficiency by LGCP is ≈ 70 %, our method should possesses the S/N ratio about 2 times smaller or less than the DRAWS experiment at $\tau_{\mathrm{m}} = 0$.

Further decrease in the S/N ratio occurs for both methods during the mixing periods $\tau_{\mathrm{m}} > 0$ but stronger decrease was observed for our method than the DRAWS experiments. The maximum cross peak intensity observed for H$^{\alpha}$–H$^{\beta}$ correlation with Val·HCl sample was only 8% of the initial diagonal C$^{\alpha}$ signal intensity. This is very small compared to that

seen in the DRAWS experiment for a ^{13}C–^{13}C distance that can provide identical geometrical information. The determination of the valine sidechain conformation is also possible by measuring ^{13}C–^{13}C distance between carboxyl and γ-methyl carbons that are separated by ≈ 300 pm. In the DRAWS experiment, the cross peak correlating the ^{13}C–^{13}C distance of $d_{\mathrm{CH}} \approx 300$ pm displayed a maximum intensity of about 40% of the initial diagonal intensity during the DQ-dipolar mixing. Such large difference of the maximum cross peak intensity seen in the ^{1}H and ^{13}C recoupling experiments may be attributed to the difference of the dipolar coupled spin cluster size that is formed during the mixing period in the two experiments. Many indirect coherence transfer pathways among such spin cluster leads to cancellation of positive and negative cross peaks under the effect of the DQ-dipolar interactions. In the DRAWS experiment, ^{13}C spins were selectively isotope labeled at only 3 sites in a molecule and further the lebeled molecules were diluted with natural abandunce molecules. In contrast, in our experiment with Val·HCl, 12 intramolecular ^{1}H spins are present, and further the naturally abandunt ^{1}H spins in the sample are free from forming large spin clusters disregard to the intra- and intermolecuar couplings. Thus, in our experiment also, the any way that can reduce the ^{1}H spin cluster size is expected to relax the rapid decay of the cross peak intensity during the mixing period. The extensive deutration of the sample molecule is one of conceivable method.

Alternatively to the DQ-dipolar interaction, use of the ZQ counterpart to the ^{1}H magnetization mixing may increase the S/N ratio by about 20 % compared to that of the DQ-mixing scheme. Another conceivable merit of the ZQ-mixing version of the present method is that it provides, although imprecise, the medium-to-long range ^{1}H–^{1}H distance estimates under the diffusion approximation of the ^{1}H magnetization exchange. In summary,

the DQ-version is talented to provide short ^{1}H–^{1}H distance constraints in high precision, and the ZQ-version is suited for producing long range constraints in reduced precision but high spectral sensitivity.

Large sensitivity enhancements were obtained in solution-state NMR by the indirect detection of ^{13}C magnetization via ^{1}H NMR signals. The the S/N ratio enhancement of our method should be possible by developing the pulse scheme of Fig.3.1 to detect the spectrum via ^{1}H free-induction singals as ^{13}C$\Rightarrow$^{1}H$\rightarrow$[mix]$\rightarrow$^{1}H$'\rightarrow$[^{1}H-acq.] under the ultra-fast MAS conditions $\nu_{\mathrm{R}} > 30$ kHz [29, 30].

Finally, our method cannot separately measure the distances to geminal protons, e.g. in the methylene group, because the ^{13}C signals are finally detected for the resolution of the spectra. Distinguished measurement of a distance to one of the geminal protons is enabled by the stereochemically-specific deutration of one of the geminal proton. This increases the validity of the ^{1}H–^{1}H distance data as a structural constraint.

3.5 Conclusion

Our method presented here alleviated the low resolution of the ^{1}H spectroscopy by detecting the ^{1}H magnetization via ^{13}C free-induction signals. The present method was appled to powder sample of the fully ^{13}C-labeled L-valine, and internuclear distance $d_{\alpha\beta}$ between H$^{\alpha}$ and H$^{\beta}$ as well as the bond length d_{CH} between ^{13}C and ^{1}H in the side chain were determined. A least-square fitting of the cross peak buildup curve by treating $d_{\alpha\beta}$ and d_{CH} as adjustable parameters yielded most probable value of 248 pm and 109 pm for $d_{\alpha\beta}$ and d_{CH}, respectively, which are in agreement with the results obtained by the neutron diffraction

study on a same molecule [22]. The precision of the determined distances was found to mainly be limited by a strong correlation between $d_{\alpha\beta}^{\mathrm{NMR}}$ and $d_{\mathrm{CH}}^{\mathrm{NMR}}$, and both distances could not be determined to better than about ± 4 pm. Nevertheless, the relative uncertainty of $u = 3.3$ % for $d_{\alpha\beta}^{\mathrm{NMR}}$ is satisfactory in comparison to ^{1}H–^{1}H distance previously determined by the DQ sideband method [4], 260 ± 15 pm ($u = 5.8$ %), and ^{13}C–^{13}C distance determined by DRAWS DQ-dipolar correlation experiment [28], 303 ± 20 pm ($u = 6.6$ %) and 246 ± 15 pm ($u = 6.1$ %). Recently, Baldus *et al.* reported very similar experiment using ^{1}H DQ and ZQ mixing, in which the ^{1}H–^{1}H distance constraints are only qualitatively discussed [31]. With our method, longer ^{1}H–^{1}H distance is determined in lower precision in a normal non-deutrated sample molecule. Numerical calculations have shown that the relative uncertainty associated with the distance $d_{\mathrm{hh}} \approx 300$ pm should be $u \approx 4$ %. The method was extended to the two-dimensional measurement, and provided multiple ^{1}H–^{1}H correlations in a single 2D spectrum. Thus, the method is potential to provide many ^{1}H–^{1}H distance restraints for fully ^{13}C-labeled molecules in a single experiment.

Most recently, Oschkinat *et al.* has shown [32] that a global structure of 62-residue protein can be derived with solid-state NMR. There, many long range ^{13}C–^{13}C distance constraints up to ≈ 700 pm were used for the structure calculation. Such long range constraints were first enabled to be detected by the use of the site-directed ^{13}C labeling technique to provide multiple samples with different ^{13}C spin dilution patterns. In this respect, the advantage of the method introduced here is clear. The present method allows to get multiple of the ^{1}H–^{1}H distance constraints with a single fully-labeled sample in a single two-dimensional correlation spectrum.

In the foreseeable future, techniques that provide ^{1}H–^{13}C and/or ^{1}H–^{15}N con-

straints will also be important. Moreover, the application of three-dimensional correlation techniques to resolve e.g. ^{13}C–^{13}C correlation spectra by ^{15}N chemical shifts will be called for studying large molecular systems. The combined use of these wealth of solid-state NMR techniques should open up a way for the molecular structure analysis for isotope-labeled peptides, proteins, other organic and inorganic materials and polymers.

3.6 Experimental

3.6.1 NMR measurement

All NMR spectra were acquired with a 3.2ϕ double-resonance MAS probe, on a Varian Infinity-plus 500 spectrometer operating at the ^{13}C-resonance frequency of 125.1 MHz. The powder of valine was purchased from Shoko Co. Ltd., Japan and was re-crystallized under acidic condition in the presence of chloride ions to form small crystallites of valine hydrochrolide, L-Val·HCl. All experiments were carried out at the sample-spinning rate of 13 kHz. The LGCP periods of very short duration, $\tau_{\rm LG} = 76.9$ μsec$= \tau_{\rm R}$, was used to emphasize the magntization exchange between covalently bonded C–H pairs. Amplitude of the rf field on ^{1}H was $\gamma B_{1,\rm H}/2\pi = 73.5$ kHz for the rectangular pulses, CP and LGCP periods, while it was $\gamma B^{\rm H}_{1,\rm H}/2\pi = 100.0$ kHz for the TPPM decoupling. Amplitude of the rf field on ^{13}C was ramped in the range $\gamma B_{1,\rm C}/2\pi = 55 - 65$ kHz for the initial CP period, while it was $\gamma B_{1,\rm C}/2\pi \sim 75$ kHz for the LGCP periods. The field amplitude on ^{13}C for the LGCP periods had to experimentally be optimized around $\gamma B_{1,\rm C}/2\pi \sim 77$ kHz, which is the first-order side band of the Hartman-Hahn condition with respect to the off-resonance irradiation on ^{1}H to remove strong dispertion-mode artifacts in the final spectra The field am-

plitude for the Gaussian-shaped selective pulse on ^{13}C in (c) was set as $\gamma B_{1,\mathrm{C}}/2\pi \sim 8$ kHz. The Gaussian-shaped pulse of 0.7 ms duration was consisted of 28 rectangular pulses of 4 μsec-long and 53 μsec-separation.

3.6.2 Numerical calculations

We used a numerical simulation technique to analyze the experimental measurement. We simulated the signal intensities resulted from the first Lee-Goldburg cross polarization (LGCP) for a time τ_{LG}, ^{1}H magnetization mixing with POST-C7 during $\tau_{mathrmm}$, and second LGCP in the pulse scheme shown in Fig.3.1, and denote these time periods as $\mathrm{LG_1}$–$\mathrm{H_{mix}}$–$\mathrm{LG_2}$. Exact numerical simulation included propagation of the initial spin state by a numerically integrated effective Hamiltonian over the time period, and its projection to the spin state observable:

$$I_{2x}(\tau_{\mathrm{E}}) = \frac{1}{8\pi^2}\int_0^{2\pi}\int_0^{\pi}\int_0^{2\pi} \mathrm{Tr}\left\{I_{2x}U(\tau_{\mathrm{E}})I_{1x}U^{\dagger}(\tau_{\mathrm{E}})\right\} d\alpha_{\mathrm{PR}} \sin\beta_{\mathrm{PR}} d\beta_{\mathrm{PR}} d\gamma_{\mathrm{PR}}, \quad (3.29)$$

in which $\tau_{\mathrm{E}} = \tau_{\mathrm{m}} + 2\tau_{\mathrm{LG}}$. In the above, the time domain signals were summed up to reproduce the powder distribution of the sample. To reduce computation time, summation was made only for about 350 crystallite orientations. A numerically exact propagator U is obtained by multiplication of propagators over short time increments, in which the elemental propagators were assumed time independent. The magic-angle sample spinning was included as a time dependent reorientation of the spin system tensor interactions with about 100 integration increments for each rotor period.

In the least-squares simulations, a model spin system of valine molecule was considered. The model system consisted of 7 spins, H^{α}–C^{α} (–H^{N}) –C^{β}–H^{β} (–H^{γ_1}) (–H^{γ_2}), in

wihch each of three geminal protons in the amino and two methyl groups were represented by one pseudo-proton H^N, H^{γ_1} and H^{γ_2}, respectively.

We approximated three dipolar couplings b_{12}, b_{13} and b_{14} of an arbitrary spin 1 to three rotating methyl or amino ^{1}H spins 2, 3, and 4 with a single coupling b_{eff} of the spin 1 to a pseudo-^{1}H spin placed on the axis of the rotating group. The exact position is determined so as to the effective coupling b_{eff} becomes as

$$b_{\text{eff}} = 1.5\kappa b \frac{\left(r_{12}^{-3} + r_{13}^{-3} + r_{14}^{-3}\right)}{3}, \tag{3.30}$$

in which b is defined in Eqs. (3.6) and (3.7),

r_{ij} is a distance between spins i and j. The scaling factor κ accounts for the effects of the dipolar interactions partially decoupled by the methyl or amino group rotation:

$$\kappa = 0.5 \times (3\cos^2\theta - 1), \tag{3.31}$$

in which θ is the aperture angle of a cone formed by spins 2, 3, 4 in the base and the spin 1. The aperture angles θ seen in the neutron diffraction structure of Val·HCl ranged between $10^\circ \lesssim \theta \lesssim 28^\circ$, which correspond to $0.68 \lesssim \kappa \lesssim 0.95$. The prefactor of 1.5 approximates three contributions of the three dipolar coupling, 1–2, 1–3 and 1–4, to one pseudo coupling. The factor was estimated by numerically calculating the dipolar line widths of a signal, and comparing the average line width of a spin 1 between spin systems H_1–(H_2,H_3,H_4) and H_1–H_2, as well as C_1–(H_2,H_3,H_4) and C_1–H_2. The factor of $\sim$1.5 was common to the homo- and heteronuclear spin systems.

In the pseudo-atom approximation, we replaced three ^{1}H spins rotating in a spatially spread area with one pseudo atom present at one fixed spatial point. The dipolar coupling expressed in the dipolar PAS ρ_{20}^{PAS} is along the z axis of the PAS, while that expressed in the molecular-fixed frame is tilted by the aperture angle θ from the z axis of the MOL

frame. Generally, the transformation of the dipolar coupling in the PAS ρ_{20}^{PAS} to the MOL frame introduces terms with $\mu \neq 0$:

$$\begin{aligned}\rho_i^{\mathrm{MOL}} &= \sum_{\gamma_{\mathrm{PR}}=0^\circ,120^\circ,240^\circ} \mathbf{R}(0,\theta,\gamma_{\mathrm{PR}})\rho_{i,20}^{\mathrm{PAS}} \\ &= \sum_{\mu} d_{\mu 0}(\beta)e^{i\mu\gamma}. \end{aligned} \tag{3.32}$$

Nevertheless, for the protons jumping at three sites, each of which is separated by the angle $\approx 120^\circ$ generated only very small $\mu \neq 0$ components, thus in our case

$$\rho_i^{\mathrm{MOL}} \approx d_{00}(\theta)\rho_{20}^{\mathrm{PAS}}. \tag{3.33}$$

This result justifies the approximation replacing the the amino and methyl ^{1}H spins by one pseudo ^{1}H spin at a average position.

Input parameters for the simulations were determined as follows: CSA tensor principal values and the orientation were assumed to be analogous as those determined by Naito *et al.* for single crystal L-alanine [33]. Internuclear distances were taken from the neutron diffraction study of Val·HCl [22]. The orientations of the dipolar tensors for molecular segments in different conformations were determined by rotation of a separate molecular segment relative to the molecular axis.

The chi-square fitting to determine $d_{\alpha\beta}$ and d_{CH} was made with 4 data points acquired at the mixing times $\tau_{\mathrm{m}} = \frac{2\tau_{\mathrm{R}}}{7}i$, $i = 2, 4, 6, 7$. The fitting assumed $\delta = 2$ degrees of freedom, i.e. 4 data points with two independent parameters to determine. The location of the minimum χ^2/δ was calculated by fitting a parabola through the three χ^2 data that straddle the minimum. The uncertainty of one standard deviation in the fitted parameter x was evaluated as the deviation in the parameter x from the value for which the chi-square is minimized that cause an increase of χ^2/δ by $1/\delta$ [24].

The dipolar powder spectrum shown in Fig.3.2 was obtained by the Fourier trans-

formation of the time-dependent sum magnetization, $I_{1z} + I_{2z}$ evolved during τ_{m} under the recoupling sequence summed up for about 35×10^5 crystallite orientations. All numerical simulation programs coded in FORTRAN were rum on an SGI Origin200 workstation having four R10000 processors.

References

[1] D. E. Demco, A. Johansson, and J. Tegenfeldt, Proton spin diffusion for spatial heterogeneity and morphology investigations of polymers, *Solid State NMR* **4**, 13–38 (1995).

[2] D. L. VanderHart, and G. B. McFadden, Some perspectives on the interpretation of proton NMR spin diffusion data in terms of polymer morphologies, *Solid State NMR* **7**, 45–66 (1996).

[3] M. feike, D. E. Demco, R. Graf, J. Gottwald, S. Hafner, and H. W. Spiess, Broadband multiple-quantum NMR spectroscopy, *J. Magn. Reson. A* **122**, 214–221 (1996).

[4] J. Gottwald, D. E. Demco, R. Graf, H. W. Spiess, High-resolution double-quantum NMR spectroscopy of homonucelar spin pairs and proton connectivities in solids, *Chem. Phys. Lett.* **243**, 314–323 (1995).

[5] R. Graf, D. E. Demco, J. Gottwald, S. Hafner, and H. W. Spiess, Dipolar couplings and internuclear distances by double-quantum nuclear magnetic resonance spectroscopy of solids *J. Chem. Phys.* **106**, 885–895 (1996).

[6] I. Schnell, S. P. Brown, H. Y. Low, H. Ishida, and H. W. Spiess, An investigation of hydrogen bonding in Benzoxazine dimers by fast magic-angle spinning and double-quantum ^{1}H NMR spectroscopy, *J. Am. Chem. Soc.* **120**, 11784–11795 (1998).

[7] I. Schnell, B. Langer, S. H. M. Sonjens, M. H. P. van Genderen, R. P. Sijbesma, and

H. W. Spiess, Inverse detection and heteronuclear editing in ^{1}H–^{15}N correlation and ^{1}H–^{1}H double-quantum NMR spectroscopy in the solid state under fast MAS, *J. Magn. Reson.* **150**, 57–70 (2001).

[8] M. Edén and M. H. Levitt, Pulse sequence symmetries in the nuclear magnetic resonance of spinning solids: Application to heteronuclear decoupling, *J. Chem. Phys.* **111**, 1511–1519 (1999).

[9] M. Carravetta, M. Edén, X. Zhao, A. Brinkmann, and M. H. Levitt, Symmetry principles for the design of radiofrequency pulse sequence in the nuclear magnetic resonance of rotating solids, *Chem. Phys. Lett.* **321**, 205–215 (2000).

[10] A. Brinkmann and M. H. Levitt, Symmetry principles in the nuclear magnetic resonance of spinning solids: Heteronuclear recoupling by generalized Hartmann-Hahn sequences, *J. Chem. Phys.* **115**, 357–384 (2001).

[11] P. K. Madhu, X. Zhao, and M. H. Levitt, High-resolution ^{1}H NMR in the solid state using symmetry-based pulse sequences, *Chem. Phys. Lett.* **346**, 142–148 (2001).

[12] M. Hohwy, H. J. Jakobsen, M. Edén, M. H. Levitt, and N. C. Nielsen, Broadband dipolar recoupling in the nuclear magnetic resonance of rotating solids: A compensated C7 pulse sequence,

J. Chem. Phys. **108**, 2686–2694 (1998).

[13] M. Hohwy, C. M. Reinstra, C. P. Jaroniec, and R. G. Griffin, Fivefold symmetric homonuclear dipolar recoupling in rotating solids: Application to double quantum spectroscopy, *J. Chem. Phys.* **110**, 7983–7991 (1999).

[14] A. Brinkmann, M. Edén, and M. H. Levitt, Synchronous helical pulse sequences in magic-angle spinning nuclear magnetic resonance: Double quantum recoupling of

multiple-spin systems, *J. Chem. Phys.* **112**, 8539–8554 (2000).

[15] C. M. Rienstra, M. Hohwy, M. Hong, and R. G. Griffin, 2D and 3D ^{15}N–^{13}C–^{13}C NMR chemical shift correlation spectroscopy of solids: Assignment of MAS spectra of peptides, *J. Am. Chem. Soc.* **122**, 10979–10990 (2000).

[16] A. Brinkmann, M. Carravetta, X. Zhao, M. Edén, J. Schmidt auf der Günne, and M. H. Levitt, Using symmetry to design pulse sequences in solid-state NMR in *Perspectives on Solid State NMR in Biology*, 3–14 (Kluwer Academic Publishers, Dordrecht, 2001).

[17] R. G. Griffin, Dipolar recoupling in MAS spectra of biological solids, *Nature Struc. Biol.* NMR supplement, 508–512 (1998).

[18] C. M. Rienstra, M. E. Hatcher, L. J. Mueller, B. Sun, S. W. Fesik, and R. G. Griffin, Efficient multispin homonuclear double-quantum recoupling for magic-angle spinning NMR: ^{13}C–^{13}C correlation spectroscopy of U-^{13}C-erythromycin A, *J. Am. Chem. Soc.* **120**, 10602–10612 (1998).

[19] M. Mehring, *Principles of High Resolution NMR in Solids* (Springer-Verlag, New York, 1983).

[20] V. Ladizhansky and S. Vega, Polarization transfer dynamics in Lee-Goldburg cross polarization nuclear magnetic resonance experiments on rotating solids, *J. Chem. Phys.* **112**, 7158–7168 (2000).

[21] G. Metz, X. Wu, and S. O. Smith, Ramped-amplitude cross polarization in magic-angle-spinning NMR, *J. Magn. Reson. A* **110**, 219–277 (1994).

[22] T. F. Koetzle, L. Golic, M. S. Lehmann, J. J. Verbist, and W. C. Hamilton, Precision neutron diffraction structure determination of protein and nucleic acid components. XV. Crystal and molecular structure of the amino acid L-valine hydrochloride, *J. Chem.*

Phys. **60**, 4690-4696 (1974).

[23] R. Tycko, and G. Dabbagh, Measurement of nuclear magnetic dipole-dipole couplings in magic angle spinning NMR, *Chem. Phys. Lett*. **173**, 461– (1990).

[24] P. R. Bevington and D. K. Robinson, *Data Reduction and Error Analysis for the Physical Sciences* (WCB/McGraw-Hill, Boston, 1992).

[25] E. R. Henry and A. Szabo, Influence of vibrational motion on solid state line shapes and NMR relaxation, *J. Chem. Phys*. **82**, 4753–4761 (1985).

[26] Y. Ishii, and T. Terao, Theory and simulation of vibrational effects on structural measurements by solid-state nuclear magnetic resonance, *J. Chem. Phys*. **107**, 2760–2774 (1997).

[27] T. Fujiwara, T. Shimomura, Y. Ohigashi, and H. Akutsu, Multidemensional solid-state nuclear magnetic resonance for determining the dihedral angle from the correlation of ^{13}C–^{1}H and ^{13}C–^{13}C dipolar interactions under magic-angle spinning conditions , *J. Chem. Phys*. **109**, 2380-2393 (1998).

[28] S. R. Kiihne, K. B. Geahigan, N. A. Oyler, H. Zebroski, M. A. Mehta, and G. P. Drobny, Distance measurements in multiply labeled crystalline cytidines by dipolar recoupling solid state NMR, *J. Phys. Chem. A* **103**, 3890-3903 (1999).

[29] Y. Ishii, and R. Tycko, Sensitivity enhancement in solid state ^{15}N NMR by indirect detection with high-speed magic angle spinning, *J. Magn. Reson.* **142**, 199–204 (2000).

[30] Y. Ishii, J. P. Yesinowski, and R. Tycko, Sensitivity enhancement in solid state ^{13}C NMR of synthetic polymers and biopolymers by ^{1}H NMR detection with high-speed magic angle spinning, *J. Am. Chem. Soc*. **123**, 2921–2922 (2001).

[31] A. Lange, S. Luca, M. Baldus, Structure constraints from proton-mediated rare-spin

correlation spectroscopy in rotating solids, *J. Am. Chem. Soc.* **124**, 9704-9705 (2002).

[32] F. Castellani, B. van Rossum, A. Diehl, M. Schubert, K. Rehbein, and H. Oschkinat, Structure of a protein determined by solid-state magic-angle-spinning NMR spectroscopy, *Nature* **420**, 98-102 (2002).

[33] A. Naito, S. Ganapathy, K. Akasaka, and C. A. McDowell, Chemical shielding tensor and ^{13}C–^{14}N dipolar splitting in single crystals of L-alanine, *J. Chem. Phys.* **74**, 3190–3197 (1981).

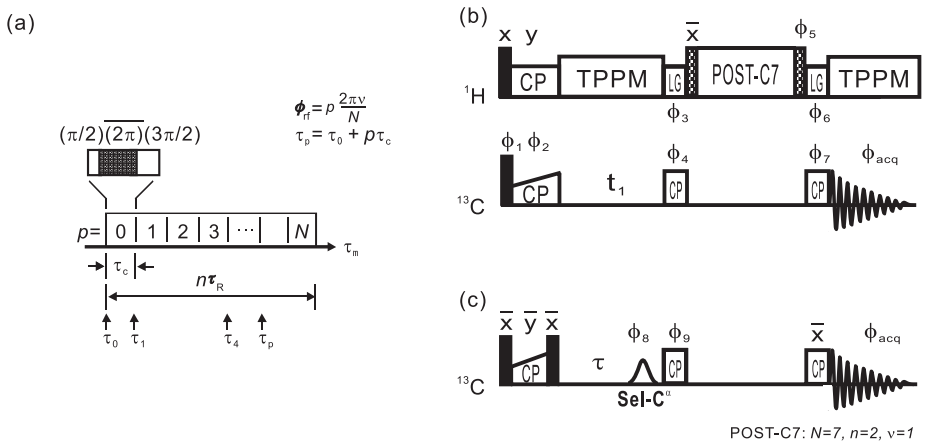

Figure 3.1: Timing scheme explaining the structure of the CN_n^ν recoupling sequence (a), the pulse sequence for a two-dimensional ^{1}H–^{1}H DQ-dipolar coupling-mediated ^{13}C/^{13}C-chemical shift correlation experiment (b), and its one-dimensional version (c). (a): The CN recoupling sequence consists of N element pulses that span n rotor revolutions. Each of the element pulse, $(\pi/2)_{0+\phi}\overline{(2\pi)}_{\pi+\phi}(3\pi/2)_{0+\phi}$, is phased so that the phase rotor-synchronously rotates in the xy plane by $\nu \times 2\pi$, i.e. p-th element pulse has a phase $\phi = p\frac{2\pi\nu}{N}$. POST-C7 with $N = 7, n = 2, \nu = 1$ was used for the ^{1}H DQ-dipolar recoupling in the scheme shown in (b). (b): Two ^{13}C-chemical shift evolution periods are connected by a period consisted of three sub-periods, namely the ^{13}C–^{1}H Lee-Goldburg cross polarization (LGCP) [20], ^{1}H–^{1}H DQ-dipolar mixing with POST-C7 and second LGCP, as we denote as $\mathrm{LG_1}$–$\mathrm{H_{mix}}$–$\mathrm{LG_2}$. The initial magnetization was prepared on ^{13}C with the ramped RF field-amplitude cross polarization [21], evolved during t_1 and submitted to $\mathrm{LG_1}$–$\mathrm{H_{mix}}$–$\mathrm{LG_2}$ block. During the LGCP periods, the effective B_1 field on ^{1}H was tilted by the magic angle from the z direction by using the phase modulation of the ^{1}H RF field. The transferred magnetization from ^{13}C to ^{1}H during the first LGCP was then mixed for τ_m with the ^{1}H DQ-dipolar interaction recoupled with POST-C7. The resultant magnetization was transfer backed to ^{13}C with the second LGCP, and observed under TPPM proton decoupling. The recycle delay was 5 s. The filled and hatched rectangular pulses represent 90° and 54.7° pulse, respectively. (c): One dimensional variant of (b). The initial magnetization on ^{13}C was flip backed to the z direction, and selectively excited on C^α with a Gaussian-shaped pulse placed after the dephasing period of duration $\tau = 1$ ms. The phase cycle was: $\phi_1 = (16\overline{x},\ 16x)$, $\phi_2 = (16\overline{y},\ 16y)$, $\phi_3 = y_-$, $\phi_4 = (8\overline{y},\ 8y)$, $\phi_5 = (x,\ y,\ \overline{x},\ \overline{y})$, $\phi_6 = (\overline{y}_+,\ \overline{x}_-,\ y_+,\ x_-)$, $\phi_7 = (4\overline{x},\ 4x)$, $\phi_8 = (8x,\ 8\overline{x})$, $\phi_9 = (4y,\ 4\overline{y})$, $\phi_\mathrm{acq} = 0202\ 20202020\ 0202\ 2020\ 02020202\ 2020$. The subscript $+$ or $-$ for ϕ_3 and ϕ_6 denotes the sign of the offset used to tilt the ^{1}H-effective field. The frequecy discrimination for the indirectly detected dimension in (b) was obtained by collecting separate real and imaginary data with ϕ_1 and ϕ_2 shifted by 90°.

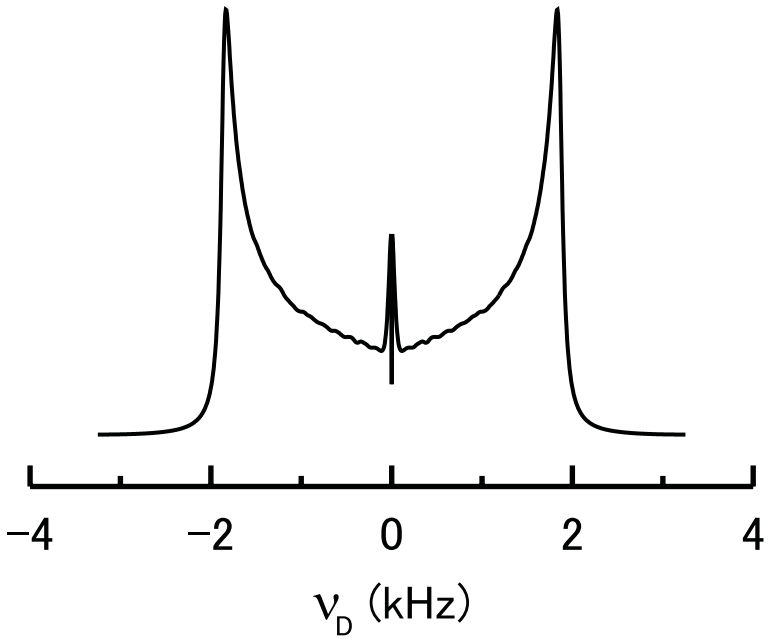

Figure 3.2: Cristallite orientation dependence of the ^{1}H DQ-dipolar interaction recoupled by POST-C7 numerically calculated with $\gamma B_{1,\mathrm{H}}/2\pi = 91.0$ kHz at $\omega_\mathrm{R}/2\pi = 13$ kHz. A $^1\mathrm{H}_1$–$^1\mathrm{H}_2$ pair separated by 246.5 pm with an identical isotropic chemical shift with no shielding anisotropy was assumed. The DQ nutation of the total Zeeman magnetization, $I_{1z}+I_{2z}$, as a function of τ_m was Fourier transformed to yield the power pattern.

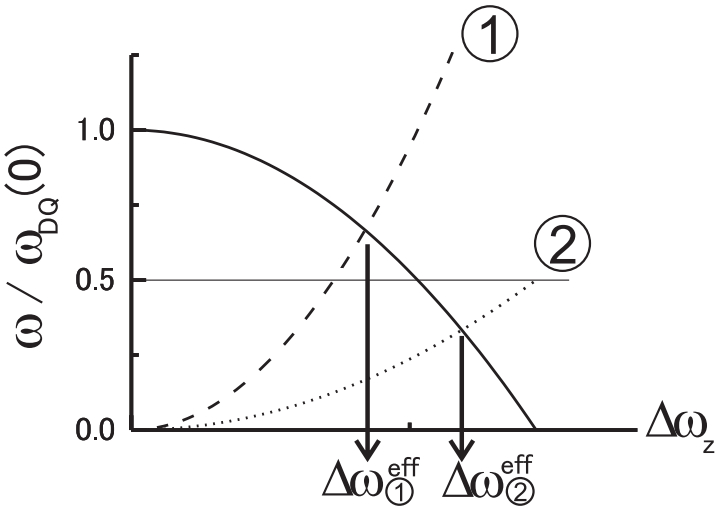

Figure 3.3: Schematic represention of decaying amplitude of the DQ-dipolar coupling $\omega_{\mathrm{DQ,j}}(\Delta\omega_z)$, and increasing amplitude of the residual spin rotation $\omega_\sigma\Delta(\omega_z)$ as a function of offset. All values are normalized to the dipolar coupling strength $\omega_{\mathrm{DQ,j}}(0)$. Dashed and dotted lines represent two cases of relatively weak and strong. dipolar couplings. The intersections of the lines that plot $\omega_{\mathrm{DQ},1}$ or $\omega_{\mathrm{DQ},2}$ and ω_σ defines the bounds $\Delta\omega_1^{\mathrm{eff}}$ and $\Delta\omega_2^{\mathrm{eff}}$ of the effective bandwidth in which the transferred magnetization is larger than 0.8 of that on resonance.

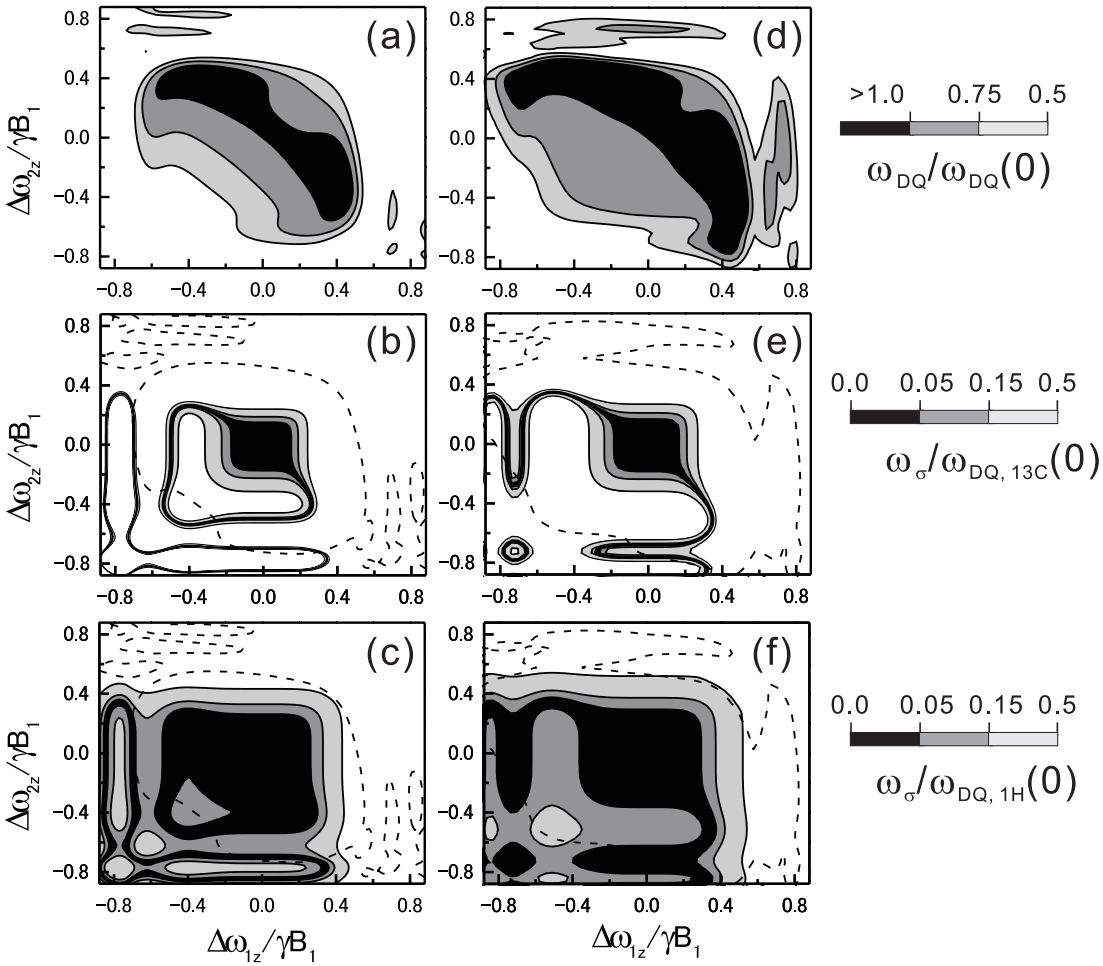

Figure 3.4: Contour plots of calculated amplitudes of the DQ-dipolar interactions normalized to the values on resonance $\omega_{\mathrm{DQ,j}}(\Delta\omega_z)/\omega_{\mathrm{DQ,j}}(0)$ (a)(b) and the residual spin rotation normalized to $\omega_{\mathrm{DQ},^{13}\mathrm{C}}$ (b)(e). The quantities are shown as a function of the offsets of two spins. The dipolar couplings recoupled with POST-C7 at the spinning frequency $\nu_{\mathrm{R}} = 13$ kHz (a)(b)(c), and SPC5 at $\nu_{\mathrm{R}} = 10$ kHz (d)(e)(f) for ^{13}C–^{13}C (b)(e) and ^{1}H–^{1}H (c)(f) spin pairs were considered. In both spin systems, chemical shift difference and the shielding anisotropies were set to zero. The internuclear distance was 220 pm in both cases. In the plots (b)(c), and (e)(f), the dashed lines indicate $\omega_{\mathrm{DQ}}(\Delta\omega_z)/\omega_{\mathrm{DQ}}(0) = 0.5$ contours in (a) and (d), respectively.

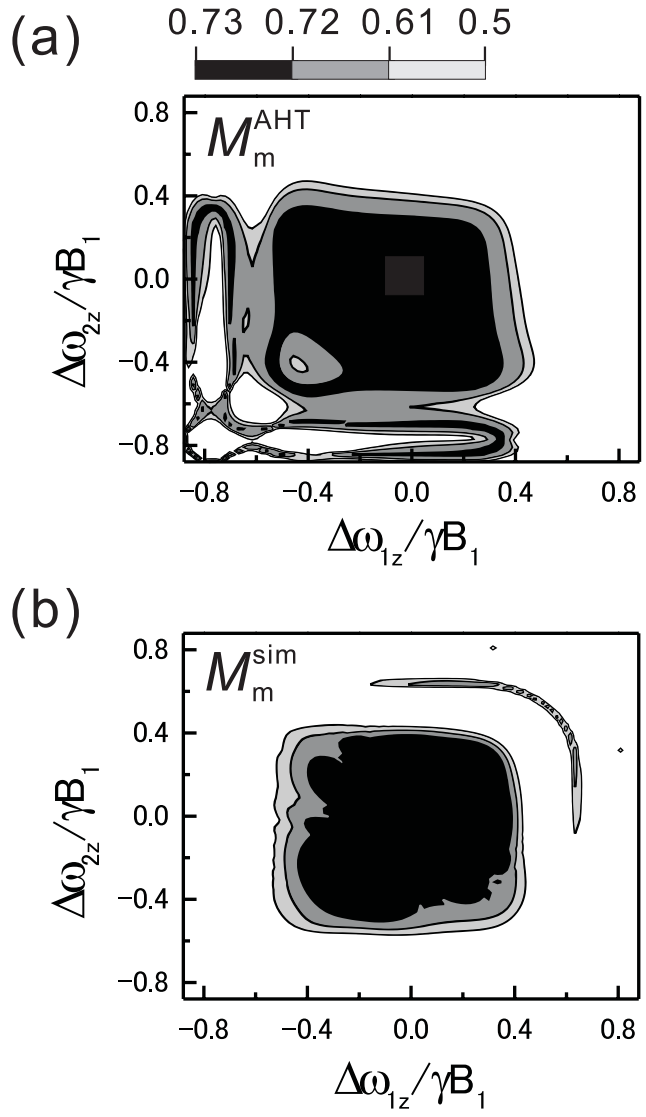

Figure 3.5: Contour plots showing the transferred magnetization calculated by the average Hamiltonian theory (AHT) M_m^{AHT} (a), and the exact numerical simulation M_m^{SIM} (b) as a function of the offsets of two spins. The DQ-dipolar interaction recoupled with POST-C7 at $\nu_{\mathrm{R}} = 13$ kHz was assumed. For a ^{1}H–^{1}H spin pair separated by 220 pm was used in the calculations, in which no chemical shift difference and shielding anisotropies were considered.

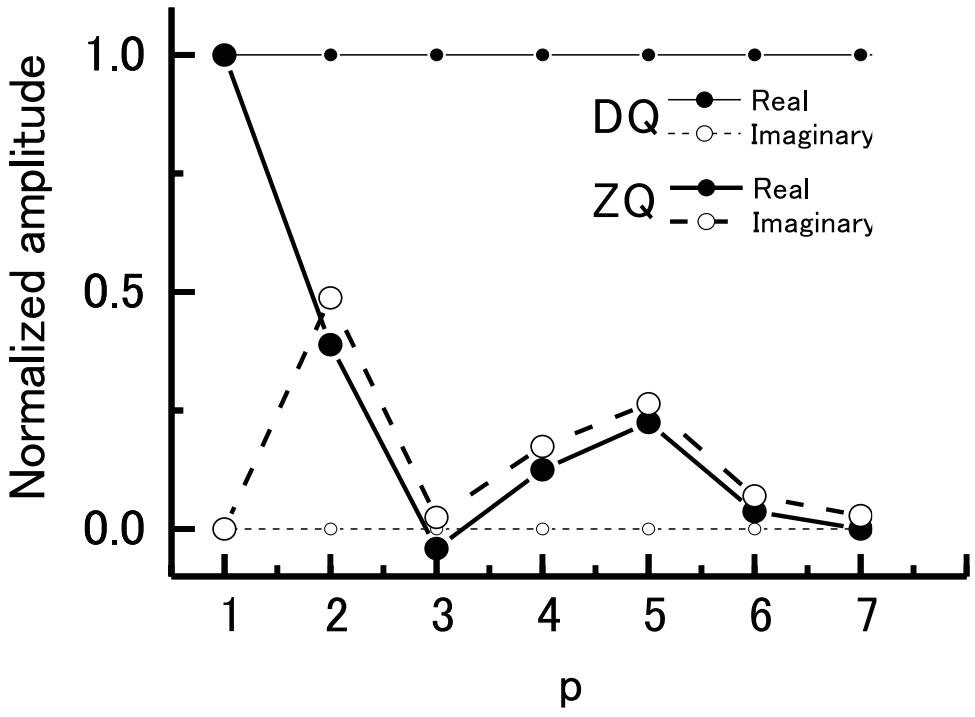

Figure 3.6: Amplitude of real (solid lines) and imaginary (dashed lines) part of the phase factor in Eq.(3.15). Amplitudes for the time period $(p-1)\tau_{\rm c} < \tau_{\rm m} < p\tau_{\rm c}$ are plotted for ZQ- (thick line) and DQ (narrow line) -dipolar interaction terms as a function of p.

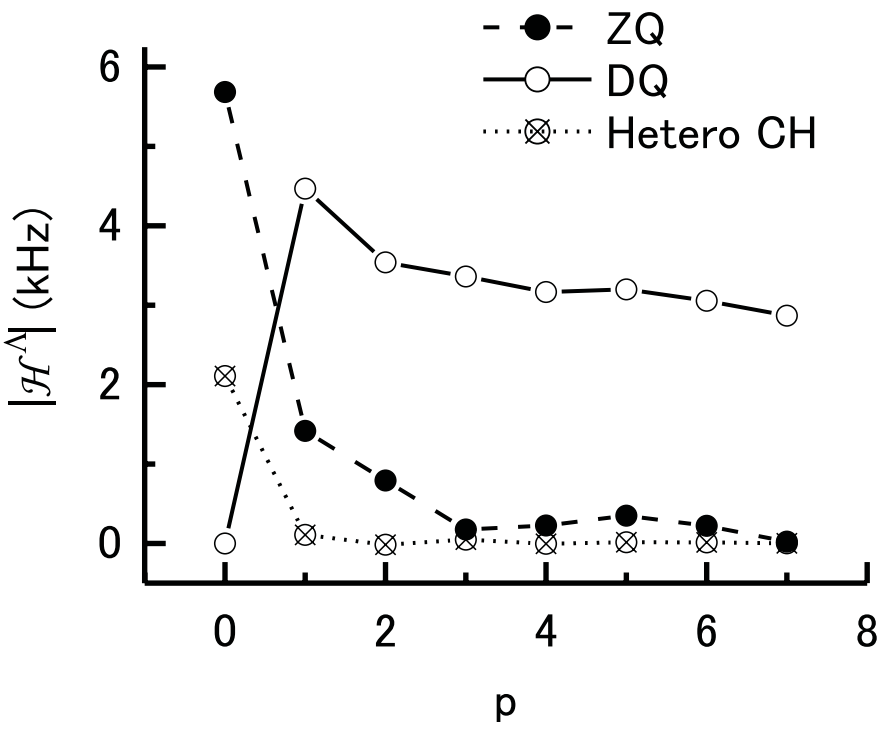

Figure 3.7: Norm of the DQ- (solid line), ZQ- (dashed line), and heteronuclear CH dipolar (dotted line) terms $||\mathcal{H}^{\Lambda}||$. The norm numerically calculated at a time point $\tau_{\mathrm{m}} = p\tau_{\mathrm{c}}$ are shown as a function of p.

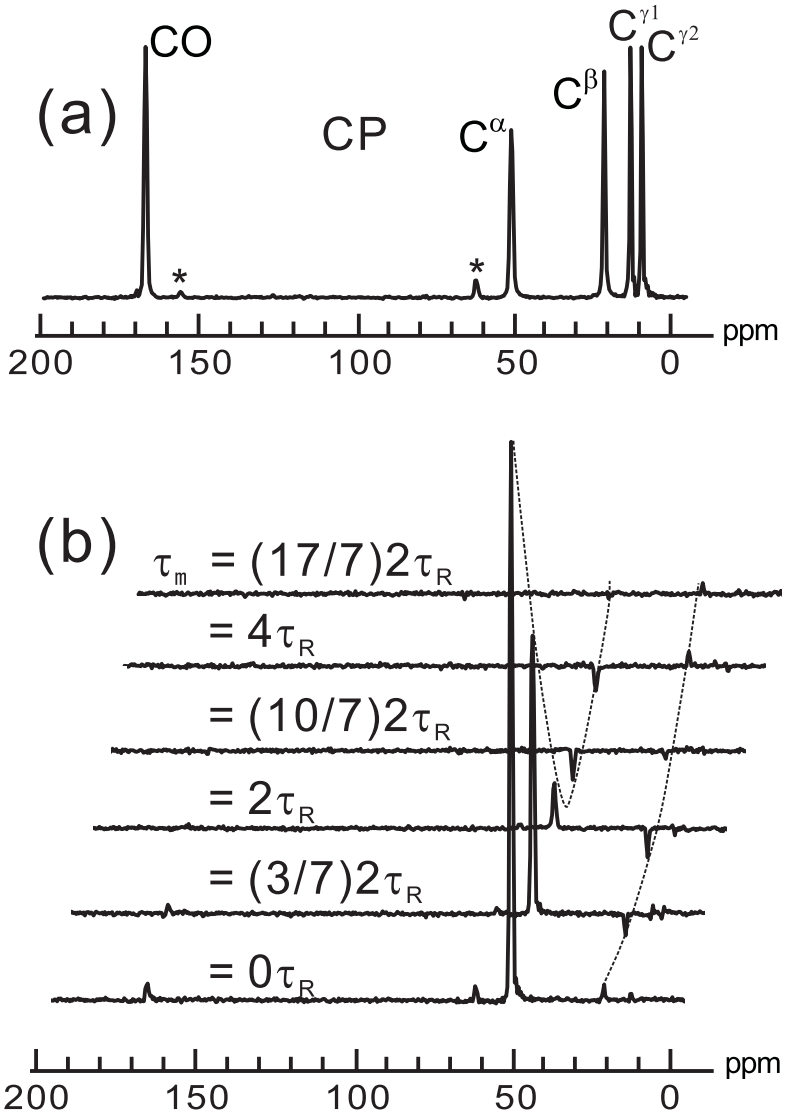

Figure 3.8: Carbon-13 chemical shift spectra of U-[^{15}N, ^{13}C] L-valine hydrochloride obtained with CP MAS (a), and with the pulse scheme shown in Fig.3.1(c) at the mixing time τ_{m} indicated (b). The sample spinning rate was 13 kHz. The asteriscs denote the spinning side bands.

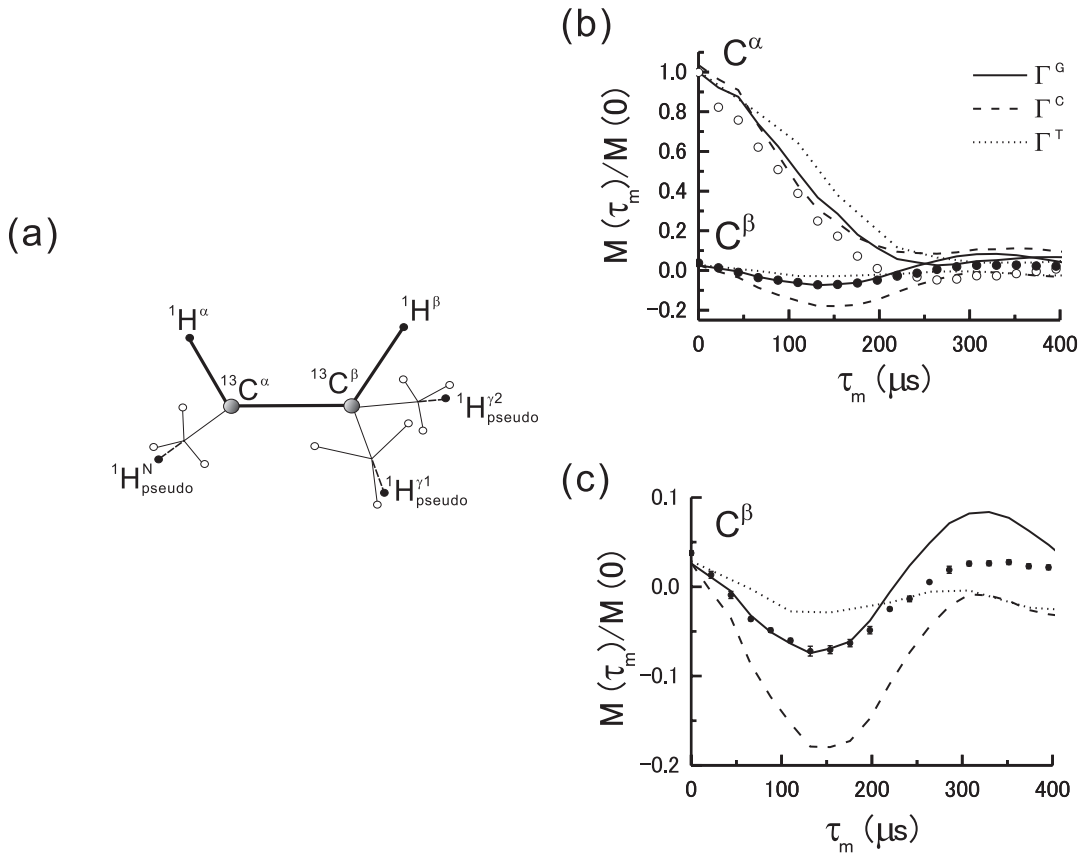

Figure 3.9: (a) Model spin system of valine that involves two ^{13}C and five ^{1}H spins. In the amino and two methyl groups, three geminal ^{1}H spins (open sphares) are replaced with a pserdo ^{1}H spin for each group. The approximation with the pseudo atom replacement is justified in Experimental section. (b) Signal intensities recorded with the pulse scheme shown in Fig.3.1(b) with a series of different ^{1}H DQ-dipolar mixing times τ_{m}. The mixing time-dependent intensities obtained by experiments $M^{\exp}(\tau_{\mathrm{m}})$ and calculations $M^{\mathrm{cal}}(\tau_{\mathrm{m}}, \mathbf{\Gamma})$ are shown with circles and lines, respectively. In the calculations, the 7-spin model shown in (a) was used. The intensities calculated with three defferent structural parameter sets $\mathbf{\Gamma} = \mathbf{\Gamma}^{\mathrm{C}}, \mathbf{\Gamma}^{\mathrm{G}}$, and $\mathbf{\Gamma}^{\mathrm{T}}$ are shown in dashed, solid, and dotted lines, respectively. (c) Expansion of the experimental and calculated intensities of the C$^{\beta}$ signal shown in (b). The distributions of the experimental measurements are indicated by the error bars.

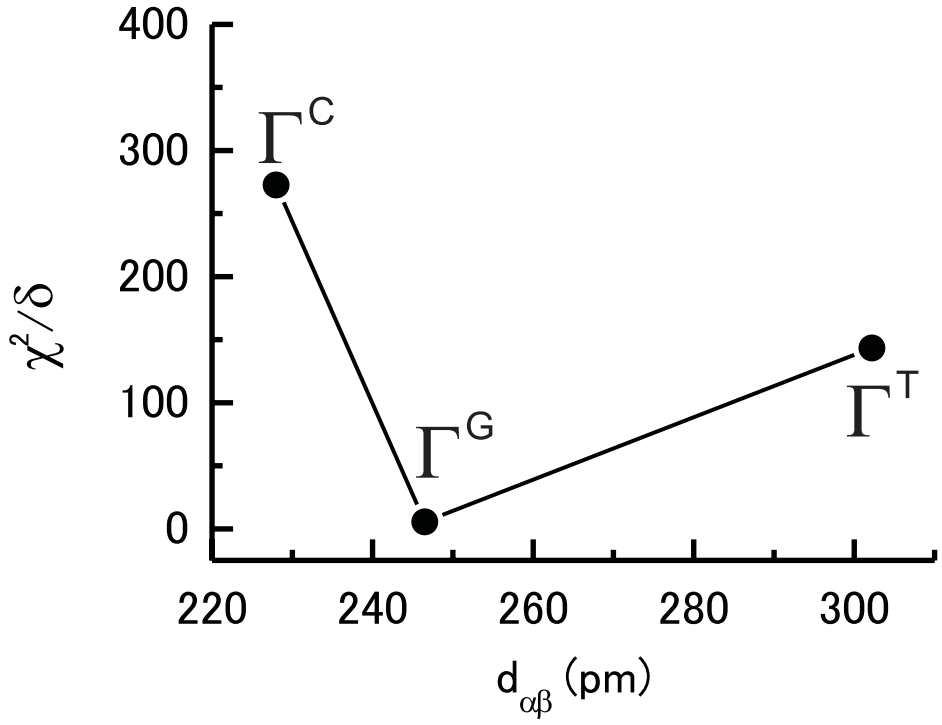

Figure 3.10: Chi-square values obtained by analyzing the experimental data $M^{\exp}(\tau_{\mathrm{m}})$ with intensities $M^{\mathrm{cal}}(\tau_{\mathrm{m}}, \mathbf{\Gamma})$ calculated with three different rotational isotopomers of the 7-spin model system.

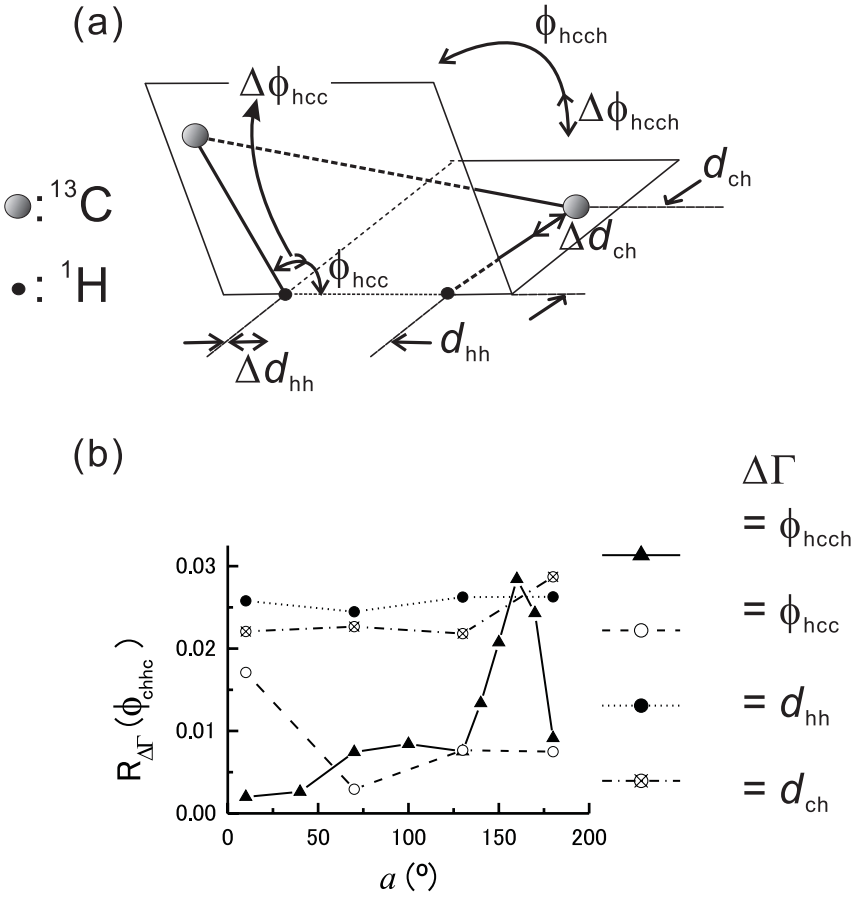

Figure 3.11: (a) Parameters that determine the structure of a 4-spin system that involves two ^{13}C and two ^{1}H spins. (b) RMSD of two calculated signal intensities $M^{\mathrm{cal}}(\tau_{\mathrm{m}}, \mathbf{\Gamma})$ and $M^{\mathrm{cal}}(\tau_{\mathrm{m}}, \mathbf{\Gamma}^{+})$ shown for several dihedral angles ϕ_{hcch} of the 4-spin system shown in (a). The two sets of the structural parameters $\mathbf{\Gamma}$ and $\mathbf{\Gamma}^{+}$ involve a change by $\Delta\Gamma$ in only one of four parameters defined in (a).

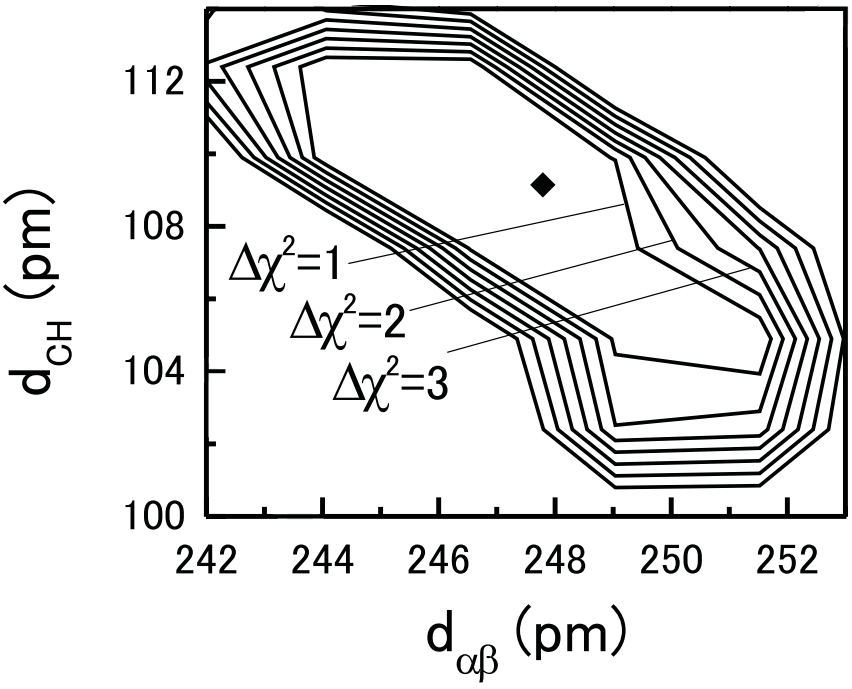

Figure 3.12: χ^2 contour map for the least-squares fitting of the experimental data $M^{\rm exp}(\tau_{\rm m})$ with the numerical calculations $M^{\rm cal}(\tau_{\rm m}, \mathbf{\Gamma})$ with the 7-spin model. In the structural parameters, $d_{\alpha\beta}$ and $d_{\rm CH}$ were treated as adjustable parameters. Numbers of the degrees of freedom is thus $\delta = 2$ with 4 data points and 2 fitting parameters. The χ^2 minimum $\chi^2(0)$ is indicated by a filled diamond and was found to be $\chi^2(0) = 1.06$. Outside the $\Delta\chi^2 = 2$ contour, i.e. $\chi^2 = \chi^2(0) + 2$, the fit has the χ^2 probability of $< 5\%$.

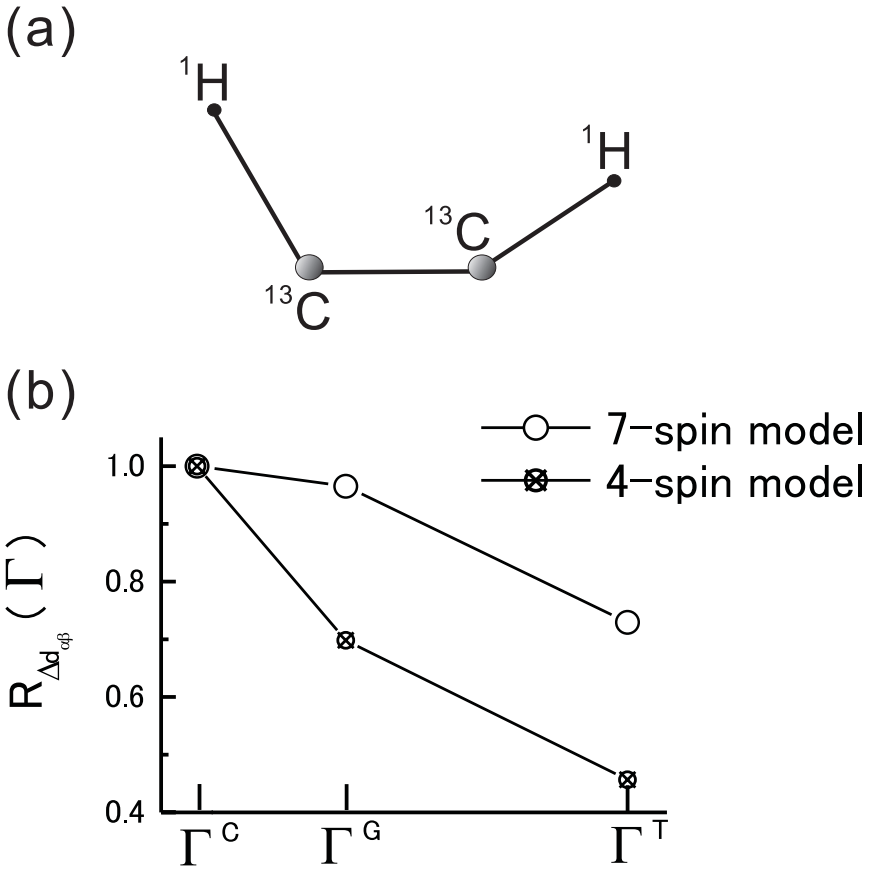

Figure 3.13: (a) Model 4-spin system. The C–C and C–H bond lengths were 150 pm and 109 pm, respectively, and the HCC bond angle was 108°. (b) RMSD of two calculated data $M^{\mathrm{cal}}(\tau_{\mathrm{m}}, \mathbf{\Gamma})$ and $M^{\mathrm{cal}}(\tau_{\mathrm{m}}, \mathbf{\Gamma}^{+})$ with $\mathbf{\Gamma}$ and $\mathbf{\Gamma}^{+}$ that differ in $d_{\alpha\beta}$ by $\Delta d_{\alpha\beta} = 7$ pm.

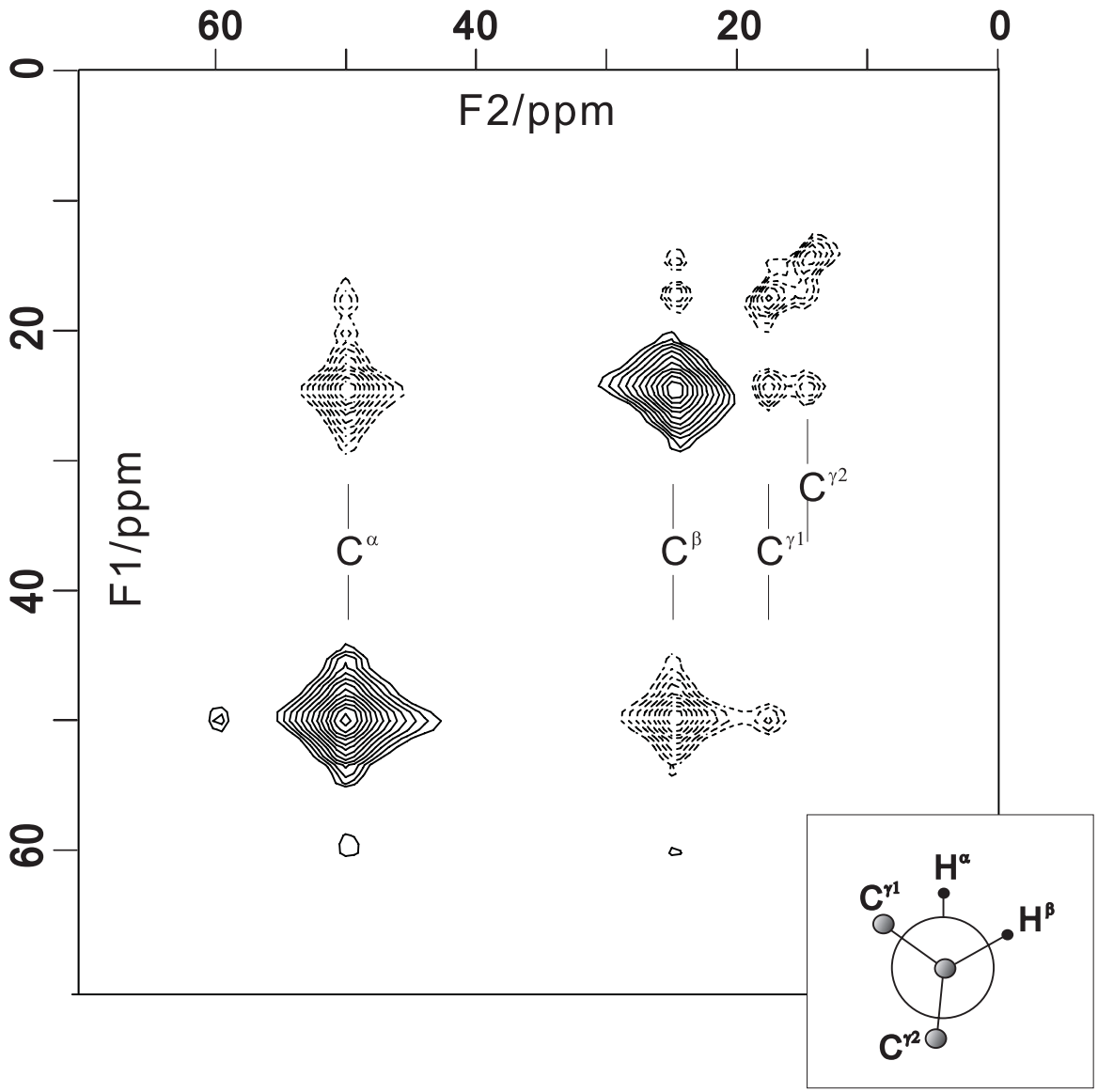

Figure 3.14: Two dimensional ^{1}H DQ-dipolar coupling-mediated ^{13}C/^{13}C-chemical shift correlation spectrum at the aliphatic region. Signals with negative intensities are shown in dashed contour lines. The pulse scheme shown in Fig.3.1(b) was used with $\tau_{\rm m} = 2\tau_{\rm R} \sim 153$ μsec at $\nu_{\rm R} = 13$ kHz. The carboxyl carbon signal is absent in the spectrum because the transfer of the magnetization between ^{13}C and non-directly bonded ^{1}H is suppressed during LGCP periods. The number of scans for an FID was 32 with recycle delay of 5 sec. A complex data matrix $218(t_1) \times 512(t_2)$ was acquired and zero-filled to 1024×1024 matrix. An exponential window function with the line-broadening factor of 100 Hz was applied for both dimension before the Fourier transformation.

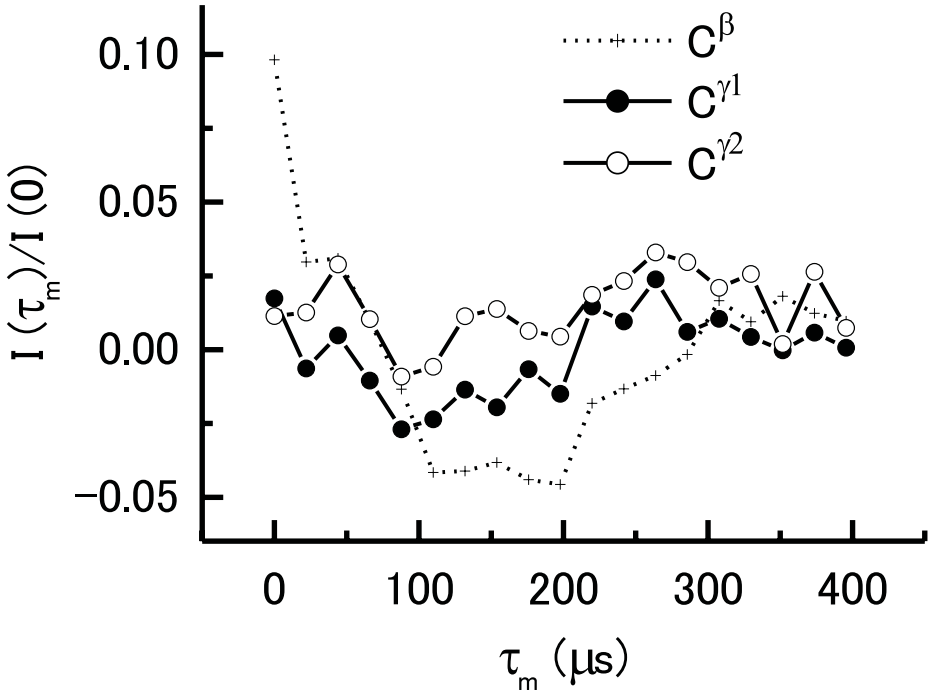

Figure 3.15: Intensity of C^{β}, $C^{\gamma 1}$ and $C^{\gamma 2}$ signals as a function of the ^{1}H DQ-dipolar recoupling time recorded with pulse scheme shown in Fig.3.1(c). Longer duration $\tau_{\mathrm{LG}} = 153$ μsec was used for the second LGCP period to clearly observe the magnetization transferred from H^{α} to H^{γ} spin during the mixing time.

CHAPTER 4

General Discussion

Most of the molecular structure studies by NMR include in its early step the assignment of the resonance signals to the nuclear spins. In solid-state NMR (SSNMR), the ^{13}C resonance assignment is often made because its spectrum has a good signal resolution with the small line width relative to the chemical shift range. The ^{13}C–^{13}C correlation experiment generally involves a magnetization mixing period sandwiched by two chemical shift evolution periods. For the mixing of ^{13}C magnetization, the dipolar interaction can be used. The major problem in such correlation experiment has been the decrease of the

^{13}C magnetization during the dipolar mixing period. When the rf field amplitude of the ^{13}C recoupling pulse, $\omega_{\rm mix}$, approaches to that for the ^{1}H decoupling pulse, $\omega_{\rm dec}$, the heteronuclear CH dipolar interaction is recoupled partially satisfying the Hartmann-Hahn condition $\omega_{\rm dec} = \omega_{\rm mix}$. The CH dipolar interaction dissipates the ^{13}C magnetization to ^{1}H spins, and reduces the signal to noise (S/N) ratio of the spectrum. In chapter 2, the $\omega_{\rm dec}$–$\omega_{\rm mix}$ matching problem was alleviated by reducing $\omega_{\rm mix}$. The author has generalized the design of a known element pulse that was used as a building block of the CN DQ-dipolar recoupling sequence, SPC5. With the recoupling sequence involving such generalized pulse, the effective bandwidth of the magnetization transfer could be varied over broad frequency range. On this basis, the bandselective recoupling scheme has been realized with reduced $\omega_{\rm mix}$.

For the ^{13}C signal assignment with protein sample, two types of ^{13}C–^{13}C dipolar recoupling modes are generally needed for the magnetization transfer. One mode is to mix ^{13}C magnetization among aliphatic ^{13}C spins having small chemical shift differences each other to assign backbone C$^{\alpha}$ and side chain C$^{\beta}$, C$^{\gamma}$ signals in an amino acid residue. The other mode is to mix ^{13}C magnetization among C$^{\alpha}$ and backbone carboxyl C$^{'}$ spins across large chemical shift differences to assign signals amino-acid sequentially. The method de-

veloped in chapter 2 has enabled the bandselective mixing of ^{13}C magnetization in the two modes, i.e. across large and small ^{13}C chemical shift difference. Our method required smaller mixing field amplitude than that required for conventional SPC5 sequence, and increased the S/N ratio of the spectrum. At a fixed ^{1}H decoupling field amplitude, the ratio $\omega_{\rm dec}/\omega_{\rm mix}$ was 2.0 for the conventional SPC5, and was 3.4 with our method in the experiment described in Figs.2.10 and 2.11 in chapter 2. It is known that the ratio larger than 3 is needed for a good CH dipolar decoupling [1, 2]. The S/N ratio was increased also because the magnetization transferred to spins outside the effective bandwidth was suppressed. The reduced power requirement has made our method feasible at faster MAS conditions than the SPC5 experiment with a same mixing rf power available.

Our method has made the CN recoupling sequences feasible at the MAS rate up to about 20 kHz. A recently introduced R18$^5_{10}$ sequence [3] is applicable at the MAS rate as fast as 30 kHz. However, it cannot perform the elaborate truncation of the spin system as demonstrated in Fig.2.11 in chapter 2. At even faster MAS rate of > 30 kHz, Meier *et al.* have recently shown [4] that "low-power decoupling approach" is applicable to alleviate the $\omega_{\rm dec}$–$\omega_{\rm mix}$ matching problem.

Methods other than the DQ-dipolar recoupling can also be used for the ^{13}C magnetization mixing in the correlation experiment. They include the ^{1}H-driven spin diffusion [5], zero-quantum (ZQ) dipolar recoupling with RFDR sequence [6], the CH dipolar assisted rotational resonance (DARR) [7], and so on. The RFDR recouples the ZQ-dipolar interaction most efficiently for spins with chemical shift difference δ_z satisfying $\delta_z \approx \omega_{\rm R}$ with MAS frequency $\omega_{\rm R}$. DARR utilizes ^{1}H-driven spin diffusion for the ^{13}C mixing, and provides a broad effective bandwidth. RFDR and DARR mixing give rise to all positive cross peaks in

the correlation spectrum in contrast to the DQ-dipolar mixing that gives negative cross peak for a correlation to the covalently-bonded ^{13}C spins, providing a convenient information for the signal assignment.

In terms of the S/N ratio, the spectrum obtained with RFDR of DARR mixing is often superior to that obtained with the DQ-dipolar mixing. In the case where RFDR or DARR is used for mixing, the cross peak intensities are equalized in long mixing time because the direct and indirect magnetization transfer pathways contribute additively to the signal intensity. In contrast case where the DQ-dipolar interaction is used for mixing, direct and indirect magnetization transfer contribute negatively and positively to the signal intensity, and cancel each other. Thus, the cross peaks are averaged to zero in long mixing time. In the RFDR or DARR mixing experiment, the additive cross peak intensity leads to generally larger S/N ratio compared with that obtained with DQ-dipolar mixing experiment with CN sequence described in this thesis.

In spin systems involving multiple dipolar couplings, the magnetization exchange occurs between spins that have dominantly strong coupling among other couplings if RFDR or CN was used for the dipolar recoupling. This is due to the phenomenon referred to as dipolar truncation, which often makes the analysis of weak dipolar coupling difficult. Because the magnetization exchange with DARR occurs depending on the spatial arrangement of spin pairs in the powder sample, the magnetization exchange through strong and weak couplings occur in same possibility. Thus, with DARR mixing, the dipolar truncation effect is alleviated.

The cross peak intensity in the correlation spectrum can also be related to spatial proximity of nuclei. The precision of the internuclear distance determination is higher with

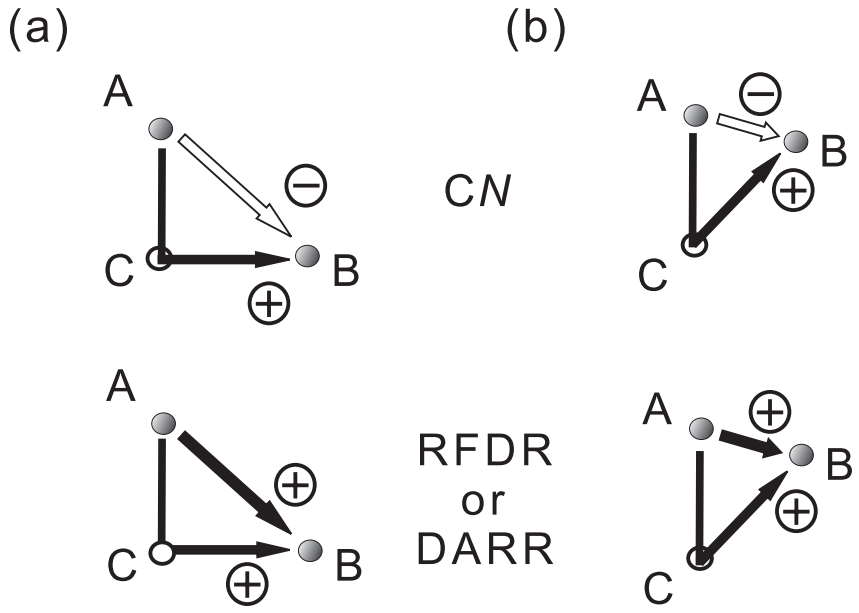

Figure 4.1: Two spatial arrangements of dipolar coupled three spins involving direct and indirect magnetization transfer in different proportion. The magnetization transfers that positively and negatively contribute to the cross peak intensity detected at spin B are denoted by filled and open arrows, respectively. Upper two drawings illustrate the case where the magnetization transfers occur under the effect of the DQ-dipolar interactions recoupled with CN sequence. Lower two drawings illustrate the case where RFDR or DARR is used for the magnetization transfer.

the DQ-dipolar mixing experiments than that with the RFDR or DARR mixing experiment. Figure 4.1 explains this point with a simplified example. The measurement of a distance d_{AB} between spin A and B by analyzing the magnetization transfer from A to B is considered. The dipolar truncation effect is ignored in the following discussion. The cross peak intensity $p(\tau_{\mathrm{m}})$ detected at spin B is characterized by a sum of two magnetization components p_1 and p_2 derived, respectively, from a direct transfer from A to B and that from the indirect transfer intermediating a spin C. In the DQ-dipolar mixing experiment, p_1 and p_2 have opposite contribution to the cross peak intensity, while in the RFDR or DARR mixing experiments, both contribute additively. When the cross peak intensity observed at spin B after the DQ-dipolar mixing is written as

$$p_{\mathrm{DQ}}^{(a)}(\tau_{\mathrm{m}}) = -p_1 + p_2 \tag{4.1}$$

for the spin configuration shown in Fig.4.1, that observed for the configuration of Fig.4.1(b) may be written as

$$\begin{aligned} p_{\mathrm{DQ}}^{(b)}(\tau_{\mathrm{m}}) &= -(p_1 + \Delta p) + (p_2 - \Delta p) \\ &= p_{\mathrm{DQ}}^{(a)}(\tau_{\mathrm{m}}) - 2\Delta p. \end{aligned} \tag{4.2}$$

Above, the change in the spin configuration from that shown in Fig.4.1(a) to (b) is assumed to increase the contribution of the direct transfer by Δp, and to decrease that of the indirect transfer by a same amount. As can be seen in Eq.(4.2), the small change in d_{AB} seen between the two spin configurations appears as the difference of the cross peak intensity by $-2\Delta p$. On the other hand, the cross peak intensity observed in the RFDR or DARR mixing experiment can be written as

$$p_{\mathrm{rfdr}}^{(a)}(\tau_{\mathrm{m}}) = p_1 + p_2, \tag{4.3}$$

for the spin configuration of Fig.4.1(a) and as

$$\begin{aligned} p_{\mathrm{rfdr}}^{(b)}(\tau_{\mathrm{m}}) &= (p_1 + \Delta p) + (p_2 - \Delta p) \\ &= p_{\mathrm{rfdr}}^{(a)}(\tau_{\mathrm{m}}), \end{aligned} \tag{4.4}$$

for that of Fig.4.1(b). Thus, by analyzing transferred magnetization under RFDR- or DARR-mixing, one cannot detect the small difference in d_{AB} in this particular case. This simplified picture suggests that higher precision of the distance measurement is expected for the DQ-dipolar mixing experiment.

Several aspects of the correlation techniques based on different mixing principles have revealed advantages and disadvantages discussed above. A fruitful approach of the signal assignment and molecular structure analysis in SSNMR might involve the combined use of these techniques.

In chapter 3, the DQ-dipolar recoupling technique was applied to precise ^{1}H–^{1}H distance measurement. The proton should be a very valuable nuclei also in SSNMR because

of its ubiquity in organic and inorganic materials and their high magnetogyric ratio. Because even shortest ^{1}H–^{1}H distance often becomes a conformation-dependent parameter [8, 9], the analysis of the molecular conformation based on the ^{1}H–^{1}H distance measurement has an advantage over that based on the ^{13}C–^{13}C distances constraints. However, the direct measurement of the ^{1}H–^{1}H distance has been hampered by the low resolution of ^{1}H NMR spectroscopy in solids.

The method developed in chapter 3 alleviated the low resolution of the ^{1}H spectrum by detecting the ^{1}H magnetization via the ^{13}C free-induction signals. The ^{1}H–^{1}H distance was precisely determined by analyzing the buildup curve of the cross peak intensities as a function of the ^{1}H DQ-dipolar mixing time with exact numerical simulations. The method was applied to fully ^{13}C-enriched L-valine, and internuclear distance $d_{\alpha\beta}$ between H$^\alpha$ and H$^\beta$ as well as the bond length d_{CH} between ^{13}C and ^{1}H involved in the H$^\alpha$C$^\alpha$C$^\beta$H$^\beta$ moiety of the side chain were determined. A least-square fitting of the experimental data by treating $d_{\alpha\beta}$ and d_{CH} as adjustable parameters yielded $d_{\alpha\beta} = 248 \pm 4$ pm and $d_{\mathrm{CH}} = 109 \pm 4$ pm, which are in agreement with the results obtained by the neutron diffraction study [10]. The uncertainty of the determined distances was mainly due to a strong correlation between $d_{\alpha\beta}$ and d_{CH}. The precision also depended on the number of surrounding ^{1}H spins that indirectly participate to the magnetization exchange between a ^{1}H–^{1}H pair of interest. Thus with our method, longer ^{1}H–^{1}H distance is determined in lower precision in a normal non-deuterated sample molecule. Comparison of the simulated and the experimental data has shown that the relative uncertainty u for the ^{1}H–^{1}H distance $d_{\mathrm{hh}} \lesssim 300$ pm should be $u < 6$ %.

The method presented in chapter 3 is characterized with relatively low S/N ratio of the spectrum. This is probably because the naturally abundant ^{1}H spins rapidly form a

large dipolar coupling network among the intra- as well as intermolecular ^{1}H spins during the mixing period. Many indirect coherence transfer pathways within such network leads to cancellation of positive and negative cross peaks under the DQ-process.

Alternatively to the DQ-mixing scheme, one can use the ZQ-dipolar mixing with the same pulse scheme shown in Fig.3.1 in chapter 3. With the ZQ-version, the S/N ratio may be increased by about 20 %. Another conceivable merit of the ZQ-version is that it provides, although imprecise, the medium-to-long range ^{1}H–^{1}H distance estimates under the diffusion approximation of the ^{1}H magnetization exchange. Overall, the DQ-version is talented to provide short ^{1}H–^{1}H distance constraints in high precision, and the ZQ version is suited for producing long range constraints in reduced precision but higher spectral sensitivity. The combined use of these versions should be important.

Our method can be extended to two-dimensional correlation experiment. The 2D spectrum of Val·HCl shown in Fig.3.14 of chapter 3 resolves four ^{1}H–^{1}H correlations. The intensities of these correlation peaks reflect the ^{1}H–^{1}H distances, thus this method is potential to provide many ^{1}H–^{1}H distance constraints in a single measurement. Most recently, Oschkinat *et al.* has shown [8] that a global structure of 62-residue protein can be determined with SSNMR. In their experiment, many long range ^{13}C–^{13}C distance constraints up to $\approx$ 7 Å were used for the structure calculation. Such long range constraints were obtained by the use of the site-directed ^{13}C labeling technique to provide many samples with different ^{13}C spin dilution patterns to alleviate the dipolar truncation effect. Measuring short ^{1}H–^{1}H distances needs no such spin dilution of samples. Our method allows to get many ^{1}H–^{1}H distance constraints with a single fully-labeled sample in a single two-dimensional correlation spectrum, thus speed up the molecular structure analysis by SSNMR.

Large sensitivity enhancements were obtained in liquid-state NMR by the indirect detection of ^{13}C magnetization via ^{1}H NMR signals [11, 12]. Our method can also be developed to detect the spectrum via ^{1}H free-induction signals. With the ultra-fast MAS probe that enables the sample spinning rate of > 30 kHz that efficiently suppresses the ^{1}H homonuclear dipolar couplings, such ^{1}H detection scheme may provide our method a large increase in the S/N ratio of the spectrum.

In this decade, SSNMR technique accomplished astonishing development, and now it is almost equipped with a desirable repertoire of techniques that are capable of yielding large number of structural constraints from each experiment and sample. It is no doubt that with the ultra-high magnetic field and ultra-fast MAS facilities available in the foreseeable future provide accelerated prosperity of SSNMR techniques in molecular structure analysis. The two methods developed in this thesis are both compatible with these futuristic hardware improvements.

References

[1] W. P. Aue, D. J. Ruben, and R. G. Griffin, Uniform chemical shift scaling: application to 2D resolved NMR spectra of rotating powdered samples, *J. Chem. Phys.* **80**, 1729–1738 (1984).

[2] Y. Ishii, J. Ashida, and T. Terao, ^{13}C–^{1}H dipolar recoupling dynamics in ^{13}C multiple-pulse solid-state NMR, *Chem. Phys. Lett.* **246**, 439–445 (1995).

[3] P. E. Kristiansen, D. J. Mitchell, and J. N. S. Evans, Double-quantum dipolar recoupling at high magic-angle spinning rates, *J. Magn. Reson.*. **157**, 253–266 (2002).

[4] M. Ernst, A. Samoson, B. H. Meier, Low-power decoupling in fast magic-angle spinning NMR, *Chem. Phys. Lett.* **348**, 293–302 (2001).

[5] S. K. Straus, T. Bremi, and R. R. Ernst, Experiments and strategies for the assignment of fully ^{13}C/^{15}N-labeled polypeptides by solid state NMR, *J. Biomol. NMR* **12**, 39–50 (1998).

[6] A. E. Benette, C. M. Rienstra, J. M. Griffith, W. Zhen, P. T. Lansbury Jr, and R. G. Griffin, Homonuclear radio frequency-driven recoupling in rotating solids, *J. Chem. Phys.* **108**, 9463–9479 (1998).

[7] K. Takegoshi, S. Nakamura, and T. Terao, ^{13}C–^{1}H dipolar-assisted rotational resonance in magic-angle spinning NMR, *Chem. Phys. Lett.* **344**, 631–637 (2001).

[8] F. Castellani, B. van Rossum, A. Diehl, M. Schubert, K. Rehbein, and H. Oschkinat, Structure of a protein determined by solid-state magic-angle-spinning NMR spectroscopy, *Nature* **420**, 98-102 (2002).

[9] A. Lange, S. Luca, M. Baldus, Structure constraints from proton-mediated rare-spin correlation spectroscopy in rotating solids, *J. Am. Chem. Soc*. **124**, 9704-9705 (2002).

[10] T. F. Koetzle, L. Golic, M. S. Lehmann, J. J. Verbist, and W. C. Hamilton, Precision neutron diffraction structure determination of protein and nucleic acid components. XV. Crystal and molecular structure of the amino acid L-valine hydrochloride, *J. Chem. Phys*. **60**, 4690-4696 (1974).

[11] Y. Ishii, and R. Tycko, Sensitivity enhancement in solid state ^{15}N NMR by indirect detection with high-speed magic angle spinning, *J. Magn. Reson.* **142**, 199–204 (2000).

[12] Y. Ishii, J. P. Yesinowski, and R. Tycko, Sensitivity enhancement in solid state ^{13}C NMR of synthetic polymers and biopolymers by ^{1}H NMR detection with high-speed magic angle spinning, *J. Am. Chem. Soc.* **123**, 2921–2922 (2001).